ESD-TR-89-142

Final Report

Submillimeter Quantum Electronics

T.C.L.G. Sollner

14 June 1989

Lincoln Laboratory
MASSACHUSETTS INSTITUTE OF TECHNOLOGY
LEXINGTON, MASSACHUSETTS

Prepared for the Department of the Army
under Electronic Systems Division Contract F19628-85-C-0002.

ADA210439

The work reported in this document was performed at Lincoln Laboratory, a center for research operated by Massachusetts Institute of Technology. This program is sponsored by the U.S. Army Research Office under Air Force Contract F19628-85-C-0002.

This technical report has been reviewed and is approved for publication.

FOR THE COMMANDER

Hugh L. Southall

Hugh L. Southall, Lt. Col., USAF
Chief, ESD Lincoln Laboratory Project Office

MASSACHUSETTS INSTITUTE OF TECHNOLOGY
LINCOLN LABORATORY

SUBMILLIMETER QUANTUM ELECTRONICS

T.C.L.G. SOLLNER
Group 87

FINAL REPORT
TO THE
U.S. ARMY RESEARCH OFFICE

1 APRIL 1985 — 1 NOVEMBER 1988

ISSUED 14 JUNE 1989

Approved for public release; distribution is unlimited.

LEXINGTON MASSACHUSETTS

SUBMILLIMETER QUANTUM ELECTRONICS

FINAL REPORT

T.C.L.G. SOLLNER

28 APRIL 1989

U. S. ARMY RESEARCH OFFICE

GRANT NUMBER 22746-PH

LINCOLN LABORATORY

MASSACHUSETTS INSTITUTE OF TECHNOLOGY

APPROVED FOR PUBLIC RELEASE;

DISTRIBUTION UNLIMITED

TABLE OF CONTENTS

APPENDICES -- Publications

A. Microwave and Millimeter-Wave Resonant-Tunneling Devices

B. Large Room-Temperature Effects from Resonant Tunneling through AlAs Barriers

C. Fundamental Oscillations up to 200 GHz in Resonant Tunneling Diodes and New Estimates of Their Maximum Oscillation Frequency from Stationary-State Tunneling Theory

D. Harmonic Multiplication Using Resonant Tunneling

E. Observation of Millimeter-Wave Oscillations from Resonant Tunneling Diodes and Some Theoretical Considerations of Ultimate Frequency Limits.

F. Persistent Photoconductivity in Quantum Well Resonators

G. Persistent Photoconductivity in Resonant Tunneling Structures: Toward a Resonant Tunneling Transistor

H. Picosecond Switching Time Measurement of a Resonant Tunneling Diode

I. Planar Dipole-Fed Mixer Arrays for Imaging at Millimeter and Submillimeter Wavelengths

J. Submillimeter-Wave Heterodyne Spectroscopy with a Compact Solid State Radiometer.

1. INTRODUCTION

Recent years have seen a rapid increase in research on quantum-well physics, materials, devices and theories. The emergence of quantum-well electronics has ushered in a new era in tailoring materials and structures for specific purposes, and now offers the possibility to advance the state of the art of submillimeter technology and a means to study high speed processes in semiconductors. This activity is indicative of the great need for ultra-fast active components. The program summarized here has developed some new approaches to fill this need.

At Lincoln Laboratory we have placed our primary effort in the recent ARO program on the area of resonant-tunneling devices. We have studied the physics of resonant tunneling and developed oscillators, multipliers, and mixers into the submillimeter spectrum. Preliminary work into the feasibility of resonant-tunneling transistors has also been undertaken. Planar antenna arrays have been investigated initially for application to detector arrays, but they may also have application for oscillator arrays. The results from all these studies have been so encouraging that we are planning to continue development of these devices and to investigate new phenomena involving coupled quantum wells.

2. RESULTS

Progress during the contract period has been reported in the semiannual progress reports to ARO. Below are listed significant highlights, the details of which appear in the reprints and preprints that are appended to this report. In most cases the work received additional support from other sponsors. An overview of some of the devices developed under this program can also be found in Appendix A.

2.1. Large Negative Differential Conductance at Room Temperature

Early resonant-tunneling structures required cooling to achieve negative differential conductance. However, by using thin AlAs barriers instead of the AlGaAs alloy and by reducing the impurity concentration outside the barriers, we have obtained peak-to-valley ratios of 3.5:1 and current densities of 4×10^4 A/cm^2 at room temperature. This development has greatly simplified the fabrication and testing of a variety of devices, in particular oscillators, and has expedited other investigations of the physics of resonant tunneling. (See Appendix B for details.)

2.2. Room-Temperature Oscillators

We have achieved fundamental oscillation frequencies up to 420 GHz using the negative differential conductance region of the resonant-tunneling current-voltage (I-V) curve. (See Appendix C for results up to 200 GHz. The 420 GHz results are in preparation.) This oscillation frequency confirms our predictions of the extrinsic maximum oscillation frequency for the double-barrier structure used in these experiments and surpasses any tunnel diode result reported in the literature. However, the power measured at 200 GHz is only 0.2 μW for this material, largely because this frequency is very close to the maximum oscillation frequency of 270 GHz. At lower frequencies ($\leq$ 60 GHz) we have measured powers between 50 and 200 μW. Although these powers are insufficient for use as a local oscillator with a room-temperature Schottky diode mixer, they are more than enough for a local oscillator with superconductor-insulator-superconductor (SIS) mixers operating at 4 K. We have also measured other properties of the resonant-tunneling oscillator specific to its application as a local oscillator. Frequency tunability of over 10% has been demonstrated near 100 GHz, and injection locking is possible with injected power 20 dB below the peak oscillator power. This latter fact and specific noise measurements indicate that resonant-tunneling oscillators should be quite low in noise content.

2.3. Self-Oscillating Harmonic Mixer

The resonant-tunneling diode has the capability to act as an efficient mixer because of the rapid variation of the dynamic conductance with voltage near the negative-differential-resistance region of the I-V curve. For a diode oscillating with a DC bias at the center of this negative-differential-resistance range, the time-varying dynamic conductance actually has a predominant Fourier component at the second harmonic of the oscillation frequency. This implies that the conversion efficiency should be high for signals at twice the oscillation frequency. We have experimentally studied the properties of this harmonic conversion with a resonant-tunneling structure that oscillated at 50 GHz. The conversion loss of a 100-GHz signal was found to be about 12 dB, which is near the state of the art for harmonic mixers. This suggests that self-oscillating resonant-tunneling mixers could be very useful in the millimeter-wave band, perhaps replacing conventional Schottky diode mixers in applications where the use of a separate local oscillator is either difficult or undesirable. (See Appendix A for details.)

2.4. Multipliers

We have used double-barrier resonant-tunneling structures as microwave and millimeter-wave multipliers. The antisymmetry of the I-V curve about the origin, i.e., I(V)=-I(-V), combined with the presence of a negative differential resistance region, suggests that fifth-harmonic generation should be especially efficient with a DC bias voltage near zero. We have observed fifth-harmonic efficiencies of -23 dB multiplying from 4 to 20 GHz without optimized device or load impedances. Theoretical predictions suggest that efficiencies slightly greater than -10 dB should be obtainable. The maximum output frequency should be on the order of the maximum oscillation frequency, as discussed in Appendix D.

2.5. Ultimate Frequency Limits for Resonant-Tunneling Diodes

We have calculated the times required for charge transport through various parts of the double-barrier structure, including the depletion region. Using the experimentally observed oscillation frequencies, we have shown that the WKB approximation greatly overestimates the storage time of charge in the well, and that a calculation method based on the energy width of the resonant state gives results consistent with the measurements. Also, the transit time across the depletion region can be important at higher frequencies, as can the RC time determined by parasitic series resistance and device capacitance. This theoretical foundation provides a guide to design of higher frequency structures and suggests that there are no fundamental or practical impediments to development of resonant-tunneling oscillators up to several hundred gigahertz. (See Appendix E for details.)

2.6. Persistent Photoconductivity

We have made the first observation of persistent photoconductivity in resonant-tunneling structures. Illumination at low temperatures of structures with $Al_{0.3}Ga_{0.7}As$ barriers results in a persistent shift of the current-voltage (I-V) curve. This is explained by modifications to the conduction band from fixed positive charges in the barriers and equal negative charges that accumulate outside the barriers. The fixed positive charge arises from ionization of DX centers located in the barriers. Calculated I-V curves agree with our measurements, and the derived DX center density agrees with estimates from material-growth constants. This effect has been useful in determining the heterojunction parameters (as described in Appendix F) and in estimating the performance of the structure in which the quantum well is contacted to form a resonant-tunneling transistor. In the latter case, the change of the well potential with respect to the contacts (caused by the DX center ionization) permitted an estimate of transistor transconductance and cutoff frequency. (Appendix H has details of the transistor.)

2.7. Resonant-Tunneling Transistor

A resonant-tunneling transistor has been proposed and fabrication feasibility studies have begun. The persistent photoconductive effects discussed above have made it possible to estimate the transconductance and unity-current-gain frequency f_T for a transistor based on the double-barrier resonant-tunneling structure, in which the well serves as the control electrode. With conservative assumptions based on experimentally obtained current densities, the projected transconductance g_m for a 1-µm emitter stripe is 2000 mS/mm. This corresponds to a f_T of at least 50-100 GHz and a maximum frequency of oscillation f_{max} of 150-200 GHz. Moreover, an increase in current density beyond that presently attained by over a factor of 10 is predicted theoretically, which should increase the f_T to well over 100 GHz. (See Appendix F for details.) We have developed a technique for growing thicker epitaxial layers that are attached to the thin quantum well by growing on the sidewall and horizontal surfaces of an etched-groove structure. Horizontal barriers and wells nearly three times as thick as on the sidewalls have been achieved. This should simplify the fabrication of contacts to the thin quantum wells.

2.8. Picosecond Optical Measurements

The switching time of one of our resonant-tunneling diodes (with oscillation cutoff frequency of 270 GHz) has been measured, using optically generated picosecond electrical pulses. The measurement was made in collaboration with Gerard Mourou and his students at the University of Rochester. (See Appendix H for details.) The observed switching time of 2 ps is in agreement with an approximate theory of switching time: $\tau \cong C(\Delta V/\Delta I)$, where $\Delta V(\Delta I)$ is the voltage (current) excursion of the negative differential resistance region. These experiments confirm our earlier measurements in the frequency domain, and suggest that the device could act as a high-speed switch. Promising digital applications are being explored.

2.9. Planar Dipole-Fed Mixer Arrays

A planar double-dipole antenna containing a beam-lead Schottky diode has been developed to produce the best sensitivity of any planar mixer above 100 GHz [T_{rec} = 4900 K (DSB)] at 140 GHz. This element has also been incorporated into a planar two-dimensional array that performed well for element spacing of about two wavelengths. (See Appendix I for details.) With the Schottky diode replaced by a resonant-tunneling diode, the double-dipole could act as a resonator for oscillations in the submillimeter region. If successful, the oscillating elements could then be combined in an array to greatly increase the output power.

2.10. Rocket-Plume Spectroscopy at 557 GHz with a Compact Solid-State Radiometer

We have developed a compact, solid-state submillimeter-wave heterodyne radiometer and have used it to measure spectral characteristics of a simulated rocket exhaust plume. Features of the 557-GHz water-vapor line profile were observed in significantly greater detail than in previous experiments through increased sensitivity and improved frequency resolution (600 kHz). A prominent self-reversal feature from a warmer central core of the plume was observed. The local oscillator of the radiometer utilized a frequency multiplication chain consisting of an InP Gunn oscillator at 92.6 GHz driving a frequency tripler and second-harmonic mixer in cascade. The receiver had a noise temperature of 4500 K (DSB) at 555 GHz, consumed 3 W and weighed 3 kg. (This project was carried out in collaboration with N.R. Erickson, University of Massachusetts, Amherst. See Appendix J for details.)

T.C.L.G. SOLLNER, E.R. BROWN, and H.Q. LE

Microwave and Millimeter-Wave Resonant-Tunneling Devices

Resonant-tunneling devices, which may be capable of operation at terahertz frequencies, have been developed and tested. Included in these solid state microelectronic components are oscillators, self-oscillating mixers, and harmonic multipliers. A characteristic of these devices, negative differential resistance (NDR), has been observed at room temperature. Resonant-tunneling transistors, which promise operation in the terahertz frequency range, are also proposed.

PHYSICS OF RESONANT TUNNELING

A resonant-tunneling diode can respond to electrical impulses in picosecond or subpicosecond times. Therefore, these devices may provide a basis for developing electronic devices that operate at terahertz frequencies.

The essential features of resonant tunneling are shown in Fig 1. A thin layer of GaAs (2 to 10 nm) is sandwiched between two thin layers of $Al_xGa_{1-x}As$. The addition of aluminum to GaAs raises the band-gap above that of GaAs so the $Al_xGa_{1-x}As$ regions act as partially transparent mirrors to electrons; the higher energy level of these barriers reflects the electrons back to the region of the structure from which they came. The charge transport across the structure takes place by tunneling through the thin (1 to 5 nm) $Al_xGa_{1-x}As$ barriers.

This structure is the electron analog of a Fabry-Perot resonator. As shown schematically at the bottom of Fig. 1, the resonator exhibits peaks in the electron transmission (current) as the incident electron energy (voltage) changes.

The physical implementation of these principles is summarized in Fig. 2. The layered material is grown in wafer form by molecular beam epitaxy. Then the active regions are defined with ohmic contacts. These contacts are used as a mask to isolate the region under the contact, either by etching mesas (as shown in Fig. 2), or by proton implantation, which makes the surrounding material nonconductive. Because the contact is only a few microns in diameter, electrical connection to the ohmic contact is made with a pointed wire (whisker). In some cases, the whisker acts as an antenna, coupling high-frequency ac fields to the double-barrier diode.

Using the Fabry-Perot analogy, coherence of the electron-wave function is required across the entire double-barrier region to maintain resonant tunneling. Any scattering that occurs in either the well or the barriers will alter the wave function phase randomly, destroying its coherence and therefore, the conditions required for resonant tunneling. But a different picture (see Appendix, "Resonant Tunneling Theory"), one that does not require coherence between the parts of the wave function outside and inside the well, can produce negative resistance, the essential characteristic that is exploited in the devices that are described in this article.

In 1973, Tsu and Esaki [1] derived the two-terminal current-voltage (I-V) curves for finite multiple-barrier structures. This matching technique has been remarkably successful in explaining experimental results. In 1974, Chang *et al* [2] were the first to observe resonant tunneling in a monocrystalline semiconductor. They used a two-barrier structure and observed the resonances in the current by measuring the I-V curve of the structure. The voltages at the current peaks agreed well with Chang's calculations.

A decade later, interest in the field was renewed when Sollner *et al* [3] showed that the intrinsic charge transport mechanism of a two-barrier diode could respond to voltage changes in less than 0.1 ps (> 1 THz). More recently, negative differential resistance (NDR), a characteristic of resonant tunneling, has been measured at room temperature [4].

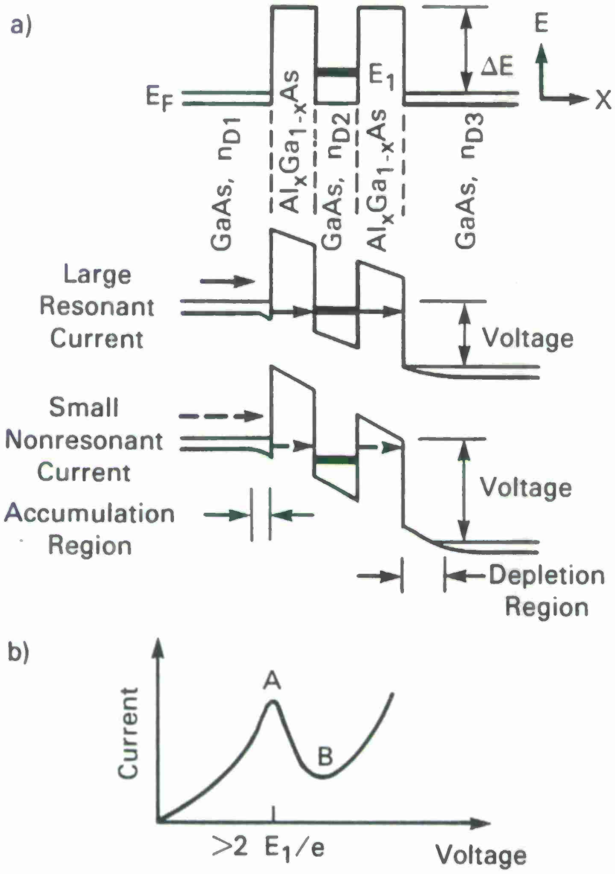

Fig. 1(a) — The energy profile of an electron in a double-barrier resonant-tunneling structure is shown here. The top illustration, which includes the energy well produced by the two $Al_xGa_{1-x}As$ layers, shows the unbiased energy profile. The $Al_xGa_{1-x}As$ layers act as partially transparent mirrors to the electrons, similar to a Fabry-Perot resonator. (b) In this plot of diode current as a function of incident electron energy, the large resonant current at point A corresponds to the energy profile of A; the valley in the current-profile at point B corresponds to energy profile of B. Although the energy of incident electrons is higher at B, the absence of resonance lowers the current.

SPEED OF RESPONSE

Two factors indicate that the response time of a double-barrier resonant-tunneling structure should be as little as 0.1 ps: the resonant-state lifetime of an electron and the time required for a double-barrier structure to reach equilibrium after an electrical impulse. This predicted response time is the time required for the device's current to respond to a sudden change in voltage. The comparison of the measured and predicted times not only gives an indication of the accuracy of the models, it also indicates the fundamental limits of operation imposed by the structure of double-barrier devices. One of the most significant limits of operation is f_{max}, the maximum useful frequency at which the device exhibits NDR. This frequency is the point above which NDR is no longer observable at the terminals of the device.

If the voltage across a double-barrier structure is instantaneously changed, the current through the device changes to a different steady-state value. As in a Fabry-Perot resonator, the steady-state charge in the well must decrease when the current decreases, and increase when the current increases. The lifetime of any resonant state, including the one represented by an electron initially placed in the well between the two barriers of a resonant-tunneling structure, is given by $\tau = \hbar/\Delta E$, where ΔE is the energy half-width of the transmission probability function through the resonant state. It takes approximately one lifetime to fill or empty the well to a new steady-state value. Since the carrier transmission probability is determined by the amplitude of the wave function inside the well, the current will reach its new steady-state value in approximately the lifetime of a resonant state.

The lifetime of an electron in between the barriers has been calculated for three representative structures by Sollner *et al* [5] and ranges from 4 ps for a 2.5-nm AlAs barrier to 0.16 ps for a 3.0-nm $Ga_{0.7}Al_{0.3}As$ barrier. In Table 1, this time is found from $\tau = 1/(2\pi f_{\Delta E})$. The transit of electrons across the structure's depletion region produces an additional delay that ranges from 0.16 to 0.69 ps. Total delays, the *intrinsic* response times, therefore range from 0.4 to 5.0 ps.

For signals with periods much shorter than the intrinsic response time, the current lags the applied voltage and the I-V curve for the high-speed signals should deviate markedly from the dc I-V curve. The intrinsic response time was first measured experimentally by examining the difference between the dc I-V curve measured and the I-V curve inferred from high-frequency measurements. Because the response times were in the picosecond range,

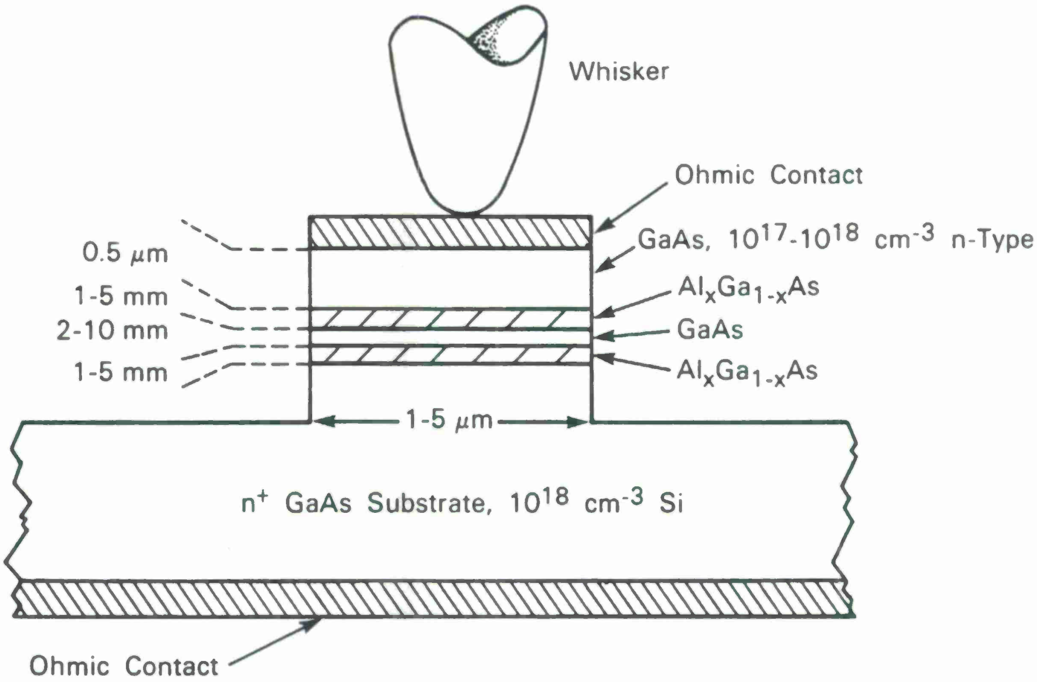

Fig. 2 — This double-barrier diode has 1- to 5-nm barriers and a 2- to 10-nm well.

operation at terahertz frequencies was necessary.

The straightforward approach to determining the frequency response of a device is to sweep through the I-V curve at increasing speed until the measured I-V curve differs from the dc curve. Unfortunately, it is difficult to measure current at frequencies above those accessible to sampling oscilloscopes (100 GHz). Therefore, we used a differential measurement technique. We swept through a large, low-frequency voltage-range and measured the diode current with relatively simple conventional techniques. At the same time we superposed a small high-frequency signal across the diode. The low-frequency current revealed changes in curvature of the I-V curve that were proportional to the high-frequency signal. Besides tractability, this method of measurement closely resembles the actual operating conditions of devices which utilize NDR. In practical operation, a device is biased into the negative differential region by a large dc bias and the superposed voltage doesn't extend far outside the NDR region.

The circuit used for applying ac and dc fields to the double-barrier diode is shown in Fig. 3. The corner-reflector mount was originally developed for Schottky-diode mixers in the far infrared [6]. Frequencies between dc and about 20 GHz can be applied through the coaxial connector via the whisker that contacts the active area. The GaAs substrate is soldered to the chip stud, which is at the same ground potential as the corner reflector. For frequencies of about 100 GHz to a few terahertz, the long whisker acts as an antenna, and the conducting surfaces cause images of the whisker to produce an antenna array. The array will receive energy in a beam that has a frequency-dependent direction, but is approximately 45° from all surfaces of the cube. The full cone-angle of the beam is about 20°.

For the 2.5-THz measurements, for example, the power produced by an optically pumped methanol laser (about 100 mW) was matched to the antenna pattern with a lens, thus coupling about 50% of the incident power onto the antenna and producing an ac signal across the double-barrier structure. The characterization of the corner-reflector mount at lower frequencies (using measurements performed by Fetterman *et al*) led to an estimate of 50 Ω for the antenna impedance Z_A. This parameter was used in Eq. (1) to calculate the curves in Fig. 4.

At high frequencies the current responsivity R_i, which is the change in dc current (ΔI), divided by the change in ac power applied, (ΔP_{ac}), is given by

$$R_i(V) = \frac{\Delta I(V)}{\Delta P_{ac}} = \frac{2I''(V)Z_A}{(1+Z_A/R_s)^2}\left(\frac{1}{\omega R_s C}\right)^2 \qquad (1)$$

In Eq. 1, I'' is the second derivative of the I-V curve at the ac frequency of interest. This expression gives the I-V curve for current responsivity measured over the voltage range of interest. Measurements were made at 1, 138, 761, and 2,500 GHz on a double-barrier diode with 3.0-nm well and barriers. The results at dc, 1 GHz and 2.5 THz are shown in Fig. 4. The measurements for 138 and 761 GHz were essentially identical to the 1-GHz curve. Since the 1-GHz signal's period is long compared with the expected intrinsic response time, deviation in the I-V curve shouldn't occur until frequencies that are orders of magnitude higher are reached. The reason for the change between dc and 1 GHz is not known, but it is probably due to slow traps in the material.

By 2.5 THz, the diode's I-V curve looks quite different from the dc curve. In one direction, NDR has vanished, but it remains in the other direction. Sollner *et al* [3] take this as evidence that the intrinsic response time for this device is of the order of $\tau = (2\pi f)^{-1} = 6 \times 10^{-14}$ s. This result agrees approximately with theoretical

Table 1 — Measured and Calculated Parameters for Three Different Wafers of Double-Barrier Diodes

	Wafer		
	1	*2*	*3*
Material Parameters			
Barrier material	AlAs	$Ga_{0.7}Al_{0.3}As$	AlAs
Barrier thickness (nm)	2.5	3.0	1.5
Well thickness (nm)	4.5	4.5	4.5
Doping outside barriers (cm^{-3})	1×10^{18}	2×10^{17}	2×10^{17}
Electrical Parameters			
Peak-to-valley ratio, 300 K	1.7/1	1.3/1	3.5/1
Peak current density ($\times 10^4$ A cm^{-2})	0.8	1.2	4.0
Depletion layer at bias (nm)	15	30	70
Capacitance (fF)[a]	100	50	20
Maximum negative conductance (mS)[a]	5.0	8.0	13.0
Series resistance (Ω)[a]	10	15	15
Oscillation Characteristics			
DC bias I_B, V_B (mA, V)	0.7, 0.40	2.7, 0.32	3.0, 0.95
f_{osc} (GHz)[b]	20.7	43.7	201
Theoretical			
Maximum Oscillation Frequency			
f_{max} (GHz)[c]	35	70	270
f_{depl} (GHz)[d]	1,000	500	230
$f_{\Delta E}$ (GHz)[e]	40	1,000	400

[a] Typical values for a circular mesa of 4-μm diameter.

[b] Maximum observed fundamental oscillation frequency.

[c] $f_{max} = (2\pi C)^{-1}(-G_{max}/R_s - G_{max}^2)^{1/2}$

[d] From depletion layer drift time assuming a drift velocity of 10^7 cm/s.

[e] From calculation of energy width of transmission through double-barrier structure.

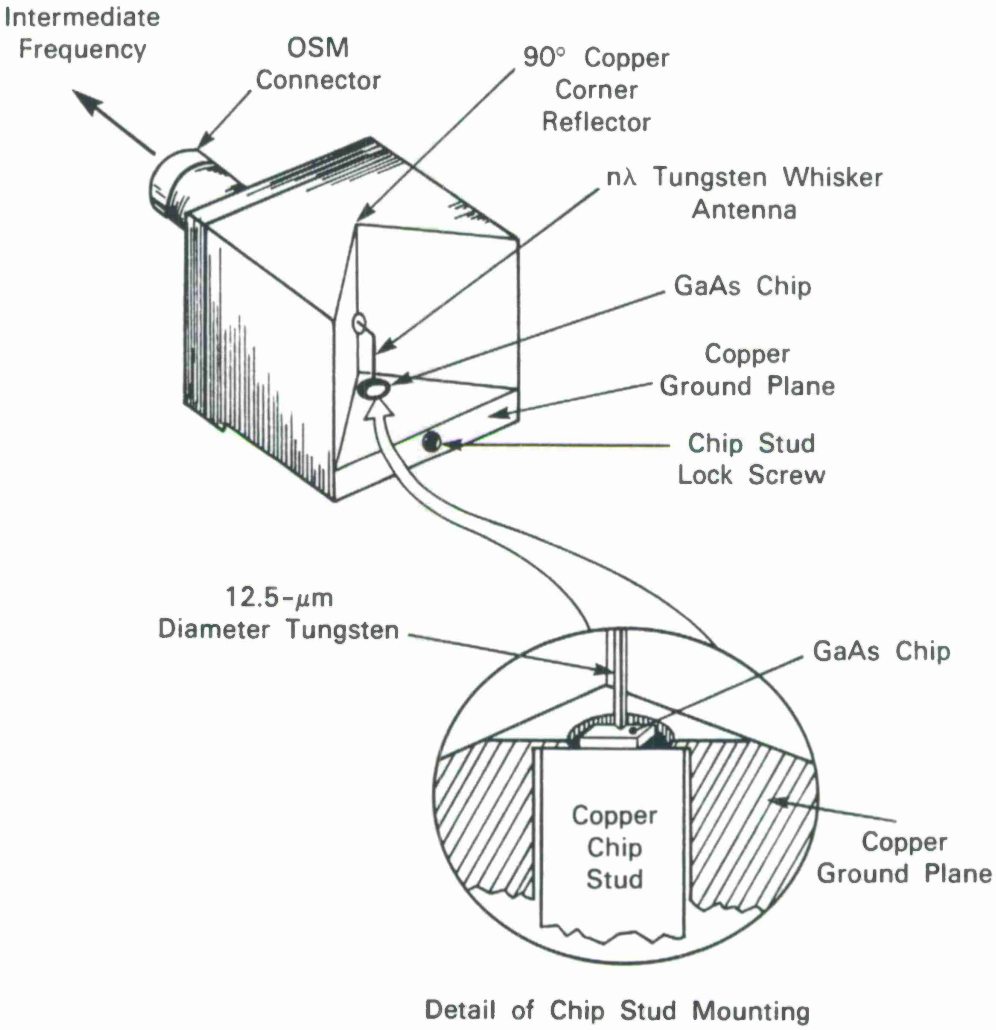

Fig. 3 — This corner-reflector mount is used to apply signals to double-barrier diodes. For frequencies between dc and 20 GHz, the signal is coupled through the OSM connector. Above 100 GHz, the long whisker acts as an antenna, coupling the signals into the chip from a full cone-angle of about 20°.

expectations from Table 1 for 3-nm barriers of $Al_{0.25}Ga_{0.75}As$ ($f_{\Delta E} = 1 \times 10^{15}$). The asymmetry of both the dc I-V curve and the response may indicate that the two barriers or the two depletion regions are not identical.

The double-barrier diode's equivalent circuit, shown in Fig. 5, provides a model for further understanding of this device. Included in the equivalent circuit are the voltage-dependent dynamic conductance G(V), the series resistance R_s, and the parallel capacitor C that is inherent in the device structure. To a good approximation, the capacitance is formed across a combination of the two barriers plus the depletion region on the anode side of the biased device. The slope of the low-frequency I-V curve gives the approximate conductance, *ie*, $(dI/dV)^{-1} = R_s + 1/G \approx 1/G$.

RESONANT-TUNNELING OSCILLATORS

The NDR displayed by the double-barrier diode is the basis of a fast and simple two-terminal oscillator. Interest in the oscillator application stems from the need for a solid state oscillation source at frequencies above 300 GHz. In this region, few fundamental-mode solid state sources are available, so the double-barrier diode would be useful for applications that require only modest amounts of power. Furthermore, these oscillations give a direct and unmistakable proof of the speed of these devices. Of course, inherent circuit elements, particularly the series resistance and the device capacitance shown in Fig. 5, must be considered for circuit applications of these devices.

In the further analysis required for circuit applications, the conductance, $G(V_0)$, is independent of frequency but strongly dependent on the voltage amplitude, V_0, across the device. The real part of the impedance, Z_D, measured across the equivalent circuit of Fig. 5 is negative up to a frequency given by the expression

$$f_{max} = \frac{1}{2\pi C}\left(\frac{-G_{max}}{R_s} - G_{max}^2\right)^{1/2} \qquad (2)$$

where G_{max} is the maximum negative value of dynamic conductance in the NDR region of the I-V curve. For all frequencies above f_{max}, the real part of the terminal impedance will be positive, making it impossible for oscillations to occur.

Brown *et al* [7] found double-barrier diode oscillators that cover the frequency range of 20 to 200 GHz (frequencies below f_{max}). Figure 6 shows the experimental results obtained in this range with diodes from the wafers listed in Table 1. The initial experiments were performed with a device from Wafer 1 in a coaxial resonator, giving an oscillation frequency of 20.7 GHz and an output power well below 1 W. Attempts to achieve oscillation with this device at frequencies near 40 GHz in a WR-22 waveguide resonator were unsuccessful, consistent with the theoretical f_{max} of 35 GHz. The first millimeter-band results were obtained in the vicinity of 30 GHz and 40 GHz in WR-22 and WR-15 waveguide resonators, respectively, using a device from Wafer 2. This device could have achieved higher oscillation frequencies, but because of the relatively low peak-to-valley ratios of devices from Wafer 2, no attempt at higher oscillation frequencies was made. The wafer's low peak-to-valley ratio indicates that devices from this wafer will provide limited power output and logic-swing capability.

The voltage range over which NDR exists for these devices limits the output power of oscillators that use them. Kim and Brandli [8] and

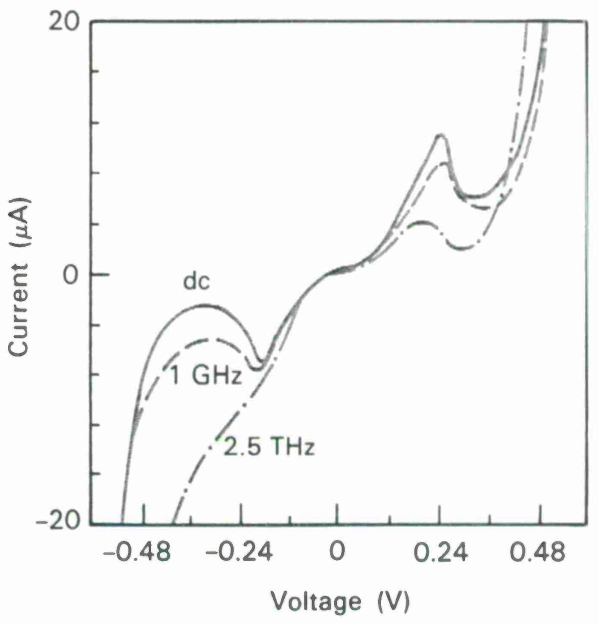

Fig. 4 — The current-voltage (I-V) curves of a double-barrier diode show the variation with frequency of the device's negative differential resistance — it essentially disappears at 2.5 THz.

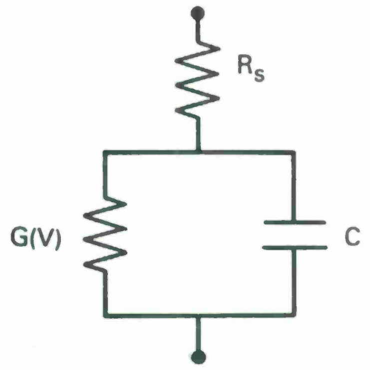

$$f_{max} = \frac{1}{2\pi C}\left[\frac{-G_{max}}{R_S} - G_{max}^2\right]^{1/2}$$

$$R_S = \rho_{epi}\frac{\ell}{A} + R_{spread} + R_C$$

$$C = \epsilon\frac{A}{L_{depl}}$$

Fig. 5 — Using this equivalent circuit, the double-barrier diode's maximum frequency of oscillation can be easily calculated.

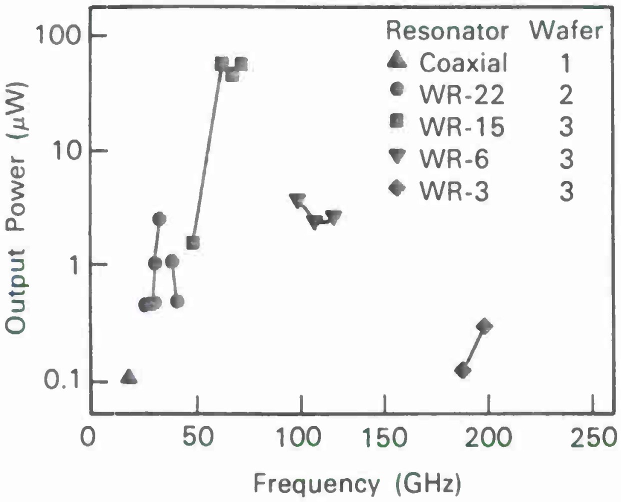

Fig. 6 — The output power versus frequency of resonant-tunneling diodes for three different wafers was measured in five different resonators.

Trambarulo [9] have shown that the maximum output power, assuming a sinusoidal voltage waveform, is $P_{max} = (3/16)\Delta I/\Delta V$, where ΔI and ΔV are the current and voltage ranges of the negative resistance region. For the 4-μm-diameter diodes of Wafer 3 in Table 1, this relation gives $P_{max} \approx 225$ μW. Diodes of larger area can produce more output power, but G_{max} scales linearly with diode area, making it very difficult to obtain dc stability in larger devices. All of the 4-μm-diameter devices tested to date have been stabilized with standard 50 Ω coaxial loads.

Diodes from Wafer 3 have produced the most powerful oscillations and the highest oscillation frequency to date. This wafer extended the maximum observed oscillation frequency of resonant-tunneling diodes from 56 to 201 GHz. The output power produced at 201 GHz was about 0.2 μW, although it reached 60 μW at lower frequencies. Several of the diodes tested did not oscillate at all. The difficulty in initiating oscillations near 200 GHz is consistent with Eq. 2, which predicts that $f_{max} \approx 270$ GHz for this diode.

The Fig. 5 model is identical to that used for p-n junction tunnel diodes. Indeed, the double-barrier resonant-tunneling diode and the p-n junction tunnel diode are similar, displaying similarities in I-V characteristics and in circuit behavior. The major difference between the two types of diodes is in the magnitude of their parasitics. In the p-n junction tunnel diode, very high doping densities are required on both sides of the junction ($N \leqslant 1 \times 10^{19}$ cm^{-3}) to achieve a high tunneling current density. This high doping density creates a short depletion layer and therefore a relatively large specific capacitance. The double-barrier diode, however, can achieve a high current density with much lower doping densities on both sides of the structure ($N \approx 10^{17}$ to 10^{18} cm^{-3}).

A good figure of merit for comparing the speed of different diodes is the ratio of specific capacitance to peak current density, $\gamma = C_S/J_P$. This ratio is known as the speed index [10]; it is a measure of the current available for charging the device capacitance. For Wafer 3, this quantity is $\gamma \approx 1 \times 10^5$ pF cm^{-2}/4.0×10^4 A cm^{-2} = 3.0 ps/V. The fastest p-n junction tunnel diodes ever reported [11] were made of GaAs and had γ = 14 to 16 ps/V, nearly a factor of five poorer than the double-barrier devices. Moreover, the p-n junction tunnel diodes [12] achieved a maximum experimental oscillation frequency of only 103 GHz with an output power well below 1 μW.

SELF-OSCILLATING MIXERS

Near the NDR region in an I-V curve, a resonant-tunneling diode's dynamic conductance varies rapidly as a function of the applied signal voltage. This feature makes the resonant tunneling diode an efficient mixer. The Fourier series of the diode's dynamic conductance has large components at the oscillation frequency f_0 and its first few harmonics, particularly the even harmonics when the I-V curve is antisymmetric about the bias point. The relative strength of these components will determine the efficiency of power conversion from the signal frequency f_S to the intermediate frequency f_I, assuming that $f_S > f_I$. In the fundamental mode of conversion, the signal has frequency $f_S = f_0 \pm f_I$, and in the second-harmonic mode, the signal frequency is $f_S = 2f_0 \pm f_I$. The most efficient conversion should be in the second-harmonic mode at the dc bias point of maximum negative resistance, because this point has approximate antisymmetry in the I-V curve [*ie*, I(V) = -I(-V)]. However, the fundamental mode should achieve its maximum efficiency at bias voltages nearest the regions of greatest curvature, where the Fourier series of g(t) has a predominant coefficient at the oscillation frequency.

The resonant-tunneling self-oscillating mixer has the potential to displace the Schottky diode in many millimeter-wave applications. To do this, it must demonstrate a competitive noise figure, roughly 3 to 6 dB in the microwave region and 6 to 10 dB in the millimeter band. Although noise figures have not yet been studied, measurements of stable resonant-tunneling diodes indicate that they have very low intrinsic noise [13]. In fact, the measured noise power is less than expected from the full shot noise expression, for reasons that are not fully understood. Nevertheless, this low noise figure will undoubtedly work to the benefit of the resonant-tunneling-diode-based self-oscillating mixer. And the resonant-tunneling self-oscillating mixer provides the intrinsic capability to achieve conversion gain. Mixers such as the standard Schottky diode aren't capable of gain and usually show losses of several decibels.

Using the fundamental mode of coaxial resonant tunneling oscillators, we have operated them as mixers in the microwave region. Shown in Fig. 7 is the mixing spectrum of an oscillator with an oscillation frequency of 14.2 GHz, a signal frequency of 8.2 GHz, and an intermediate frequency of 6.0 GHz. The single-sideband conversion loss in this case is just under 6 dB,

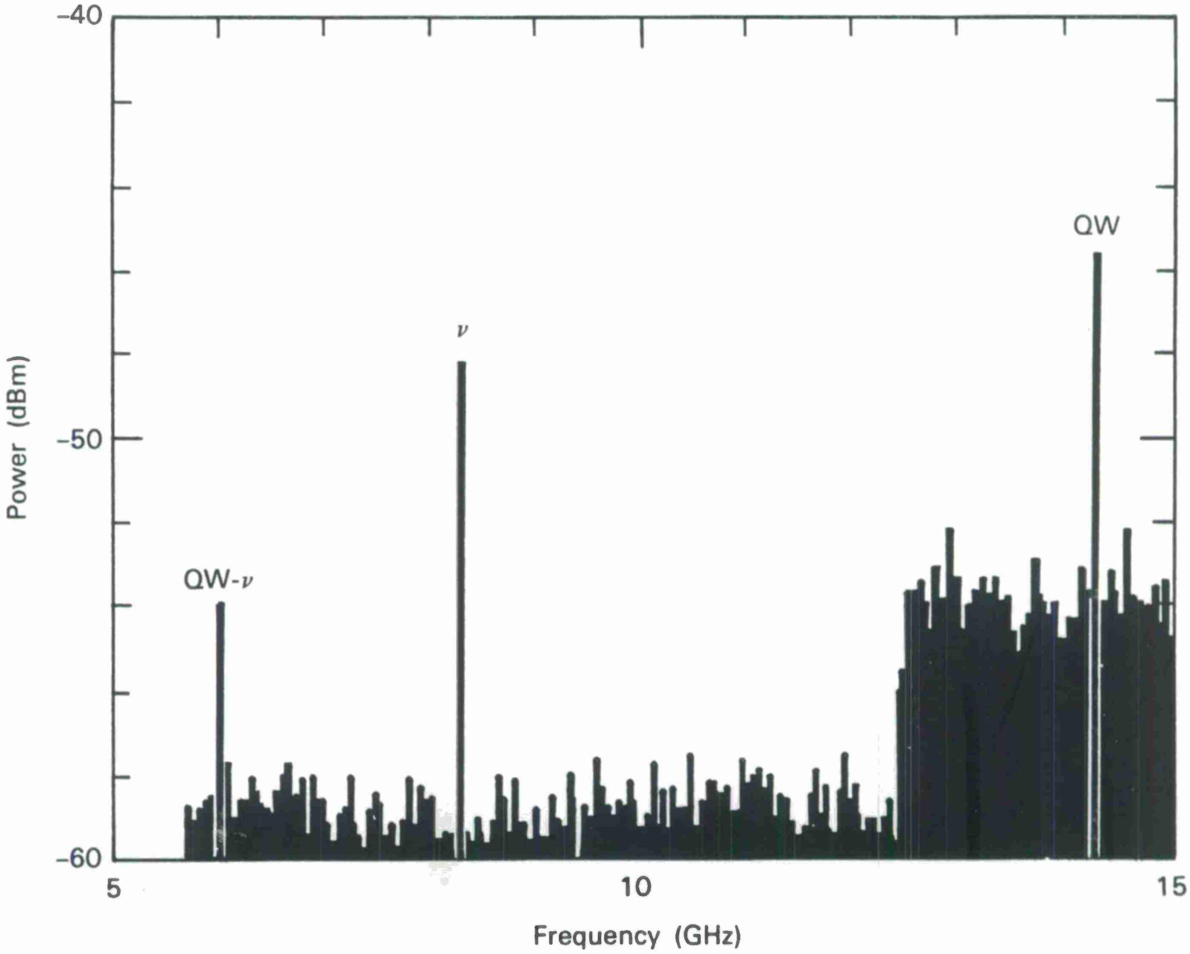

Fig. 7 — The frequency down-conversion of a signal at frequency ν by a double-barrier diode oscillating at the frequency marked QW produces the difference frequency labeled QW-ν.

which is only about 3 dB higher than the best results for room-temperature Schottky-diode mixers in the same frequency region. The experiments on the second-harmonic mode have just begun, using a waveguide oscillator in the millimeter band. The best conversion loss achieved to date is about 12 dB for an oscillation frequency of 50 GHz and a signal frequency of 100 GHz. This performance is comparable to the best results reported for a pair of Schottky diodes in the antiparallel configuration [14].

RESISTIVE MULTIPLIERS

Resonant-tunneling devices excel as resistive multipliers. A resistive multiplier, which is a form of harmonic multiplier, generates power at frequencies that aren't conveniently available from fundamental oscillators. Harmonic multipliers are often used for radio astronomy. In radio astronomy, heterodyne receivers, operating at frequencies above 100 GHz, use power from a harmonic multiplier as a local oscillator source. Harmonic multipliers are also the primary source of power for molecular spectroscopy in the submillimeter wavelength spectrum.

Currently, resistive multipliers usually use Schottky-barrier diodes, but the advantages of resonant-tunneling diodes will promote their use as resistive multipliers. The absence of even harmonics in a resonant-tunneling diode's dynamic conductance simplifies the design of multiplier circuits, particularly in the millimeter-wave region. Also, because of its negative resistance, the maximum theoretical generation efficiency of a double-barrier diode can be significantly higher than an ideal diode's n^{-2} (where n is the harmonic number) [15].

If a resonant-tunneling diode is pumped so that the peak amplitude of the voltage across the diode occurs above the device's resonant-current peak, at least three local maxima in the diode's current waveform will be produced over one cycle. (See Fig. 8 for a theoretical curve.) These maxima correspond to third- or higher-order odd-harmonic generation. The ease with which these higher-order odd harmonics are obtained is due to the presence of a peak and a valley in the diode's I-V curve, as well as the overall antisymmetry of this curve about the origin.

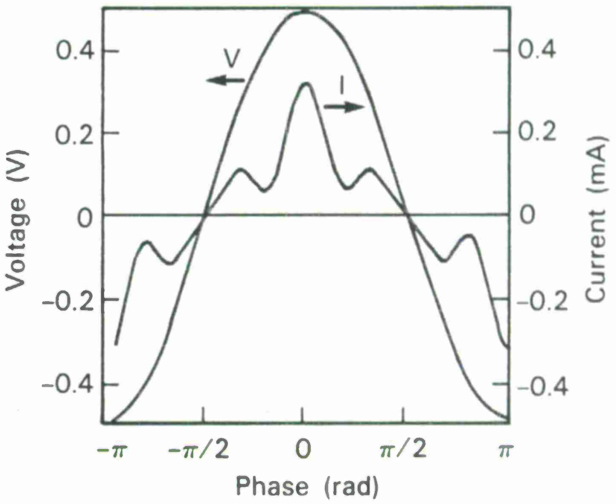

Fig. 8 — Voltage and current waveforms for a double-barrier diode reveal that the local maxima in the current waveform, if equally spaced in phase, should lead to a strong fifth harmonic component in the current-power spectrum.

To demonstrate this odd-harmonic generation, a diode's I-V curve can be modeled with a seventh-order polynomial. Using this model, the diode is assumed to be driven by a source that has an internal impedance less than the minimum negative resistance of the double-barrier diode. Thus the current across the diode is a single-valued function of the drive voltage. The numerically determined current-waveform of an 0.5 V source is shown in Fig. 8. The local maxima in this waveform, if equally spaced in phase, should lead to a strong fifth harmonic component in the current-power spectrum. This spectrum, shown in Fig. 9, predicts that the available fifth-harmonic power will be 0.065 times that of the fundamental.

Figure 10 illustrates the power spectrum obtained for a resonant-tunneling diode that was mounted in a 50 Ω coaxial circuit and pumped at 4 GHz. As expected, even harmonics are absent and the fifth harmonic predominates among the odd harmonics. However, the measured efficiency was only about 0.5%, significantly less than the theoretical prediction of 6.5%. This discrepancy can possibly be attributed to the test circuit, which does not allow

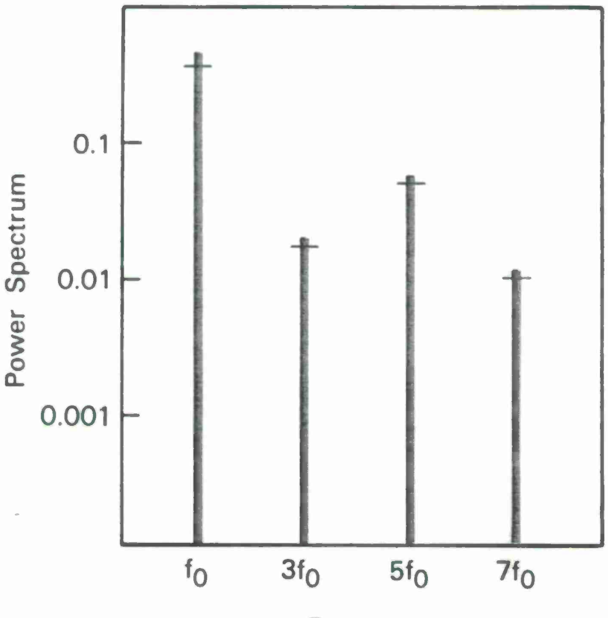

Fig. 9 — A power spectrum corresponding to the voltage-current plot of the Fig. 8.

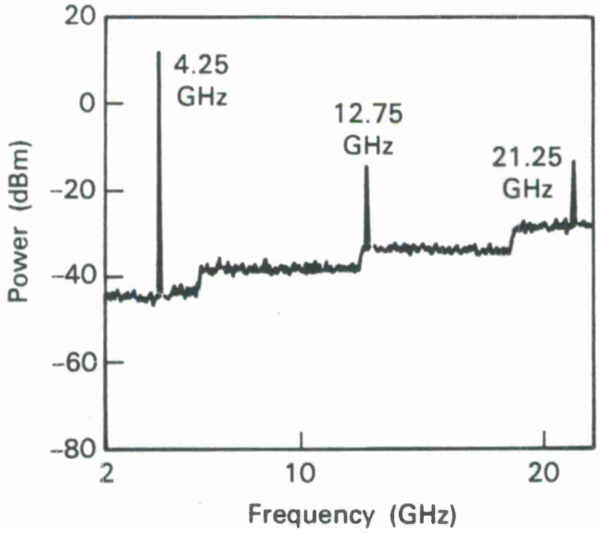

Fig. 10 — A strong fifth-harmonic component was confirmed experimentally for a 4.25-GHz input signal.

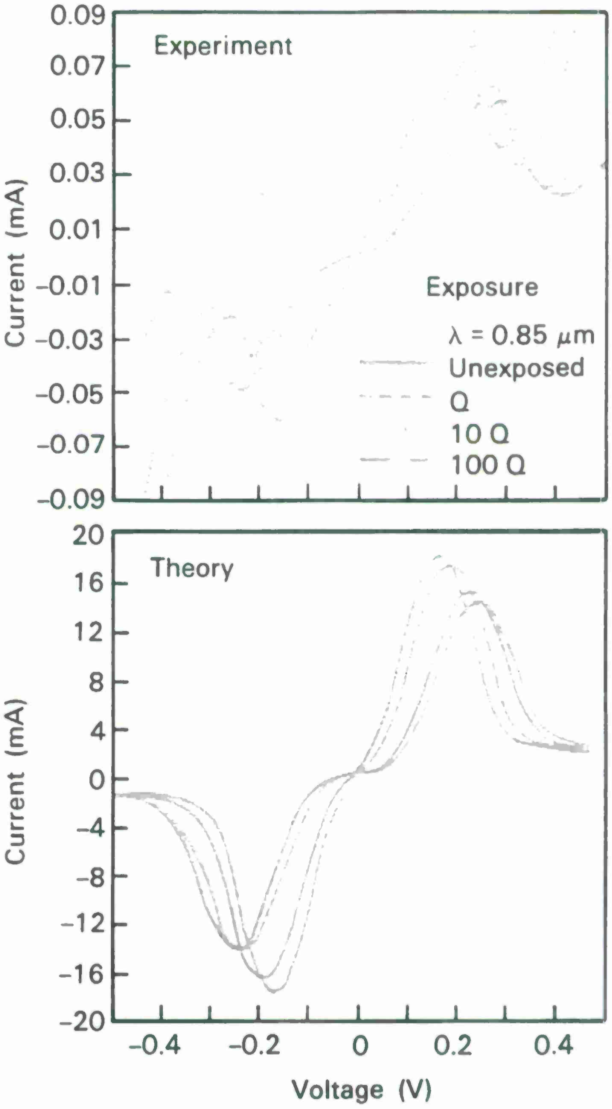

Fig. 11 — Persistent photoconductivity is a characteristic of resonant-tunneling diodes. The experimental results were obtained from a diode that was cooled to 20 K in the dark and then exposed to progressively greater levels of light.

independent tuning of the harmonics. Ideally, the fifth harmonic should be terminated with a resistance greater than the source resistance. But the third harmonic should be terminated with a reactance, which eliminates power dissipation and reinforces the fifth-harmonic voltage. Combining these features in a one circuit will allow independent tuning of the harmonics and greater conversion efficiency for the fifth harmonic.

PERSISTENT PHOTOCONDUCTIVITY AND A RESONANT-TUNNELING TRANSISTOR

A transistor based on a double-barrier resonant-tunneling structure could significantly improve upon the present state of the art. Persistent photoconductivity provides clues to the operation of such a transistor, wherein the well region acts as the device's control electrode.

A resonant-tunneling structure sometimes exhibits persistent photoconductivity [16], that is, the structure's I-V curve shifts with successive exposures to light. Figure 11 illustrates this shift. Photoionization of DX centers in the $Al_{0.3}Ga_{0.7}$ barriers in the structure causes the shift in the I-V curve. (DX centers are lattice vacancies associated with a nearby donor atom. For a detailed discussion of DX centers, see Nelson [17] or Lang *et al* [18].) This photoionization creates a dipole region with fixed positive charge in the barriers and free electrons outside the barriers. Any electrons that reside initially in the well quickly escape because of the higher energy of the confined band edge within the well and the short resonant-state lifetime. The dipoles produce the band bending shown in Fig. 12. The well is lowered in potential by an amount $\Delta\phi$, and the barriers are also lowered. The resulting shifted I-V curve shows a peak transmission that has been moved to a lower voltage by the lowered well and a higher current density caused by the lower effective barriers.

Figure 12 shows that DX centers in the barriers provide a way of adjusting the well potential relative to the outer contact regions. This effect is analogous to the modulation of the base potential of a conventional transistor. In this case, the structure's potential well serves as the control electrode.

The transconductance of such a device, G_m, is related to the change in collector current density, ΔJ_c, and the change in well potential, $\Delta\phi$, by

$$G_m \equiv \frac{\partial I_c}{\partial V_{be}} = \frac{A \Delta J_c}{\Delta \phi} \qquad (3)$$

where A is the emitter area. The shift in the well potential is approximately related to the shift in the current peak ΔV_p by

$$\Delta V_p \approx 4 \Delta \phi \qquad (4)$$

This expression is valid only for the specific diode of Sollner *et al* [19]. One factor of two on the right side approximately accounts for the depletion region on the collector side when biased to the current peak. The other factor of two arises from the base-to-emitter voltage,

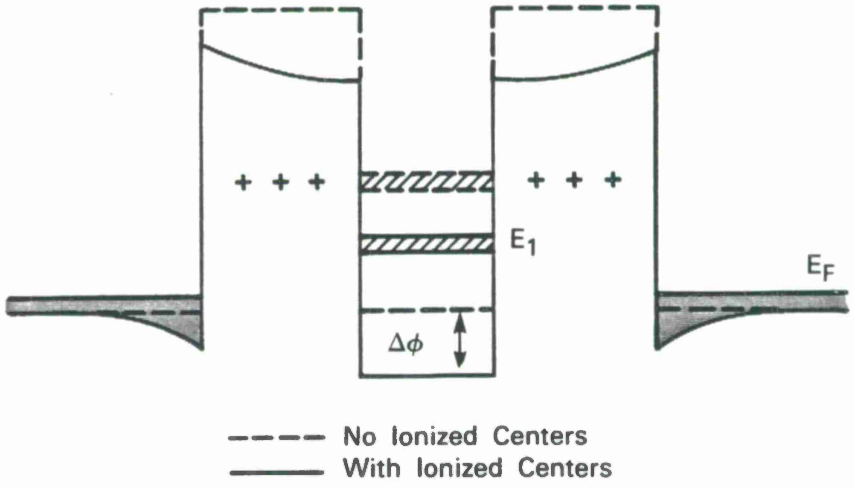

Fig. 12 — Positive charge in the barriers of a double-barrier diode produces band bending (red line); a device without ionized centers has no band bending (black line).

which is, at most, half of that applied between the base and collector. Thus the transconductance becomes

$$G_m = \frac{4A\Delta J_c}{\Delta V_p} \tag{5}$$

But there is one complication. The leakage current also changes with $\Delta\phi$, but this change is probably related to the presence of DX centers in the barriers rather than to the modulation of the well potential. To account for this contribution, we assume that, at voltages below the current peak, the transistor output impedance is large and positive, so we can extrapolate the excess current at high voltage back to zero and keep the output impedance positive. These extrapolations are shown in Fig. 13. Using this figure, an emitter width of 1 μm gives an intrinsic transconductance of 4,000 mS/mm. Specific contact resistances of the order of 10^{-7} Ω cm^2 are necessary to realize such a high extrinsic transconductance.

The frequency above which the small-signal short-circuit current gain drops below unity is

$$f_T = \frac{C}{2\pi G_m} \tag{6}$$

where C is the total input capacitance. Using a 1-μm gate contact and 40-nm n^- regions, we find f_T = 110 GHz.

The maximum frequency of oscillation f_{max} will also depend on the base resistance. For negligible emitter resistance,

$$f_{max} = \frac{f_T}{4R_bC_c} \tag{7}$$

where Rb is the base resistance and C_c is the base-to-collector capacitance. As the base is very thin and lightly doped, it might be expected

Symbols

Units are shown in brackets.

A	Cross-sectional area of a device [cm^2]
C	Capacitance [F]
C_c	Collector capacitance [F]
C_S	Capacitance per unit area [F/cm^2]
E_f	Fermi energy [J]
e	Charge on the electron [C]
f_I	Intermediate frequency [Hz]
f_{max}	Frequency above which the terminal conductance is positive for all voltages, hence maximum oscillation frequency [Hz]
f_O	Output frequency [Hz]
f_S	Signal frequency [Hz]
f_T	Frequency above which the small-signal short-circuit current gain is below unity [Hz]
$f_{\Delta E}$	Frequency corresponding to resonant-state lifetime [Hz]
G_{max}	Maximum negative value of voltage-dependent conductance [S]
G(V)	Voltage-dependent conductance of a resonant-tunneling diode [S]
g(t)	Conductance of a diode modulated by a changing voltage [S]
I	Current [A]
IF	Intermediate frequency [Hz]
J_c	Collector current density [A/cm^2]
J_P	Peak current density [A/cm^2]
n_0	Carrier concentration [cm^{-3}]
P_{max}	Maximum output power obainable from a negative-resistance amplifier [W]
R_b	Base resistance [Ω]
R_i	Current responsivity [A/W]
R_s	Series resistance [Ω]
V	Voltage [V]
V_0	Voltage amplitude [V]
v_m	Voltage at frequency m [V]
Z_A	Antenna impedance [Ω]
Z_D	Device impedance [Ω]
Z_L	Load impedance [Ω]
ΔE	Energy half-width of transmission function [J]
ΔI	Current excursion of negative differential resistance region [A]
ΔE	Change of current [A]
ΔP_{ac}	Change of ac power [W]
ΔV_p	Shift of the voltage of the current peak from ionized charges in the barriers [V]
ΔV	Voltage excursion of negative differential resistance region [A]
$\Delta\phi$	Shift in potential of the well from ionized charges in the barriers [eV]
ϵ	Dielectric constant [F/cm]
γ	Speed index [s/V]
ω	Angular frequency [s^{-1}]
$\phi(x)$	Electrostatic potential energy [eV]

that the base resistance would be high. However, the quantum-well geometry reduces the resistance considerably. Electron mobilities in modulation-doped quantum wells are very high at temperatures less than 100 K. Although this structure is not a modulation-doped well in the usual sense, the base layer near the resonant current peak acquires charge from the transiting carriers without any direct doping [20]. For present samples, the average well-charge density is approximately 10^{17} cm^{-3}.

Using a mobility of 5×10^5 cm^2/V-s for a base carrier density 2×10^{17} cm^{-3} (the best mobility [21] at 50 K), a 1×20-μm emitter, and a 4.0-nm well thickness, the base resistance is less than 10 Ω. This gives an R_bC_c product of about 0.5 ps, resulting in an f_{max} of 330 GHz. Any increase in current density increases f_T and f_{max} proportionately. Theoretically predicted currents are several times higher than presently observed values.

CONCLUSIONS

Much fertile, yet uncultivated, territory remains in the realm of multiple-barrier tunneling. Three-terminal devices are in their infancy, as are devices for digital applications. The possibility of electro-optical effects has received some attention, and several novel devices have resulted [22]. Most structures to date have contained only two barriers, but investigation of the interaction of three or more barriers may yield even more interesting and useful phenomena.

An extension of multiple-barrier structures to the inclusion of many barriers produces a superlattice. Because of domain formation, superlattices have been impractical electrical devices in the past. Many variations remain untested, even unanalyzed. For example, the "CHIRP" superlattice was examined in some detail [23], but only one type of period variation was investigated. The domain formation that has limited this field to date may be overcome with structures that are yet undeveloped.

All of the devices discussed in this paper have been small compared with their operating

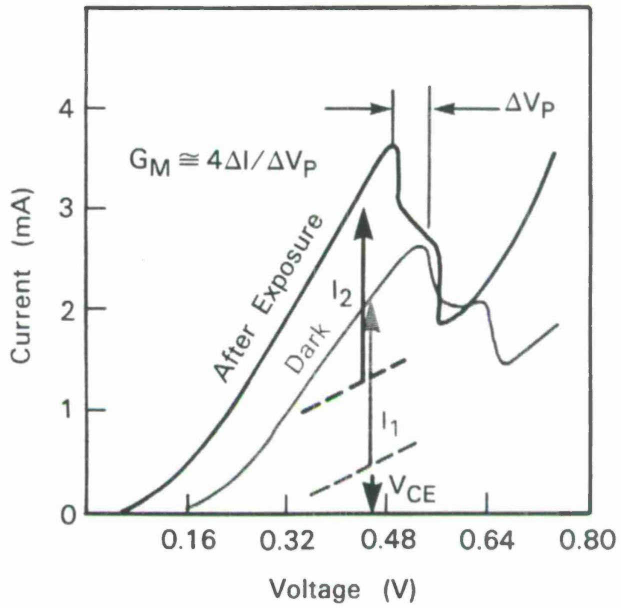

Fig. 13 — These calculated I-V curves for a resonant-tunneling transistor are based upon the assumption that the output impedance of the transistor is large and positive and that the excess current at high voltage can be extrapolated smoothly back to zero.

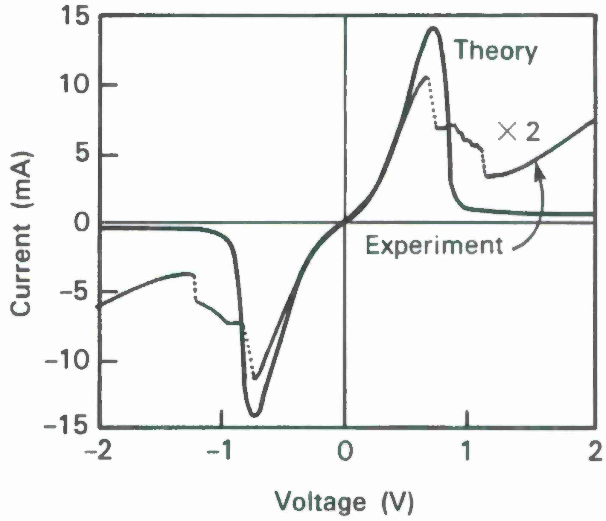

Fig. 14 — The predicted peak-to-valley ratio of a resonant-tunneling device's I-V curve is much greater than that measured for any experimental devices. Improvements in material purity should bring the observed values into closer agreement with the theory.

wavelength. Therefore, they are lumped elements, not transmission media. A bulk material that could provide large, fast impedance nonlinearities would be useful at high frequencies. With two-barrier structures, these nonlinearities are difficult to create, but some variety of superlattice may provide the material necessary for large-scale structures that will find application as traveling-wave devices.

The materials growth that makes possible the high spatial resolution in heterostructure formation is well advanced and progressing rapidly, but much improvement is still possible. Material of sufficient quality for observing reasonable peak-to-valley ratios at room temperature has been available only for two years. Theoretically, as shown in Fig. 14, this peak-to-valley ratio should be much greater. Materials of greater purity could validate most of the assumptions leading to the calculated curve of Fig. 14.

In short, the future of multiple-barrier tunneling structures appears bright, especially in view of the high level of interest in the field. Some of the devices that are just beginning to demonstrate feasibility will be commercially exploited in the next several years and many yet undevised structures will reach the same point in the years to come.

Appendix: Resonant Tunneling Theory

The theory of resonant tunneling is still evolving. The full problem is complicated, involving self-consistent solution of Poisson's equation and the time-dependent Schrödinger equation. The spatial quantization that creates the effects of interest also renders inadequate many of the common approximations used in the solution of these equations. To further complicate matters, scattering from impurities, defects, other carriers, and collective excitations are almost certainly important, but the inclusion of these effects in detail is a difficult theoretical problem. On the positive side, however, the simplest calculations seem to explain the general outline of the experimental observations.

Stationary-State Calculation

The first simplification to make in the analysis of the resonant-tunneling structure is the elimination of time-dependence in the solution of the controlling equations. This stationary-state treatment is based on the approach first applied to finite superlattices by Tsu and Esaki [1]. The calculation shown here incorporates some of our own refinements.

For a first-order solution to the problem, we assume that electrons are the only charge carriers and that they interact only with potential discontinuities in the conduction band. In addition, we use the simplification of the effective-mass model for the electrons. The matching of wave-functions at hetero-interfaces is based on the conservation of probability current, which also accounts for the different effective masses in different semiconductors. We use superposition to determine the potential profile as an electron makes a transit of the structure; the potential is taken as the sum of the potential due to the conduction-band offsets, the applied bias, and any localized charges within the structure. A further, and final, simplifying assumption is that the regions outside the barriers house an electron gas, the field-screening behavior of which is described by the Thomas-Fermi approximation.

The first step in the calculation of a resonant-tunneling I-V curve is the determination of the spatial variation of the electrical potential experienced by the electrons as they transit the double-barrier device under consideration. In addition to the potential change produced by the barrier regions, the electrostatic potential applied by the external (biasing) field produces accumulation and depletion regions that will perturb the potential profile. The spatial dependence of the electrostatic potential, $\phi(x)$, is calculated in the barrier region using the self-consistent Thomas-Fermi equation (cgs units).

$$\phi''(\chi) = \frac{4\pi e n_0}{\epsilon} \left\{ 1 - \left[1 - \frac{e\phi(\chi)}{E_f} \right]^{3/2} \right\} \qquad \text{(A-1)}$$

where E_f is the Fermi energy, ϵ is the dielectric constant, and n_0 is the average volume-doping density. This expression is solved analytically in the regions with nonzero net charge and then matched numerically at the boundaries. In practice, a parabola is fitted to the solution in the cathode to limit the band-bending region. The spatial extent of the fitted region is taken to be about twice the Thomas-Fermi screening length. A potential profile calculated for a double-barrier structure with doping carrier density of 10^{17} cm^{-3} in the outer regions is shown in the Figure.

Once the potential has been found, the transmission coefficient of an electron with a given energy is determined by using the transfer-matrix method and matching boundary conditions. The current is then found by integrating over the incident electron distribution and the density of available final states [1]. The transfer matrix is numerically calculated for an arbitrary parabolic potential profile. To guarantee rapid convergence, the potential is divided into a few (< 10) spatial segments with transfer matrices calculated for each partition.

Even though the cathode contains an accumulation region, we obtain better agreement between the calculated and measured transmission coefficients if we use the equilibrium Fermi distribution of the cathode material and ignore possible tunneling of the accumulated electrons. This agreement between theory and experiment may be due to the improbability of electrons scattering (inelastically) into the accumulation region, which makes the lifetime for tunneling out of the region shorter than the time for scattering in. However, this means that there is much less band bending than has been assumed.

Temporal Behavior

Time evolution of the system has been eliminated from the stationary-state calculation above. But it is possible to find the lifetime of a transiting electron in the resonant state that it occupies while it is between the two barriers. The approach, first derived for atomic and nuclear resonances, is applicable to any resonant state and can be applied to resonant tunneling. The lifetime is given by the uncertainty relation, $\tau = \hbar/\Delta E$; ΔE is the half-width of the peak in the transmission coefficient T(E). Frequencies corresponding to $f_{\Delta E} = (2\pi\tau)^{-1}$ are calculated for the three structures and listed in Table 1.

A time-dependent calculation of the electron distribution has been performed by using the Wigner function approach [20]. The time required to reach equilibrium after an impulse to the system is comparable to that estimated by the resonant-state lifetime. This calculation, however, offers the advantage of predicting the time evolution of the wave functions for all times.

Scattering

A complete time-dependent solution should take account of charge redistribution from applied electric fields and motion of carriers through the depletion and accumulation regions. Scattering plays an important part in these processes, because scattering in the barriers removes the assumed condition of conservation of transverse momentum during tunneling, and scattering in the well region or regions destroys the coherence of a carrier wave function over the structure.

According to Luryi [24], scattering may dominate the charge-transport process through a double-barrier structure. His proposal has led to the development of a second, sequential, model of the double-barrier structure. In contrast to the ballistic model, which maintains the coherence of the wave function across the incoming barrier, the sequential model attempts to incorporate the effects of scattering by eliminating the assumption of phase coherence. This model is called the sequential model because each electron is presumed to enter the structure and tunnel through the first barrier, achieve a resonant state within the structure's potential well, and then exit the structure sequentially by tunneling through the remaining barrier. Luryi proposed that all phase coherence is lost before each electron leaves the structure's potential well and that the negative resistance exhibited by the double-barrier device results from the conservation of momentum. When the peak in the density of states in the well (for momentum perpendicular to the well) is below the conduction band edge of the cathode, electrons can not tunnel into the well.

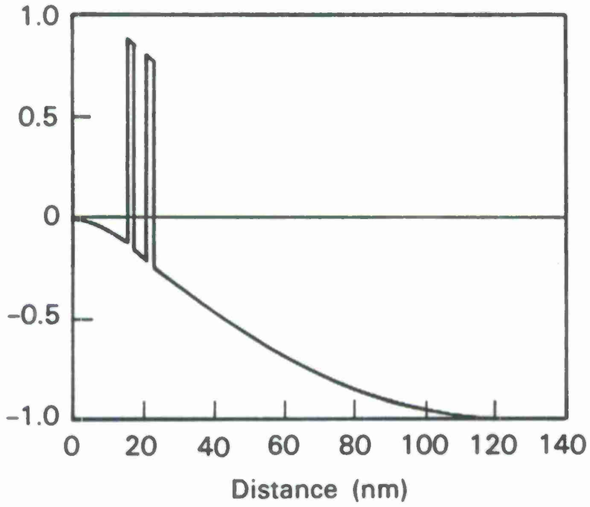

Calculated potential energy of an electron as it transits a double-barrier diode.

Weil and Vinter [25] have recently calculated that the peak current densities should be the same for both the ballistic and the sequential models. It may be, however, that the two models are equivalent as they are presently defined. In their sequential-tunneling calculations, Weil and Vinter use the same boundary conditions as those used for the resonant model (see Ref. 8 in their paper); they maintain the coherence of the wave function across the incoming barrier. The effects of the second barrier enter via the width of the quasibound state in the well, again with a calculation that assumes coherence across the barrier. Perhaps it is not surprising that, with no scattering in the well, the calculations of ballistic and sequential tunneling give the same result.

Weil and Vinter do attempt to include the effects of scattering in the well, via a broadening of the quasibound state. They conclude that, as long as the energy width of this state is small compared to the energy width of the incoming carriers (the usual experimental situation), the lower peak transmission is offset by the additional width. Thus the integral determining the peak current is unaffected. However, the technique of including scattering still implicitly assumes the phase coherence discussed above, even though scattering will generally alter the phase after the scattering event.

This calculation does not appear to be the same as the one originally suggested by Luryi [24] because it does not perturb the phase coherence across the structure. There are also important scattering processes, such as scattering in the barriers, that are not in Luryi's model. Thus the role of scattering remains one of several important unanswered questions in resonant tunneling.

REFERENCES

1. R. Tsu and L. Esaki, "Tunneling in a Finite Superlattice," *Appl. Phys. Lett.* **22,** 562 (1973).
2. L.L. Chang, L. Esaki, and R. Tsu, "Resonant Tunneling in Semiconductor Double Barriers," *Appl. Phys. Lett.* **24,** 593 (1974).
3. T.C.L.G. Sollner, W.D. Goodhue, P.E. Tannenwald, C.D. Parker, and D.D. Peck, "Resonant Tunneling Through Quantum Wells at Frequencies up to 2.5 THz," *Appl. Phys. Lett.* **43,** 588 (1983).
4. M. Tsuchiya and H. Sakaki, "Room Temperature Operation of High-Performance AlAs/GaAs/AlAs Resonant Tunneling Diodes with Atomically Controlled Barrier Width," *IEEE Int. Electron Devices Mtg.*, 662 (1985).
5. T.C.L.G. Sollner, W.D. Goodhue, and H.Q. Le, "Observation of Millimeter-wave Oscillations from Resonant Tunneling Diodes and Some Theoretical Considerations of Ultimate Frequency Limits," *Appl. Phys. Lett.* **50,** 332 (1987).
6. H.R. Fetterman, P.E. Tannenwald, B.J. Clifton, C.D. Parker, W.D. Fitzgerald, and N.R. Erickson, *Appl. Phys. Lett.* **33,** 151 (1978).
7. E.R. Brown, T.C.L.G. Sollner, W.D. Goodhue, and C.D. Parker, "Millimeter-band Oscillations Based on Resonant Tunneling in a Double-barrier Diode at Room Temperature," *Appl. Phys. Lett.* **50,** 83 (1987).
8. C.S. Kim and A. Brandli, "High-frequency High-power Operations of Tunnel Diodes," *IRE Trans. Circuit Theory* **CT8,** 416 (1961).
9. R.F. Trambarulo, *Int. Solid-State Circuits Conf.*, Philadelphia, PA, 1961.
10. P.E. Davis and G. Gibbons, "Design Principles and Construction of Planar Ge Esaki Diodes," *Solid State Electron.* **10,** 461 (1967).
11. D.T. Young, C.A. Burrus, and R.C. Shaw, "High Efficiency Millimeter-Wave Tunnel-Diode Oscillators," *Proc. IEEE* **52,** 1260 (1964).
12. C.A. Burrus, "Gallium Arsenide Esaki Diodes for High-Frequency Applications," *J. Appl. Phys.* **32,** 1031 (1961).
13. E.R. Brown, T.C.L.G. Sollner, and W.D. Goodhue, *Solid State Research Report, MIT Lincoln Laboratory* **1986:1,** 37 (1986).
14. D. Carlson and M.V. Schneider, "Subharmonically Pumped Millimeter-Wave Mixers," *IEEE Trans. Microwave Theory Tech.* **MTT 26,** 706 (1978).
15. C.H. Page, "Harmonic Generation with Ideal Rectifiers," *Proc. IRE* **46,** 1738 (1958).
16. E.R. Brown, T.C.L.G. Sollner, W.D. Goodhue, and C.D. Parker, "Fundamental Oscillations up to 200 GHz in a Resonant-Tunneling Diode," *Device Research Conf.*, Paper IV A 2 (1987).
17. R.J. Nelson, "Long-lifetime Photoconductivity Effect in n-Type GaAlAs," *Appl. Phys. Lett.* **31,** 351 (1977).
18. D.V. Lang, R.A. Logan, and M. Jaros, *Phys. Rev.* B, 1015 (1979).
19. T.C.L.G. Sollner, H.Q. Le, C.A. Correa, and W.D. Goodhue, "Persistent Photoconductivity in Resonant Tunneling Structures: Toward a Resonant Tunneling Transistor," *IEEE/Cornell Conf. Advanced Concepts in High Speed Semiconductor Devices and Circuits*, p. 252.
20. W. Frensley, "Quantum Transport Simulation of the Resonant-Tunneling Diode," *IEEE Int. Electron Devices Mtg.*, Paper 25.5 (1986).
21. A.C. Gossard, "Quantum Well Structures and Superlattices and Their Applications Potential," *Inst. Phys. Conf. Ser.* 69, 1 (1984).
22. F. Capasso, "New Multilayer and Graded Gap Optoelectronic and High Speed Devices by Band Gap Engineering," *Surf. Sci.* **142,** 513 (1984).
23. T. Nakagawa, N.J. Kawai, and K. Ohta, "Design Principles for CHIRP Superlattice Devices," *Superlattices Microstruct.* **1,** 187 (1985).
24. S. Luryi, "Frequency Limit of Double-barrier Resonant-Tunneling Oscillators," *Appl. Phys. Lett.* **47,** 490 (1985).
25. T. Weil and B. Vinter, "Equivalence Between Resonant Tunneling and Sequential Tunneling in Double-barrier Diodes," *Appl. Phys. Lett.* **50,** 1281 (1987).

ACKNOWLEDGMENTS

None of the experimental work described here could have been accomplished without help from staff members skilled in the art of material growth and fabrication. We are especially indebted to W.D. Goodhue for producing excellent quality heterostructures grown by molecular beam epitaxy, for suggesting useful structures, and for overseeing much of the processing. C.L. Chen has also been very helpful in processing, as have G.D. Johnson, K.M. Molvar, W.F. DiNatale, and R.F. Murphy. Expert packaging help has been provided by N. Usiak, D.J. Landers and P.J. Daniels. C.D. Parker has provided considerable expertise with the measurements.

We also owe much to the environment of ideas in which we work. P.E. Tannenwald, B. Lax, C.O. Bozler, A.R. Calawa, B.J. Clifton, M.W. Geis, W.D. Goodhue, M.A. Hollis, R.A. Murphy and H.J. Zeiger at Lincoln Laboratory; F. Capasso and S. Luryi at AT&T Bell Laboratories; W.R. Frensley, R.T. Bate and M.A. Reed at Texas Instruments; M. Heiblum and R.A. Kiehl at IBM; D.D. Coon at the University of Pittsburgh; H. Fetterman at UCLA; H. Sakaki at the University of Tokyo; and L.F. Eastman at Cornell have all contributed to useful technical discussions.

This work was sponsored by the US Army Research Office and by NASA.

T.C.L. GERHARD SOLLNER is a staff member in the Microelectronics Group. During his five years at Lincoln Laboratory, he has concentrated on novel approaches to high-speed devices. Before coming to Lincoln Laboratory, Gerry was an assistant professor at the University of Massachusetts. He received a bachelor's degree in physics from the Georgia Institute of Technology and a doctorate in physics from the University of Colorado. In his spare time, Gerry enjoys windsurfing, cooking, and skiing.

HAN QUANG LE is a staff member in the Quantum Electronics Group. Before joining Lincoln Laboratory two years ago, he worked for the National Magnet Laboratory at MIT. Han received a PhD in physics from MIT. Han's current research is focused on optoelectronics. In his free time, he enjoys exploring wilderness areas.

Large room-temperature effects from resonant tunneling through AlAs barriers

W. D. Goodhue, T. C. L. G. Sollner, H. Q. Le, E. R. Brown, and B. A. Vojak[a)]
Lincoln Laboratory, Massachusetts Institute of Technology, Lexington, Massachusetts 02173

(Received 3 June 1986; accepted for publication 2 September 1986)

At room temperature, we have observed negative differential resistance in AlAs double-barrier structures and a large hysteresis in the current-voltage characteristic of a stack of five AlAs double-barrier structures. The peak-to-valley ratio of the current was as high as 3.5:1 in a double-barrier structure. To the best of our knowledge, this is the largest room-temperature peak-to-valley ratio observed to date in a double-barrier structure and the first report of a room-temperature hysteresis in a stacked structure. These structures were grown by molecular beam epitaxy using thin AlAs barriers in GaAs. Both the first and second resonances were observed, and are well explained by simple tunneling theory assuming a value of 1.0 ± 0.1 eV for the GaAs-AlAs conduction-band discontinuity seen by the tunneling electrons. This value is very close to the difference in conduction-band energy at the Γ points found by using the accepted values of GaAs and AlAs band gaps with 65% of the band-gap difference appearing in the conduction band. This suggests that negligibly few electrons relax to the lower AlAs X valley as they tunnel through the 1.5–2.5-nm-thick AlAs barriers. These results indicate that AlAs should be a high quality barrier material for a variety of heterojunction devices.

Resonant tunneling through double-barrier semiconductor structures has received much interest in the past few years. These structures consist of two semiconductor barriers roughly 10 nm or less thick, embedded in a semiconductor having a smaller band-gap energy than that of the barrier material, and separated by less than about 10 nm. In this way the carriers are confined to the lower band-gap material but can readily tunnel through the thin barriers under applied bias voltage. In 1970 Tsu and Esaki[1] first proposed that a large peak in the tunneling current through the structures should occur when the injected carriers have certain resonant energies. Both Chang *et al.*[2] and Vojak *et al.*[3] observed slight negative resistance from single quantum well and multilayer heterostructures grown by molecular beam epitaxy (MBE) and metalorganic chemical vapor deposition (MOCVD), respectively. In 1983 Sollner *et al.*[4] reported the first observations of resonant tunneling at room temperature and of large regions of negative differential resistance at lower temperatures. Their experiments indicated that the intrinsic response time is shorter than 1×10^{-13} s. Sollner *et al.*[5] also reported microwave oscillations at low temperatures. Recently, Bonnefoi *et al.*[6] have observed resonant tunneling in a MOCVD-grown GaAs/AlAs structure, Shewchuk *et al.*[7] have observed room-temperature resonant-tunneling oscillations and negative differential resistance in MBE-grown GaAs/GaAlAs structures, and Tsuchiya *et al.*[8] have observed room-temperature negative differential resistance from MBE-grown GaAs/AlAs structures.

In this letter we report a variety of resonant tunneling effects observed in GaAs quantum well structures with AlAs barriers. All of the structures were grown by MBE on (100) oriented n^+-GaAs substrates and utilized at least a 1-μm-thick temperature stabilizing GaAs buffer layer. The growth temperature was 560 °C, and the growth rates were about 1.0 μm/h and 0.2 μm/h for the GaAs and AlAs, respectively. Computer-controlled shutters were used during the growth of the barriers and wells of the samples. The wells and barriers were unintentionally doped p type with a net concentration $N_A - N_D \sim 5 \times 10^{14}$ cm^{-3}, while the remaining GaAs was doped n type with silicon to a concentration $N_D - N_A \sim 1 \times 10^{17}$ cm^{-3}. Low resistance contacts were obtained by evaporating and alloying a standard Ni/Ge/Au metallization, and individual mesas were defined on the wafers by ion beam etching. Further details of the fabrication procedure are described elsewhere.[4]

Figure 1 shows the curves of room-temperature current density versus voltage (J-V) for two-terminal devices formed from both a single double-barrier structure with 1.5-nm-thick barriers and a 4.5-nm-thick well, and a stack structure consisting of five double-barrier structures with 1.5-nm barriers and a 4.5-nm well, separated by 80 nm of n-type GaAs having a donor concentration N_D–$N_A \sim 1 \times 10^{17}$ cm^{-3}. As shown in Fig. 1(a), the double-barrier structure exhibited large current densities and high peak-to-valley ratios at room temperature. The current density at the peak of the first resonance is about 4×10^4 A cm^{-2} while the peak-to-valley ratio is about 3.5:1. At 77 K the current density of this sample remained practically the same as above but the peak-to-valley ratio increased to about 10:1. In addition, both the first and second resonances are observed. As shown in Fig. 1(b), the stack also exhibited large current densities at room temperature although a hysteresis effect was observed. This hysteresis effect is presently under further investigation. The transmission peak in the stack was approximately five times higher in voltage than for a single double-barrier structure. This is the expected result if the double-barrier structures in the stack are far enough apart that the electrons can relax in the buffer layers between

---

[a)] AMOCO Research Laboratory, Standard Oil Co. of Indiana, Naperville, IL 60566.

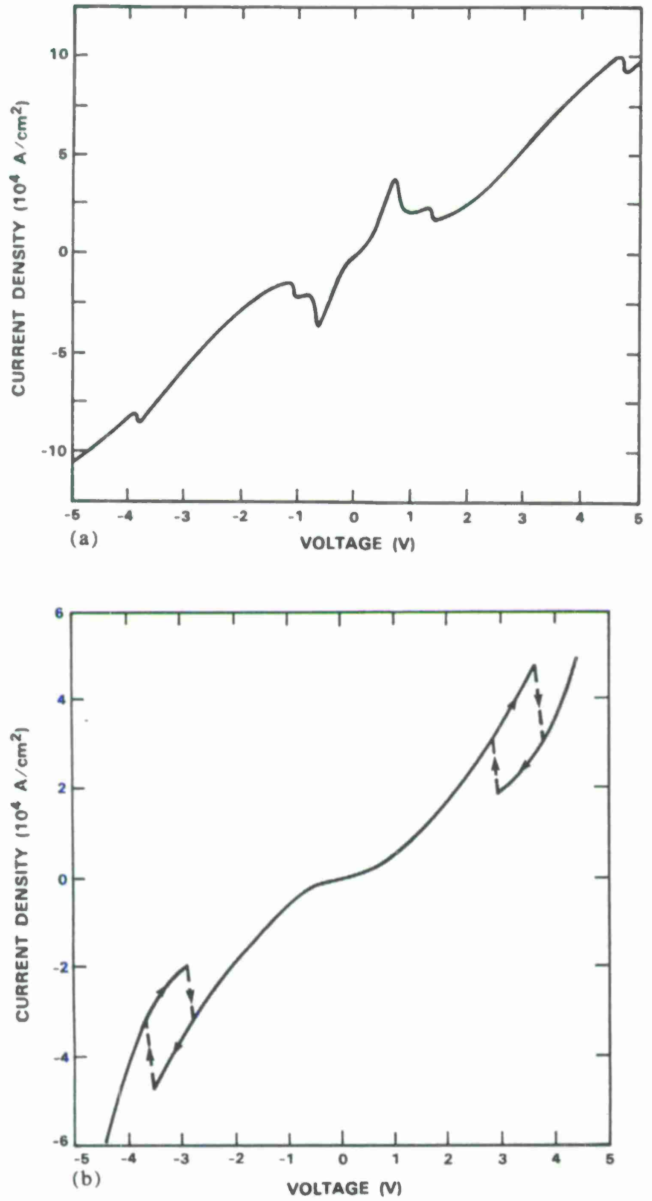

FIG. 1. (a) *J-V* characteristic of an AlAs double-barrier structure with two 1.5-nm barriers and a 4.5-nm GaAs well. Both the first and the second resonances are clearly delineated at room temperature. The chairlike form of the *J-V* curve in the negative resistance region of the first resonance is indicative of electrical oscillation with the measurement circuit. (b) *J-V* characteristic of a stack of five AlAs double barriers, each similar to that of (a), with 80.0 nm of *n*-type GaAs between the pairs. The dashed portion of the curve indicates switching or bistable behavior. The arrows are located on that part of the *J-V* curve which is traced if the hysteretic region is entered with a direction defined by the arrow.

them. Each double barrier then presents the same tunneling transmission coefficient and the structures behave like independent series elements. Further consideration of the stack structure will be given in a future letter.

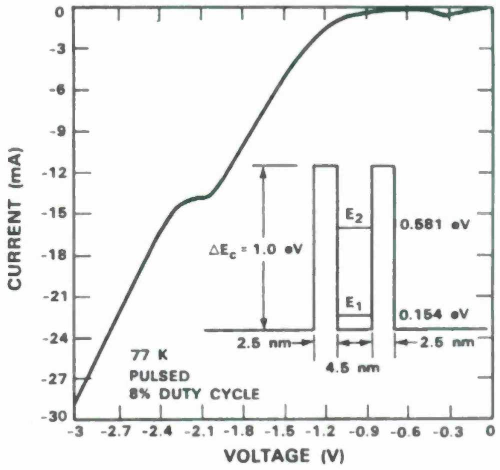

FIG. 2. *I-V* characteristics at 77 K of an AlAs double-barrier structure with 2.5-nm barriers and a 4.5-nm well. The second, higher voltage resonance, which appears as a bump at room temperaure, is clearly delineated at 77 K. The energy levels of the well were calculated from theory using both the *I-V* characteristic and TEM measured thicknesses.

We grew several double-barrier structures having barrier thicknesses between 1.5 and 2.5 nm and well widths between 4.5 and 5.6 nm for analyzing the conduction-band discontinuity between AlAs and GaAs. The dimensions were confirmed to within 10% using transmission electron microscopy (TEM). These devices exhibited resonances at room temperature and a higher voltage resonance became visible at low temperatures. Because of the high current densities generated when operating the devices at the second, higher voltage resonance, the current-voltage (*I-V*)curves for these devices were generated in a pulsed mode. Figure 2 shows the *I-V* characteristic at 77 K of a device with 2.5-nm AlAs barriers and a 4.5-nm GaAs well. Shown in Fig. 3 is a TEM cross-sectional micrograph of this device. The second resonance, which manifests itself only as a small change of curvature at room temperature, becomes a clearly delineated kink in the *I-V* curve at 77 K.

To determine the conduction-band discontinuity between GaAs and AlAs, we analyzed the above *I-V* curves using the resonant tunneling theory described in Ref. 9. Figure 4 shows one important result of this theory: the position

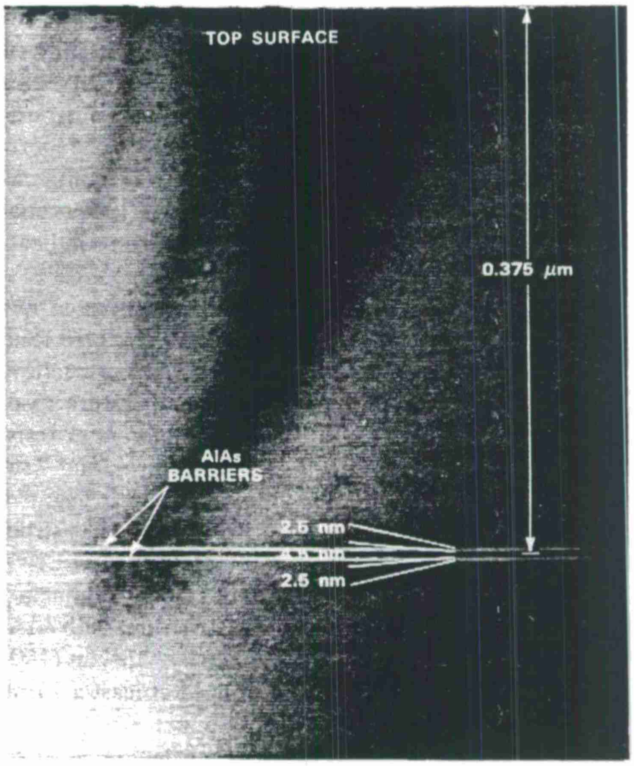

FIG. 3. TEM cross-sectional micrograph of the device of Fig. 2.

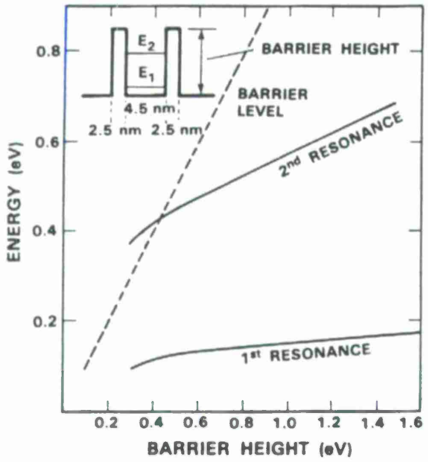

FIG. 4. Diagram showing how sensitive the second, higher voltage resonances of double-barrier structures are to barrier height.

of the second resonance depends much more strongly on the barrier height than does the position of the first resonance, which depends strongly on the well width. This allows us to use the position of the first resonance to fix the well width and the position of the second to determine the barrier height. For the four samples measured with barrier thicknesses between 1.5 and 2.5 nm and wells between 4.5 and 5.6 nm, the best agreement with the theoretical *I-V* curves in each case required a 1.0 ± 0.1 eV conduction-band discontinuity.

Using the known Γ-point energy gaps of 1.424 eV for GaAs and 3.018 eV for AlAs[10] with 65% of the band-gap discontinuity in the conduction band, we calculate the Γ-point discontinuity to be 1.036 eV. This is close enough to our 1.0 eV estimate to strongly suggest that direct Γ-valley tunneling processes are favored over indirect processes in the thin AlAs. This is not surprising since the indirect processes require phonon interactions to conserve transverse crystal momentum or other scattering processes to allow tunneling without momentum conservation. Few if any phonons can be created or absorbed in the thin AlAs barriers because the time that the electron wave packet spends in these regions during tunneling is prohibitively small. On the other hand, impurity or crystal-defect assisted tunneling is certainly present and is thought to be responsible for the rapidly increasing current in the region of the second resonance. The uncertainty in our barrier height determination includes the small shift of the second resonance peak due to the presence of this current component. Our results provide independent support of the 65-35 rule[11] over the older 85-15 rule[12] pertaining to the percentage of Γ-point band-gap discontinuity that appears across the conduction and valence bands, respectively.

Another interesting effect, shown in Fig. 5, is the room-temperature *I-V* characteristic of an asymmetric double-barrier AlAs structure with a 2.5-nm barrier, 4.0-nm well and 5.0-nm barrier. The asymmetry observed in the *I-V* curve is consistent with the theory. It is apparent that many different *I-V* curves can be generated for a variety of devices by varying double-barrier parameters.

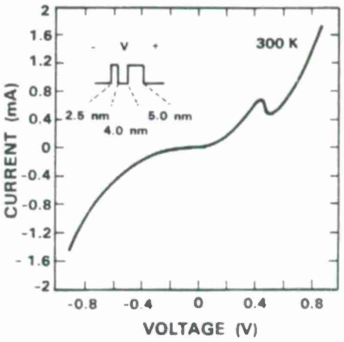

FIG. 5. Room-temperature *I-V* characteristic of an asymmetric AlAs double-barrier structure. The barrier thicknesses are 2.5 nm and 5.0 nm, respectively, and the well width is 4.0 nm.

In summary, we have observed large resonant tunneling effects at room temperature in AlAs double-barrier structures and in a stack of five AlAs double-barrier structures. The peak of the tunneling current is raised to the 2–5 V range in the stacked structure, thereby demonstrating a means of increasing the power handling capacity of devices based on this effect. From the observed first and second resonances in the tunneling current, we have inferred a 1.0 ± 0.1 eV Γ-valley conduction-band discontinuity at the interface between GaAs and thin AlAs barriers. The *X*-valley and *L*-valley band gaps are not important in determining the barrier height for resonant tunneling of electrons through thin AlAs barriers. We have fabricated an asymmetric AlAs double-barrier structure and observed the expected asymmetric *I-V* characteristic. Our resonant tunneling model agrees well with both *I-V* characteristics and TEM thickness measurements of the structures. Our experiments indicate that GaAs-AlAs double-barrier structures can be grown with high quality interfaces and with properties that appear potentially useful for a variey of devices.

The expert technical assistance of G. D. Johnson, C. A. Correa, C. D. Parker, and J. W. Bales is gratefully acknowledged. This work was sponsored by the Department of the Air Force.

[1] R. Tsu and L. Esaki, Appl. Phys. Lett. **22**, 562 (1973).
[2] L. L. Chang, L. Esaki, and R. Tsu, Appl. Phys. Lett. **24**, 593 (1974).
[3] B. A. Vojak, S. W. Kirchoefer, N. Holonyak, Jr., R. D. Dupuis, P. D. Dapkus, and R. Chin, J. Appl. Phys. **50**, 5830 (1979).
[4] T. C. L. G. Sollner, W. D. Goodhue, P. E. Tannenwald, C. D. Parker, and D. D. Peck, Appl. Phys. Lett. **43**, 588 (1983).
[5] T. C. L. G. Sollner, P. E. Tannenwald, D. D. Peck, and W. D. Goodhue, Appl. Phys. Lett. **45**, 1319 (1984).
[6] A. R. Bonnefoi, R. T. Collins, T. C. McGill, R. D. Burnham, and F. A. Ponce, Appl. Phys. Lett. **46**, 285 (1985).
[7] T. J. Shewchuk, P. C. Chapin, P. D. Coleman, W. Kopp, R. Fischer, and H. Morkoç, Appl. Phys. Lett. **46**, 508 (1985).
[8] M. Tsuchiya and H. Sakaki, *IEEE International Electron Devices Meeting Technical Digest* (IEEE, New York, 1985), pp. 662–665.
[9] T. C. L. G. Sollner, H. Q. Le, C. A. Correa, and W. D. Goodhue, Appl. Phys. Lett. **47**, 36 (1985).
[10] H. C. Casey, Jr. and M. B. Panish, *Heterostructure Lasers, Part A: Fundamental Principles* (Academic, New York, 1978), p. 193.
[11] D. Arnold, A. Ketterson, T. Henderson, J. Klem, and H. Morkoç, Appl. Phys. Lett. **45**, 1237 (1984).
[12] R. Dingle, *Festkörperprobleme XV—Advances in Physics* (Pergamon, New York, 1975), p. 21.

Fundamental oscillations up to 200 GHz in resonant tunneling diodes and new estimates of their maximum oscillation frequency from stationary-state tunneling theory

E. R. Brown, W. D. Goodhue, and T. C. L. G. Sollner
Lincoln Laboratory, Massachusetts Institute of Technology, Lexington, Massachusetts 02173-0073

(Received 30 December 1987; accepted for publication 5 April 1988)

Fundamental oscillations have been measured up to 200 GHz in resonant-tunneling diodes at room temperature. Oscillations in the range 102–112 GHz were achieved with diodes mounted in a WR-6 waveguide resonator, and the peak output power in this range was approximately 5 μW. The same diodes oscillated between 192 and 201 GHz and generated about 0.2 μW when mounted in a WR-3 resonator. The estimated maximum oscillation frequency ($f_{\max}$) for these devices is 244 GHz, assuming the average drift velocity across the depletion layer to be 4×10^7 cm s^{-1}. This estimate has been obtained from a new phenomenological theory of the negative differential conductance which accounts for the frequency-dependent spreading resistance and transit-time delay. The theory is also used to show that diodes having $f_{\max}$ exceeding 600 GHz are feasible simply by modifying the doping profile in the regions on either side of the double-barrier structure.

I. INTRODUCTION

Several experimental and theoretical studies of resonant-tunneling oscillators have been conducted since the first microwave[1] and room-temperature[2] oscillation results were obtained. In a recent letter we reported the first millimeter-band oscillations based on the negative differential conductance (NDC) of double-barrier diodes at room temperature.[3] We also emphasized that two of the important requirements for fast diodes, high NDC and low specific capacitance, would be achieved by using thin AlAs barriers with moderate doping outside of these barriers. AlAs was the material of choice for the barriers because it yielded a large room-temperature peak-to-valley ratio, an important requirement for large NDC. The barriers were made thin (1.7 nm) to compensate for the large Γ-point AlAs-GaAs conduction-band offset ($\cong$1.0 eV) and to allow for high peak current density.[4] Thin barriers also decrease the lifetime of the tunneling electron in the quasibound state of the region (quantum well) between the barriers, which further increases the frequency limit imposed by this lifetime.[5] Our previous results led to the prediction that the fastest device could oscillate up to 186 GHz. The measurement of oscillations up to 201 GHz, as reported here, has compelled us to derive a new estimate of $f_{\max}$ using the more sophisticated analysis of the double-barrer diode described here.

II. EXPERIMENT

The diodes studied here were taken from the same wafer that yielded the highest frequency oscillations in our previous work.[3] In brief, these diodes consist of two 1.7-nm-thick (three lattice constants), undoped-AlAs barriers separated by a 4.5-nm-thick quantum well made of undoped GaAs. Outside of each barrier is a 0.5-μm-thick layer of n-GaAs, doped to 2×10^{17} cm^{-3}. The entire structure was grown by molecular-beam epitaxy (MBE) on an n^+ substrate at 560 °C.[4] This growth temperature is lower than those usually applied in MBE and was used here to suppress the rapid diffusion of Al and Si. This yields sharper interfaces and cleaner barrier material,[6] and is likely the reason for the large room-temperature peak-to-valley ratio (3.5:1) of the present device. Devices were fabricated with a standard sequence of steps, including patterning of Ni/Ge/Au layers into dots on the epitaxial side of the wafer, followed by alloying of these layers to make ohmic contacts. Individual mesas were defined by chlorine ion-beam-assisted etching using the patterned metal as a mask.[7] The wafer was then diced into chips (~0.018 cm squares) and mounted in the millimeter-wave resonator.

The resonator structures used to obtain the oscillations above 100 GHz are represented schematically in Fig. 1(a). In this structure the device chip is mounted in the gap between the bottom of a whisker post and the floor of a standard-height rectangular waveguide. The gap is a radial transmission line that is terminated at its periphery by a high impedance, and the diameter of the post is such that the first radial-line resonance occurs slightly above the cutoff frequency (f_C) of the waveguide. In the vicinity of this resonance the behavior of the radial line is well approximated by the series combination of L and C_G shown in Fig. 1(b). A backshort placed behind the diode provides limited tuning of the oscillation power and frequency. The dc bias is provided through a coaxial line that also serves to stabilize the diode at all frequencies below the band of interest.

Some oscillation results obtained in these resonators are shown in Fig. 2, along with the results obtained at lower frequencies with diodes from the same wafer. Oscillations between 102 and 112 GHz were obtained with a single diode in a WR-6 waveguide ($f_C = 91$ GHz). In this structure, the post diameter was 0.063 cm and the height of the gap was about 0.035 cm. A 50% scaled-down version of this resonator in WR-3 waveguide ($f_C = 174$ GHz) then yielded oscillations from 191 to 201 GHz. For both of these resonators, the frequency was varied primarily by changing the bias voltage within the NDC region. The frequency was measured

0021-8979/88/151519-11$02.40

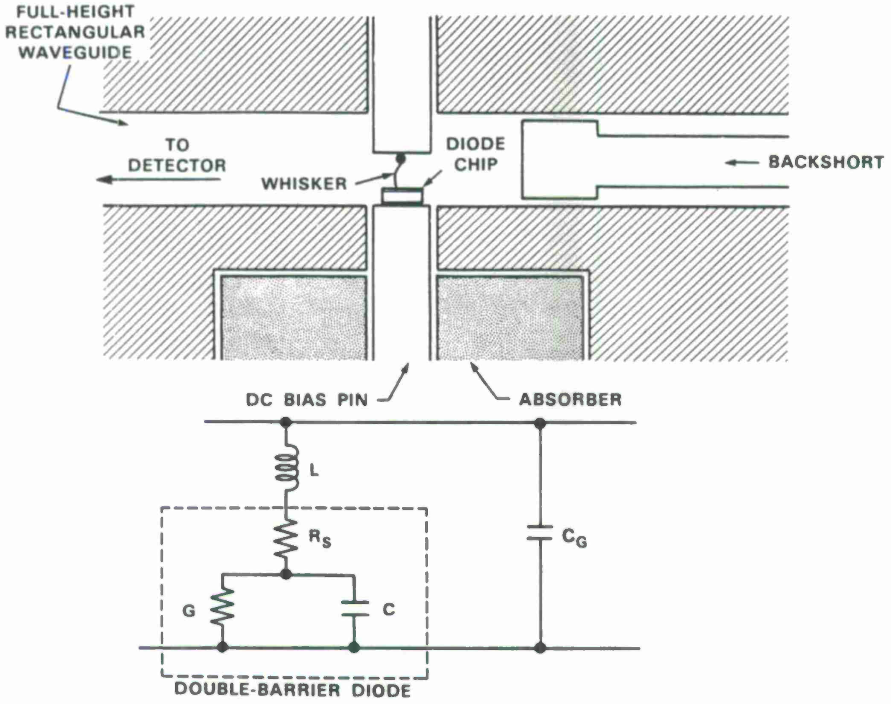

FIG. 1. (a) Schematic diagram of rectangular waveguide resonator used to generate 100- and 200-GHz oscillations with resonant-tunneling diodes. (b) Resonator equivalent circuit with L and C_G determined by the radial waveguide below the whisker post.

with wavemeters, and the power was measured with calibrated Schottky diode detectors.

The frequency of all of these oscillations could also be varied somewhat by moving the backshort, even from positions located many guide wavelengths behind the diode. This provides strong evidence that fundamental oscillations have been observed, as opposed to harmonics of an oscillation at a lower frequency. If the oscillations were second or higher harmonics, then the fundamental would be well below f_C and thus would be unaffected by the position of the backshort. This argument rests on the fact that the output power of the second and all higher harmonics is considerably weaker (at least 10 dB or so) than that of the fundamental. The oscillation frequency is then determined almost entirely by the circuit impedance at the fundamenal frequency.

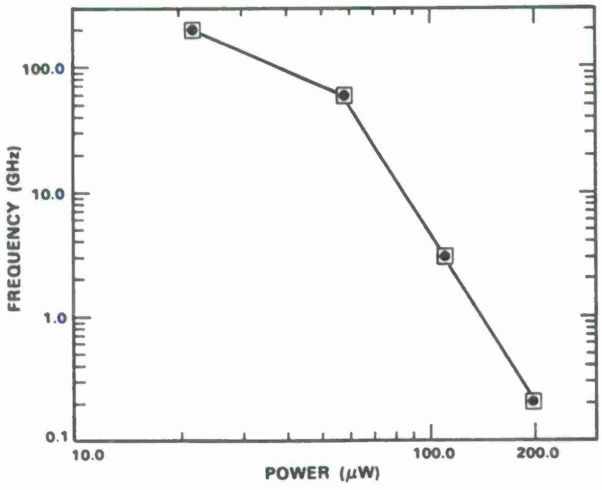

FIG. 2. Room-temperature oscillation results obtained to date with present samples.

Although the power falls very rapidly with frequency, it is clear from the highest frequency data point in Fig. 2 that the $f_{\max}$ of this device must be above 200 GHz. This is higher than our previous, conservative estimate for the same device (187 GHz). Therefore, we will now calculate $f_{\max}$ more carefully and consider ways to further increase it.

III. THEORY

As previously described, $f_{\max}$ is the highest frequency at which a particular diode can oscillate, independent of the circuit. An upper bound on $f_{\max}$ can be found using the lumped equivalent circuit shown in Fig. 1(b), consisting of a (negative) differential conductance G, a parasitic series resistance R_S, and a capacitance C. If we assume that all of the elements are frequency independent, the real part of the terminal impedance of this circuit is negative up to a frequency given by

$$f_R = (2\pi C)^{-1}\left(-\frac{G}{R_S} - G^2\right)^{1/2}. \qquad (1)$$

In all double-barrier diodes of interest, both R_S and C are also nearly independent of bias voltage throughout the NDC region, but G varies rapidly from a maximum negative value $G_{\max}$ near the center of the NDC region to zero at the peak and valley points. Therefore, we consider f_R as a function of G only, and find that it gives a maximum value $f_{\max} = (4\pi C R_S)^{-1}$ for $G = (-2R_S)^{-1}$. If the diode of interest is such that $G_{\max} < (-2R_S)^{-1}$ (as is often the case in practice), then $f_{\max} = f_R(G_{\max})$.

The circuit element that varies the most across a wafer is R_S. For the most part this reflects nonuniformities in the contact metallization. A more consistent component of R_S is the resistance of the undepleted eipilayers (total thickness L_e) on both sides of the heterostructure. A third important component of R_S is the resistance caused by the spreading of the current from the mesa into the much wider substrate. At low frequencies and in a mesa that is etched well into the low-resistivity substrate material, this spreading resistance can be well approximated by $\rho_s/(2d)$, where ρ_s is the substrate resistivity and d is the mesa diameter.[8] This leads to the following expression for the total series resistance,

$$R_S = [(\rho_c + \rho_e L_e)/A] + (\rho_s/2d), \qquad (2)$$

where A is the mesa area, ρ_c is the specific contact resistance, and ρ_e is the epilayer resistivity. At frequencies high enough that the skin depth δ in the substate is much less than the effective diameter b of the chip, the spreading resistance is increased. Assuming also that the skin depth is much less than the chip thickness h but much greater than the mesa diameter, one can write[9]

$$R_S(f) = \frac{\rho_c + \rho_e L_e}{A} + \frac{\rho_s}{\pi\delta}\left[0.5\ln\left(\frac{b}{d}\right) + \frac{h}{b}\right]. \qquad (3)$$

The geometrical parameters in this expression are shown in Fig. 3. Equation (3) is frequency dependent through the behavior of the skin depth. We will apply the standard planar formula, $\delta = [2\rho/(\mu\omega)]^{1/2}$, where μ is the permeability and ω is the angular frequency. In any case, the zero-resistance frequency f_R is now the solution to the equation

$$f_R = (2\pi C)^{-1}\left(-\frac{G}{R_S(f_R)} - G^2\right)^{1/2}. \qquad (4)$$

The solution will be determined later in our analysis of diode $f_{\max}$.

The differential conductance of the present device has not been measured accurately because the observed current-voltage (I-V) curve of this device in the NDC region is always discontinuous, even when it is not oscillating at a frequency above f_C. The most likely cause of this is a spurious oscillation in the dc bias line, which can occur if a stronger oscillation does not exist in the desired frequency range. Because a true I-V curve could not be measured, we previously estimated G by scaling the value obtained from the continuous I-V curve of a much slower device. Shown in Fig. 4 is the I-V curve of such a diode that was stabilized in a coaxial mount (the material parameters of this diode are those of wafer 1, Ref. 3). This is also a diode for which we know the series resistance to be negligible (i.e., $R_S \ll -G_{\max}$). Measurement of the slope yields $G_{\max} = -2.1\,\Delta I/\Delta V$, where $\Delta I = I_P - I_V$, $\Delta V = V_p - V_V$, and the subscripts P and V refer to the peak and valley points, respectively. Applying this same prefactor to the present device gives $G_{\max} = -15$ mS for the best $\Delta I/\Delta V$ ratio observed, and $G_{\max} = -11$ mS for the worst ratio observed.

The differential conductance can also be obtained theoretically from the single-particle, stationary-state model of tunneling. In this model the electrical current through the structure is found by summing the probability-current transmission coefficient over the occupied states on the cathode side of the structure. Each state is weighted by the longitudinal velocity in that state, $v = \hbar^{-1}dE/dk_L^c$, where E is the kinetic energy and k_L^c is the longitudinal component of crystal momentum on the cathode side. This procedure leads to the following expression for the magnitude of the current density[10,11]:

$$J = \beta\int_0^\infty dE_L\,\frac{k_L^a}{k_L^c}\,T^*T(E_L,V_W)$$
$$\times\ln\left(\frac{1+\exp(E_F^c + eV_A - E_L)/kT}{1+\exp(E_F^a - eV_W - eV_D - E_L)/kT}\right), \qquad (5)$$

where E_L is the longitudinal component of kinetic energy of electrons measured just to the cathode side of the double-barrier structure, k_L^a is the longitudinal crystal momentum on the anode side of the structure, $\beta = em^*kT/2\pi^2\hbar^3$, and as shown in Fig. 5, V_W is the potential difference across the structure, V_D is the potential difference across the depletion layer on the anode side, and E_F^c (E_F^a) is the Fermi energy on the cathode (anode) side measured relative to the conduction-band edge in the neutral region on that side. The quanti-

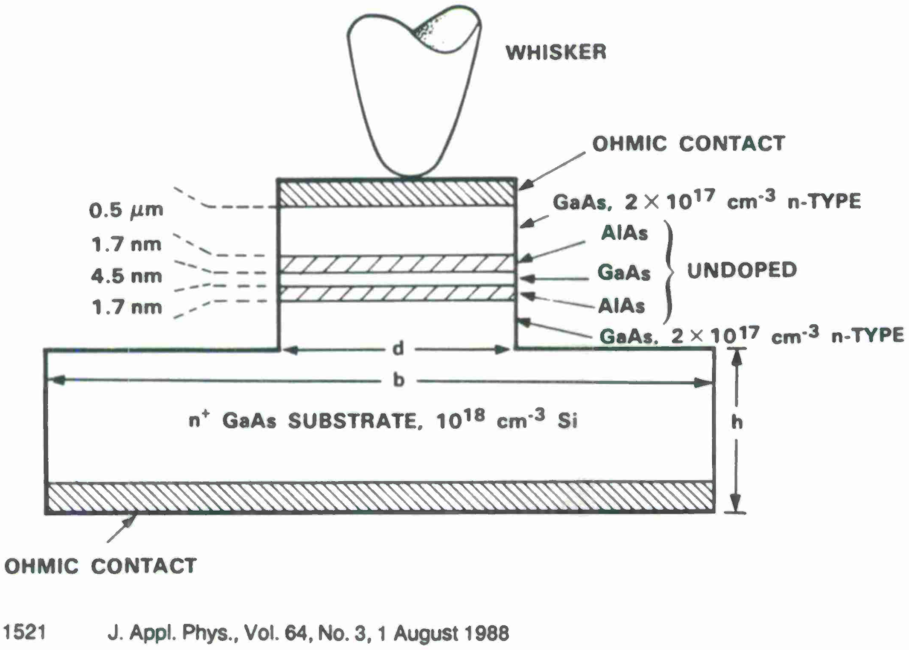

FIG. 3. Cross-sectional view of present diode mesa. The dimensions d, b, and h are not drawn to scale for clarity.

ty T^*T is the particle transmission coefficient through the structure, and is assumed to be independent of the transverse energy and crystal momentum in the derivation of Eq. (5). In the case of resonant tunneling, T^*T has one or more sharp peaks as a function of E_L, and the position of these peaks generally falls to lower E_L as V_W is increased. Each of these peaks is conveniently represented by a (quasibound) level in the double-barrier structure, as is done for the lowest T^*T peak in Fig. 5. At the cathode end of the structure, this level occurs at the value of E_L equal to the energy E_P of the center of the peak. The extension of this level through the entire double-barrier structure delineates the fact that the total longitudinal energy is conserved in the resonant tunneling process.

When increasing bias voltage causes the center of the first T^*T peak to fall near the conduction-band edge or near the upper edge of any other gap in the density of states on the cathode side, the current density given by Eq. (5) should display a corresponding maximum with an NDC region on its high-voltage side. To accurately predict the position of this maximum and the magnitude of the negative conductance, we must account for the band bending in the active regions of the device. The diagram in Fig. 5 shows qualitatively the spatial variation of the conduction-band edge at a bias voltage near the first current-density peak. In the depletion layer on the anode side of the structure, the electron potential energy is quadratic, reflecting the fact that the present devices have a uniform doping concentration on the anode side over a distance significantly longer than the depletion length under bias D. The potential in the double-barrier structure is linear since this region is nominally undoped and is assumed to have negligible mobile space charge density from tunneling electrons. This assumption will be verified later. The potential profile in the accumulation layer is not so straightforward. A numerical solution to Poisson equation indicates that the length of this layer is approximately 30 nm and that eV_A is close to 100 meV for the device shown in Fig. 3 at room temperature and at bias voltages in the NDC region. This solution was obtained by assuming that the electrons are distributed in a three-dimensional continuum throughout the layer. However, the solution to the single particle Schrödinger's equation indicates that an accumulation layer having these dimensions would yield a maximum single-electron quasibinding energy of only about 10 meV. This leads us to suppose that there is a minimum energy level below which electron states do not exist, and that this level is only slightly less in energy than the neutral band edge on the cathode side. For simplicity in the present calculations, we will assume that the minimum energy occurs *exactly* at the neutral band edge shown in Fig. 5. If we make the additional, reasonable assumptions that $e(V_W + V_D) \gg E_F^a$ and $e(V_W + V_D) \gg kT$, the current density integral can be written

$$J = \beta \int_{eV_a}^{\infty} dE_L (k_L^a/k_L^c) T^*T(E_L, V_W) \times \ln\left[1 + \exp(E_F^c + eV_A - E_L)/kT\right]. \tag{6}$$

For the particle transmission probability, we adopt the Breit–Wigner resonant form,

$$T^*T = (k_L^c/k_L^a)\Gamma_0^2\left[(E_L - E_P)^2 + \Gamma_0^2\right]^{-1},$$

where Γ is the half-width at the half-maximum value.[12] Strictly speaking, this expression is only an upper limit on the transmission probability as required by unitarity.[13] Nevertheless, we apply it in lieu of a more accurate numerical method because it leads to a closed-form expression for the current density, and because it can analytically account for the effects of band bending and scattering. It we use the model shown in Fig. 5, the band bending causes E_P to decrease with V_W almost exactly as $eV_W/2$, and therefore causes it to decrease with V_D as $E_P = E_0 - \alpha V_D^{1/2}$, where E_0 is the peak of the T^*T curve (i.e., the quasibound state energy) at zero bias, $\alpha = eW(eN_D/2\epsilon)^{1/2}$, W is the width of the double-barrier structure, and ϵ is the dielectric constant in the anode region. In deriving this expression the dielectric constant in the barriers was set equal to ϵ. The error caused by this as-

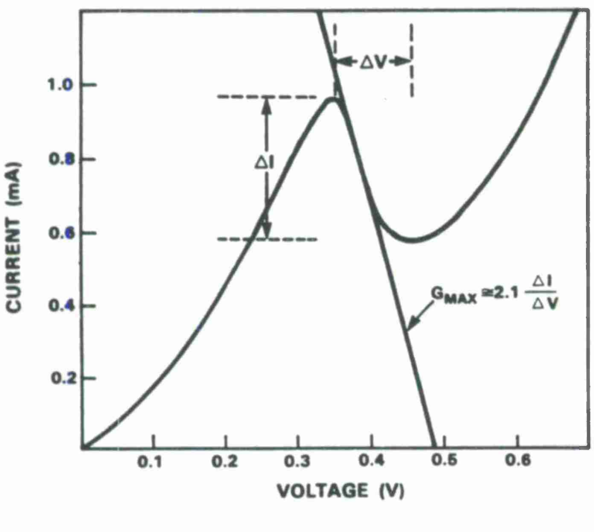

FIG. 4. *I-V* curve of separate device stabilized throughout the negative-conductance region.

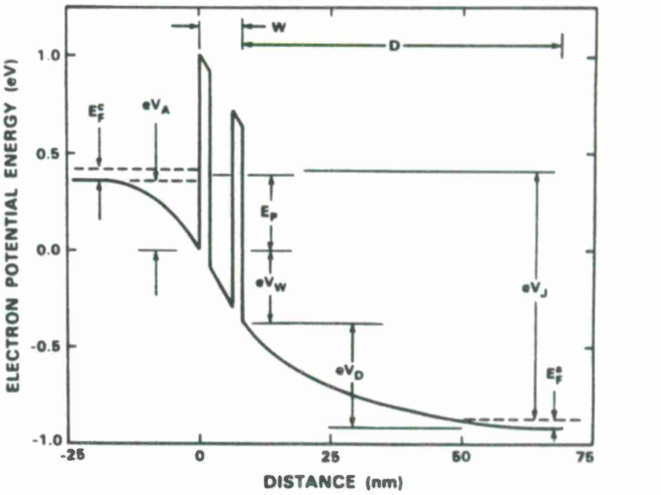

FIG. 5. Electron potential energy at the conduction-band edge of the present device near the bias voltage required for the first current peak. The potential-energy drop eV_A across the accumulation layer is exaggerated for clarity.

sumption will be negligible in the present devices because of the thinness of the barriers in these devices.

Scattering can be accounted for by generalizing the recent result of Stone and Lee,[14]

$$T^*T = \frac{k_L^c}{k_L^a}\frac{\Gamma_0}{\Gamma_T}\frac{\Gamma_T^2}{(E_L - E_P)^2 + \Gamma_T^2}, \tag{7}$$

where $\Gamma_T = \Gamma_0 + \Gamma_S$, and Γ_S is related to the scattering time τ_s through the relation $\Gamma_S = \hbar/\tau_s$. For the present double-barrier structures $\Gamma_T \ll kT$ at room temperature, so that we can treat the logarithmic term as a constant, evaluate it at the peak of T^*T, and approximate the current integral in Eq. (6) as

$$\begin{aligned} J = {} & \beta\Gamma_0\{\pi/2 + \tan^{-1}[(E_P - eV_A)/\Gamma_T]\} \\ & \times \ln\{1 + \exp[(E_F^c + eV_A - E_P)/kT]\}. \end{aligned} \tag{8}$$

The differential conductance is related to the current density by $G = A\,dJ/dV_J$, where

$$V_J = V_D + V_W + V_A + (E_F^c - E_F^a)/e.$$

Upon differentiating Eq. (8) we find

$$\begin{aligned} G = {} & \beta\Gamma_0 A \frac{dE_P}{dV_J} \\ & \times \left[\frac{\Gamma_T \ln\{1 + \exp[(E_F^c + eV_A - E_P)/kT]\}}{\Gamma_T^2 + (E_P - eV_A)^2}\right. \\ & \left. - \frac{\pi/2 + \tan^{-1}[(E_P - eV_A)/\Gamma_T]}{kT\{\exp[(E_P - E_F^c - eV_A)/kT] + 1\}}\right]. \end{aligned} \tag{9}$$

As has been noted previously,[15] the current density is largely independent of the scattering width Γ_S provided that $\Gamma_S \ll E_F^c$. However, in the NDC region, the expression for G depends strongly on this parameter. This is to be expected, since in this model the NDC occurs as the bias voltage drives E_P below eV_A. Thus, the *I-V* curve in the NDC region reflects the shape of T^*T and how it decreases with V_J.

The calculation of the capacitance in the lumped-circuit model is straightforward. If we assume that no charge exists in the double-barrier structure, that the depletion approximation is valid on the anode side, and that the dielectric constant ϵ is uniform throughout the active region, the solution to Poisson's equation yields

$$D + W = [W^2 + (2\epsilon/eN_D)(V_J - V_A)]^{1/2}. \tag{10}$$

The capacitance of these regions is given by $C_{DW} = \epsilon A/(D + W)$, and the total device capacitance is $C = C_A C_{DW}/(C_{DW} + C_A)$, where C_A is attributable to the accumulation layer. Because C_A should exceed C_{DW} by about a factor of 10, its contribution will henceforth be ignored and we will assume the total capacitance to be equal to C_{DW}. Confidence in the depletion approximation is provided by the fact that the peak current density J_P through the present devices is typically less than 4×10^4 A cm^{-2}, so that the mobile space-charge density under bias ($J_P/ev_d = 1.2\times10^{16}$ cm^{-3} for $v_d = 2\times10^7$ cm s^{-1}) is far less than the background doping concentration, $N_D = 2\times10^{17}$ cm^{-3}. The assumption of an uncharged quantum well is definitely good near the current valley, but as the bias point approaches the current peak, the well should be charged maximally by tunneling electrons. The magnitude of this charge will be evaluated later for one particular diode.

At oscillation frequencies for which the period is comparable to the time of electron transit across the total depletion length, the lumped circuit analysis becomes inaccurate and should be replaced by a distributed theory. Since we are only interested here in maximum oscillation frequencies (near which the oscillation power is necessarily weak), we adopt the *small-signal* transit time theory first applied to BARITT diodes.[16] The real part of the terminal impedance is given by

$$\begin{aligned} R_T = {} & \frac{1}{\omega C_D}\left(\frac{\sigma}{\sigma^2 + \omega^2\epsilon^2}\right) \\ & \times\left(\frac{\sigma(1 - \cos\theta) + \omega\epsilon\sin\theta}{\theta}\right) + R_S(f), \end{aligned} \tag{11}$$

where σ is the injection conductance (dJ/dF) of the double-barrier structure, F is the electric field across the structure, θ is the transit angle and equals $\omega D/v_d$, v_d is the average drift velocity across the depletion layer on the anode side of the barriers, $R_S(f)$ is given by Eq. (3), and $C_D = \epsilon A/D$. The frequency at which R_T vanishes defines the transit-time-limited, zero-resistance frequency. Because the double-barrier structure is assumed to be uncharged, we can write

$$\sigma = (D + W)\frac{dJ}{dV_J} = (D + W)\frac{G}{A},$$

where G is given by Eq. (9).

IV. DEVICE PARAMETER EVALUATION

The double-barrier diode that yielded the best performance has the material composition shown in Fig. 3. From this information and the measured *I-V* curve of the device, all of the desired device parameters can be evaluated. We first calculate the total series resistance of Eq. (3) for a 4-μm mesa. Separate measurements indicate that for $N_D = 2\times10^{17}$ cm^{-3} in the region below the ohmic contact, ρ_c can be no less than 10^{-6} Ω cm^2. Using this lower limit we find a contact resistance of 8 Ω. The epilayer resistance $R_{\rm epi}$ is found to be about 4 Ω for $L_e = 500$ nm and $\rho_e \cong 0.009$ Ω cm on each side of the barriers. The high-frequency spreading resistance component in Eq. (3) can be simplified to $6\times10^{-6}\sqrt{f}$ Ω if we assume $\rho_s = 0.0015$ Ω cm (for the $n^+ = 2\times10^{18}$ cm^{-3} substrate), $b = 0.02$ cm, and $h = 0.01$ cm. The sum of these components is $R_S = 14$ Ω at 200 GHz and 16 Ω at 600 GHz, respectively. However, nonuniformities in the contact quality often resulted in much larger values of ρ_c than the minimal value assumed here. Higher series resistance causes the current peak to shift to higher voltage. Devices having peak voltages shifted by about 0.25 V or more ($R_S \gtrsim 50$ Ω) did not oscillate in the WR-3 resonator.

Shown in Fig. 6 is the *I-V* curve for the present device obtained by applying Eq. (8) and the expression for the total voltage across the device $V_T = V_J + JAR_S$. We assume here that R_S equals the minimum value 14 Ω. In applying this expression, Γ_0 was obtained by demanding that the peak current be the same as that observed experimentally. The value of $\Gamma_0 = 1.65$ meV obtained by that procedure is much greater than the value of $\Gamma_0 = 0.5$ meV predicted by a separate (numerical) calculation of T^*T for the present structure in which the effective mass in the AlAs barriers was assumed to be equal to the bulk-AlAs value, $m^* = 0.15\ m_0$. It is much closer to the numerical result of $\Gamma_0 = 2.1$ meV obtained with an effective mass in the barriers equal to the bulk-GaAs value, $m^* = 0.067\ m_0$. The latter calculation also determined $E_0 = 140$ meV. The value of $\Gamma_S = 2.5$ meV was calculated from data on the mobility of quantized inversion layers in MODFETs,[17,18] assuming $\Gamma_S = \hbar/\tau$, $\tau = m^*\mu/e$, and $\mu = 7000\ \text{cm}^2\ \text{V}^{-1}\ \text{s}^{-1}$. The value for $E_F^c = -18$ meV corresponds to fully ionized but neutral $2\times 10^{17}\ \text{cm}^{-3}$ material at 295 K. Finally, $V_A = 0.065$ V was obtained by demanding that Eq. (8) yield the same peak voltage as the experimental curve. Since we are only interested in the rather narrow range of the NDC region, V_A was kept fixed in this calculation.

The determination of the two quantities, Γ_0 and V_A, allows us to calculate the capacitance, the differential conductance, and the charge distribution in the double-barrier structure. Substituting $V_A = 65$ mV, $W = 79$ nm, and $V_J = 0.85$ V in Eq. (10), we find $D + W = 75.5$ nm, so that $C \cong 19$ fF for a 4-μm-diam mesa. This parameter was found to be 21 fF in our previous estimation when the quantum well was assumed to be charged.[3] The value $\Gamma_0 = 1.65$ meV and the assumed value of Γ_S allow us to obtain the curve G vs V_J shown in Fig. 7. Note that the $G_{\max} = -26$ mS is significantly larger than the value -13 mS obtained by applying the rule $G_{\max} = -2.1\ \Delta I/\Delta V$ to the experimental I-V curve in Fig. 4. However, it is much smaller in magnitude than the ~ -1000 mS predicted by a previous theory.[12] Band bending on the anode side of the barriers reduces the latter prediction by an order of magnitude, and scattering reduces it further by about a factor of 3.

To obtain the charge distribution in the present double-barrier structure, we employ a variation of the model that was used to derive Eq. (5). Here we sum the electron stationary-state probability density $\rho_{E_L}(x) = \psi^*_{E_L}(x)\psi_{E_L}(x)$, where ψ_{E_L} is the wave function at a longitudinal energy E_L, over the occupied states on the cathode side of the structure without weighting these states by their longitudinal velocity. If we adopt the model of band bending shown in Fig. 5, this procedure leads to the following expression for the charge density:

$$n(x) = (2m^*)^{1/2}\frac{\beta}{e}\int_{eV_A}^{\infty} dE_L\, \frac{\rho_{E_L}(x)}{E_L^{1/2}} \times \ln[1 + \exp(E_F^c + eV_A - E_L)/kT]. \quad (12)$$

The probability density is obtained by first modeling the real potential energy profile as a series of 0.1-nm-wide, uniform-potential layers. Starting at the accumulation layer boundary, we evaluate $\rho_{E_L}(x)$ in each successive layer by applying the transfer-matrix method.[11] Finally, Eq. (12) is numerically integrated using the value for V_A found above and the value of V_J at the current peak. The resulting charge distribution is shown in Fig. 8 along with the assumed (linear) potential energy profile in the double-barrier structure. Notice that the charge peaks near the center of the quantum well as expected, but the maximum magnitude is only about $1\times 10^{17}\ \text{cm}^{-3}$. When this distribution is integrated over the double-barrier structure, a sheet charge density of $3.9\times 10^{10}\ \text{cm}^{-2}$ is obtained. This is so much less than the total sheet density, $\cong 1.5\times 10^{12}\ \text{cm}^{-2}$, in the depletion layer that its effect on the resonant-tunneling process is negligible. A detailed calculation verifies this assertion by showing the charge to depress the assumed potential profile by less than 1 meV across the entire structure.

V. ANALYSIS OF MAXIMUM OSCILLATION FREQUENCY

We can now determine $f_{\max}$ for the present diode structure and for a feasible variation of it. In relation to the theory

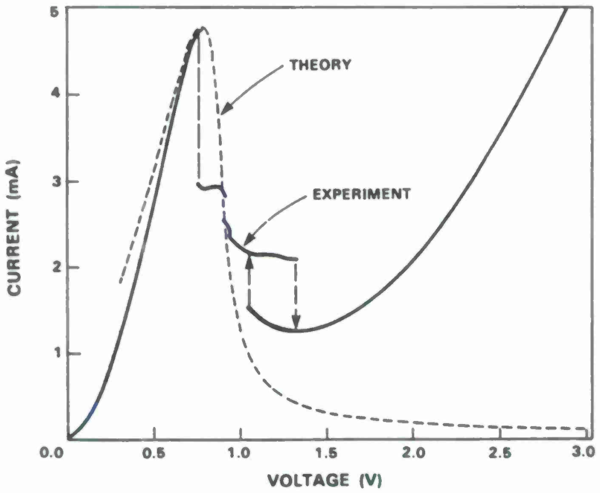

FIG. 6. Experimental (solid) and theoretical (dashed) I-V curves for present 4-μm-diam device at room temperature. The arrows denote the direction of switching that occurs in the experimental hysteresis loop.

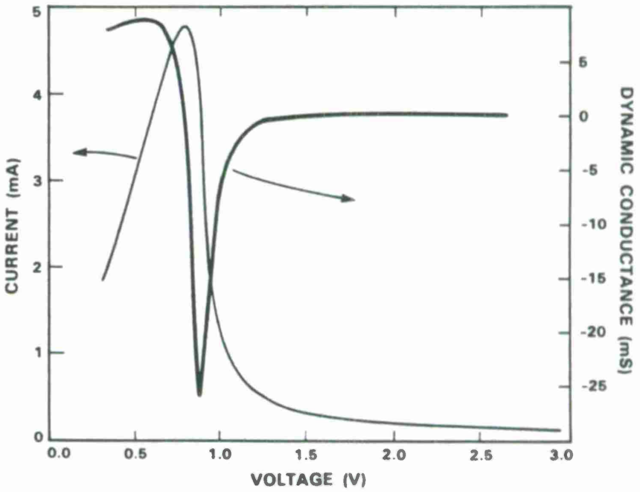

FIG. 7. Theoretical I-V and G-V curves of the present 4-μm-diam device at room temperature.

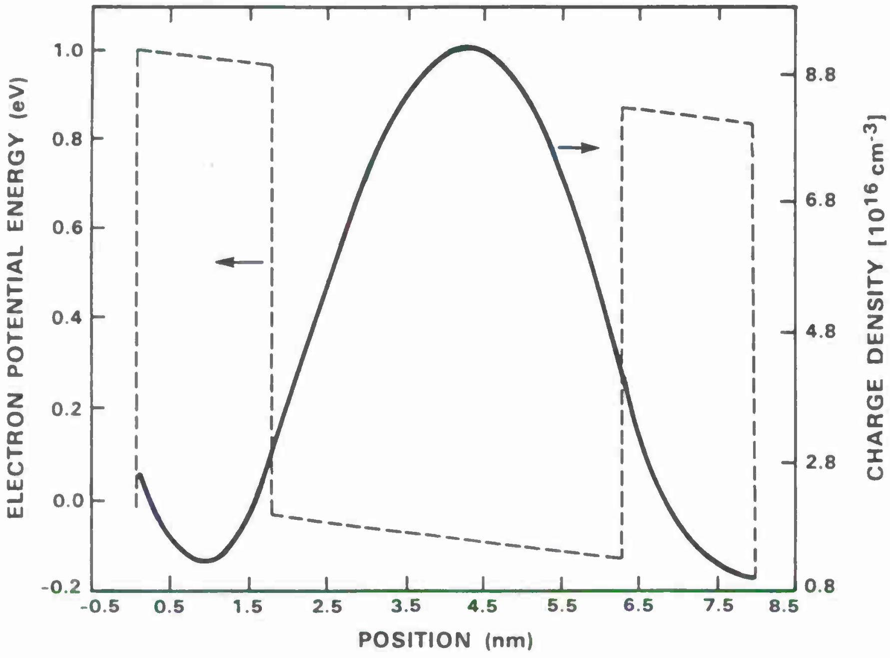

FIG. 8. Electron potential energy and charge distribution across the present double-barrier structure with 0.9-V bias applied at room temperature.

developed in Sec. III, $f_{\max}$ is the peak value of the zero-resistance frequency f_R over the possible range of differential conductance values, $G < G_{\max}$. It is instructive to calculate $f_{\max}$ for each of the three theoretical models considered: the lumped-circuit model [Eq. (1)], the lumped-circuit model modified by the frequency-dependent skin effect [Eq. (4)], and the combined transit-time, skin-effect model [Eq. (11)]. We also suspect that $f_{\max}$ will depend strongly on the diode geometry, so that three different mesa diameters will be anayzed.

Shown in Figs. 9(a), 9(b), and 9(c) are curves of f_R for mesa diameters of 4, 2, and 1 μm, respectively. The range of possible operating conditions for each diode size lies left of the dashed line $G = G_{\max}$. The resulting values of $f_{\max}$ are denoted $(f_{\max})_L$, $(f_{\max})_S$, and $(f_{\max})_T$ for the lumped-circuit, skin-effect, and transit-time models, respectively, and are summarized in Table I. Note that curves of $(f_{\max})_T$ are given for two different values of drift velocity, $v_d = 2\times 10^7$ cm s^{-1} and 4×10^7 cm s^{-1}. Although we do not precisely know the average drift velocity across the 75-nm depletion layer, the two assumed values are thought to be representative of the possible range. They are both greater than the saturation velocity in GaAs ($\sim 1\times 10^7$ cm s^{-1}) because the double-barrier structure injects the elecrons with a relatively large kinetic energy ($\sim$200 meV), which results in a very large initial group velocity.

Several aspects of these theoretical results deserve attention. First, it is gratifying that the range of $(f_{\max})_T$, 214 to 244 GHz, for the 4-μm-diam mesa lies above our highest experimental result. However, notice that the transit-time delay lowers $f_{\max}$ significantly compared with the lumped-circuit and skin-effect models. In addition, $f_{\max}$ varies noticeably with the mesa diameter. For example, when the diameter is reduced from 4 to 2 μm, all $f_{\max}$ values increase somewhat because the spreading resistance is a much smaller fraction of R_S in the 2-μm-diam device. This reflects the fact that the spreading resistance varies with area much slower than inversely. However, there is very little difference in $f_{\max}$ between the 2- and 1-μm-diam devices because the relative magnitude of the spreading resistance is becoming negligible at these diameters. Finally, it is clear that a change in the material parameters of this device that increased $G_{\max}$ but kept R_S and C fixed would do little or nothing to enhance $f_{\max}$. This is because the $G_{\max}$ calculated for our present device is very close to the value of G which produces the highest $f_{\max}$. A more promising material change would be one that decreases R_S.

A simple variation of the present device structure that should reduce R_S significantly is shown diagrammatically in Fig. 10. The doping concentration on the cathode side is rapidly increased to the largest practical value ($\lesssim 2\times 10^{18}$ cm^{-3}) after a few accumulation-layer lengths on the cathode side, and is increased to the same level after about 100 nm on the anode side. This will reduce the contact specific resistance to about $1\times 10^{-7}\ \Omega$ cm^2, and should cut R_{epi} in half, thereby lowering R_S to about 5 Ω at 200 GHz and 7 Ω at 600 GHz. We assume that the other parameters are identical to those of the present device.

Theoretical curves of the zero-resistance frequency for the proposed device are given in Fig. 11. First notice the large increase in all $f_{\max}$ values compared with present devices of the same diameter. For example, the 4-μm-diam device now gives $(f_{\max})_L = 593$ GHz and a transit-time-limited range $(f_{\max})_T = 369$–426 GHz. Because the relative contribution of the spreading resistance is now much larger, there is a great increase in all $f_{\max}$ values as the mesa diameter is decreased. For example, the upper limit of the $(f_{\max})_T$ range increases to 568 and 641 GHz in the 2- and 1-μm mesas, respectively. Also notice that the transit-time-limited curves all peak at a value of G greater than $G_{\max}$, in contrast to the present device. This means that for these low values of R_S, significantly faster devices can be obtained by increasing $G_{\max}$.

In principle $G_{\max}$ could be increased in one of three

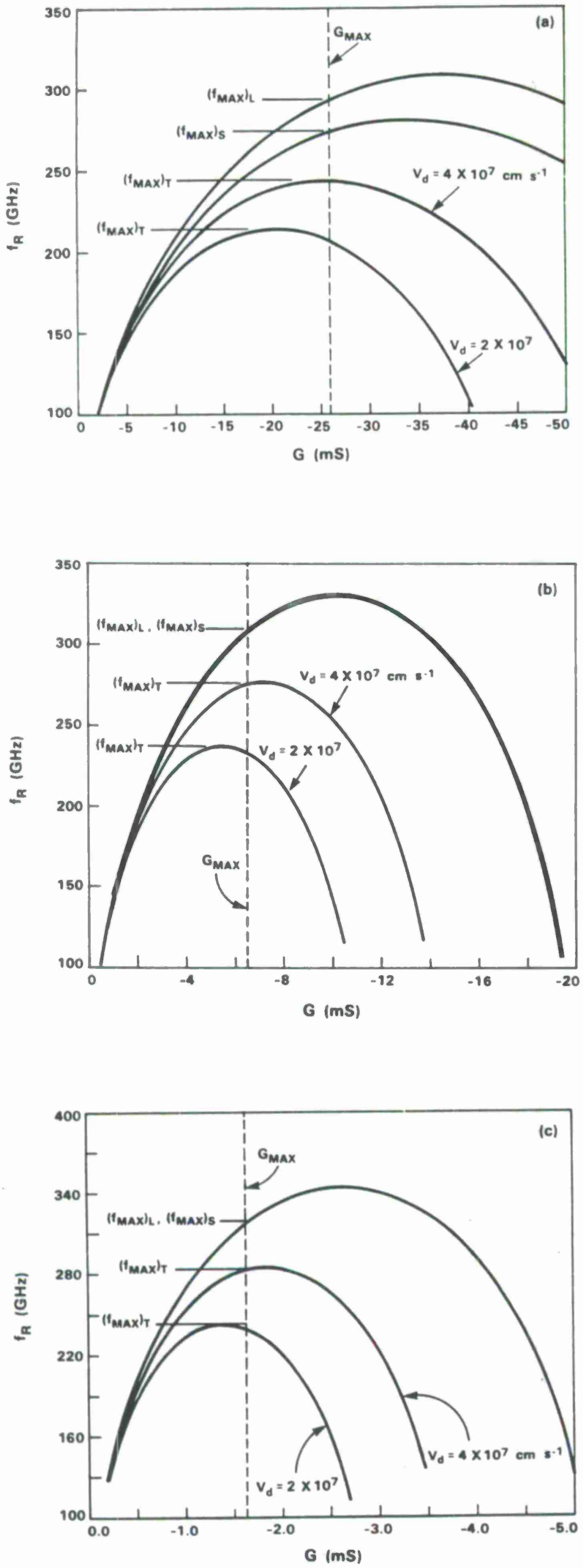

FIG. 9. Zero-resistance frequency curves for (a) 4-μm-, (b) 2-μm-, and (c) 1-μm-diam mesas of the present sample. The three quantities $(f_{\max})_L$, $(f_{\max})_S$, and $(f_{\max})_T$ are the maximum oscillation frequencies for the lumped-circuit model, the lumped-circuit model with skin effect, and the transit-time model with skin effect, respectively. The quantity $G_{\max}$ is the maximum differential conductance.

TABLE I. Values of $f_{\max}$ for the three models under consideration.

Mesa diameter (μm)	$(f_{\max})_L$ (GHz)	$(f_{\max})_S$ (GHz)	$(f_{\max})_T$ (GHz) ($v_d = 2\text{–}4 \times 10^7\ \text{cm s}^{-1}$)
		Present device:	
4	293	274	214–244
2	310	310	237–275
1	317	317	244–283
		Proposed device:	
4	593	467	369–426
2	676	634	475–568
1	758	730	535–641

ways: (1) by material changes that increase the resonant-tunneling current density by some fraction while enhancing the leakage current density by a lesser fraction; (2) material changes that reduce only the leakage current density; or (3) operational changes (such as a reduction in temperature) that reduce the leakage current density. We will consider only the first method because it is the simplest to compute in the present theoretical formalism, and because it has the practical appeal of increasing the oscillation power density. The most plausible material change is to increase the doping concentration, and hence the Fermi level, on the cathode side of the heterostructure. For example, suppose that $N_D = 1 \times 10^{18}\ \text{cm}^{-3}$ throughout the cathode side of the barriers. In this case $E_F^c = +39$ meV, and if we assume that the V_A remains the same as for the lower doping, Eqs. (8) and (9) predict the *I-V* and *G-V* curves of Fig. 12. Notice that J_P has increased to four times its value in Fig. 7, and $G_{\max} = -125$ mS. All of the peaks in the f_R curves of Fig. 11 could then be achieved. Thus, the upper limit of the $(f_{\max})_T$ range would be 453, 642, and 750 GHz for the 4-, 2-, and 1-μm devices, respectively.

VI. DISCUSSION

This analysis is not intended to provide a complete optimization for the double-barrier diode. Instead, we have pointed out some simple changes in the diode material structure that should increase the maximum oscillation frequency by at least a factor of 2. A complete optimization would require consideration of other material parameters, such as the barrier and quantum-well thickness, and the doping concentration on the anode side of the structure. Very little is known about the effect of these parameters on the diode behavior, especially their influence on the excess current [i.e., the current beyond that predicted by Eq. (8)]. As seen in Fig. 6, the excess current is the major component of the total current at and above the valley. It is possibly associated with scattering from impurities in the barriers, a mechanism for which transverse crystal momentum is not conserved in the tunneling process. The component should also be very fast, so that it would affect the device behavior by reducing the peak-to-valley ratio and by reducing $G_{\max}$.

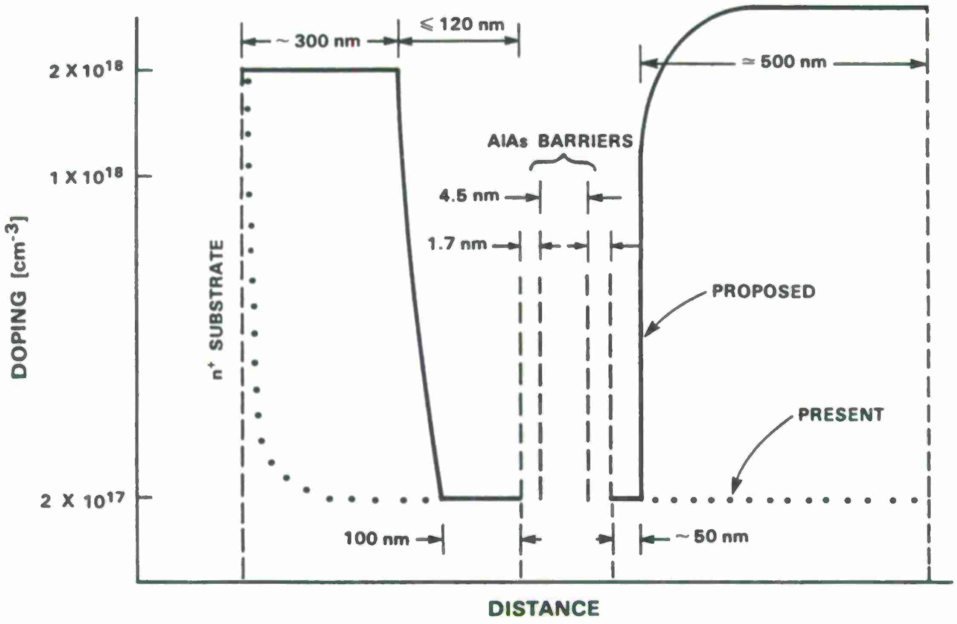

FIG. 10. Doping concentration profile for present (dotted) and proposed (solid) double-barrier device.

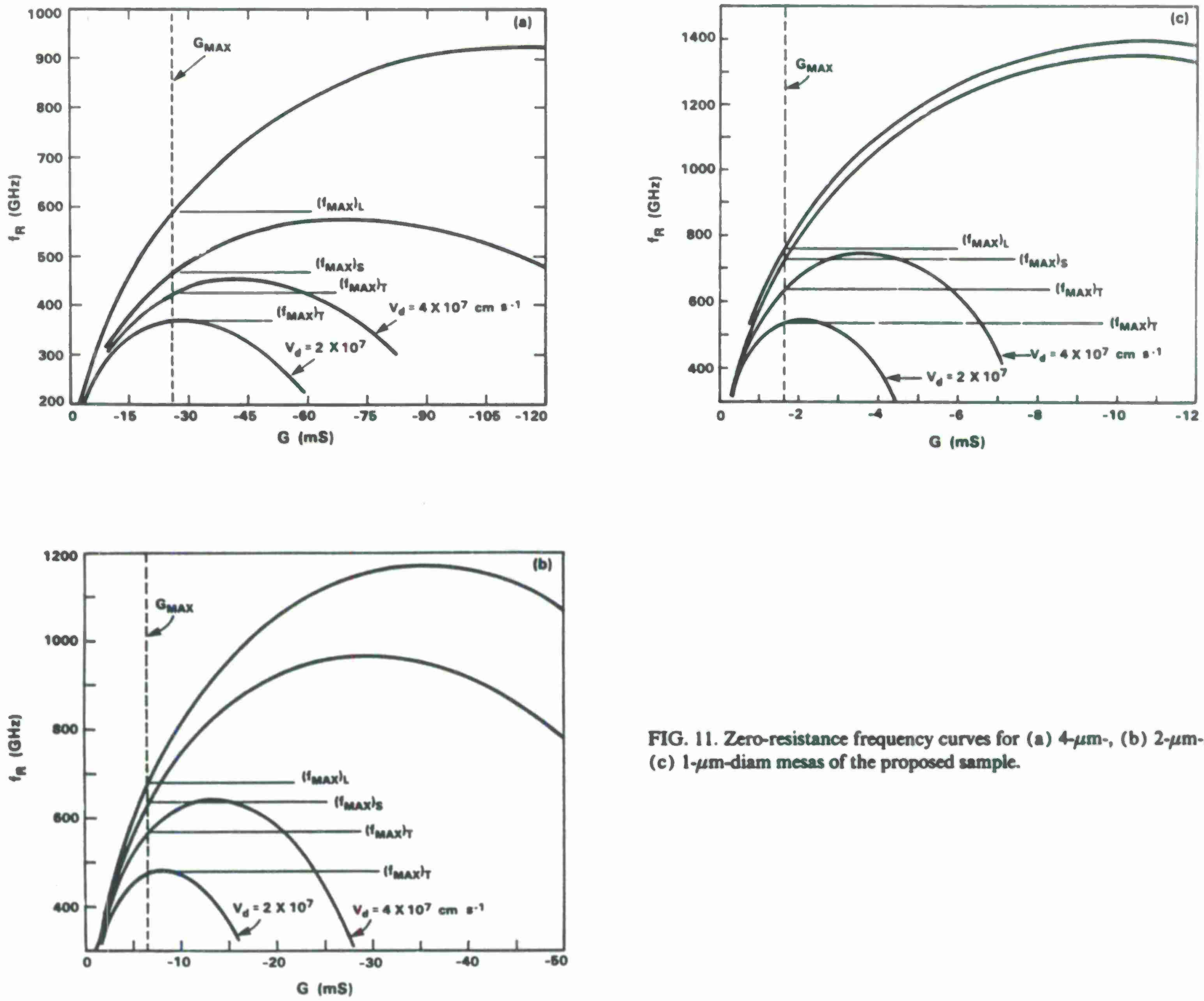

FIG. 11. Zero-resistance frequency curves for (a) 4-μm-, (b) 2-μm-, and (c) 1-μm-diam mesas of the proposed sample.

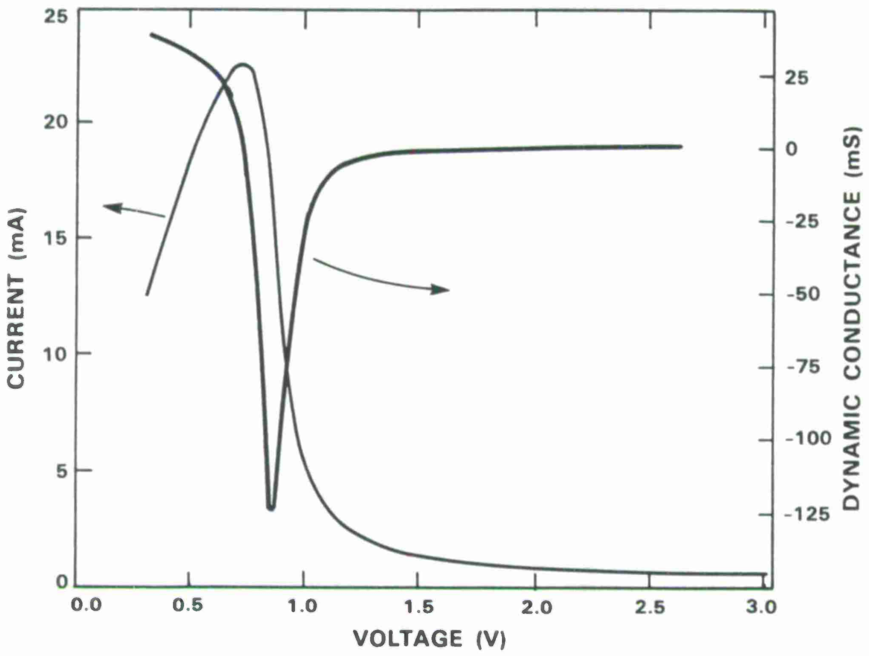

FIG. 12. Theoretical I-V and G-V curves of proposed sample at room temperature. This sample would have a uniform doping concentration of $N_D = 2\times10^{17}\,\mathrm{cm}^{-3}$ and $1\times10^{18}\,\mathrm{cm}^{-3}$ on the anode and cathode sides of the double-barrier structure.

Another factor that we have ignored is the finite lifetime of electrons in the quasibound states of the quantum well. According to the uncertainty principle, each electron wavepacket builds up and decays in the well in a time $\tau \gg \hbar/\Gamma_0$, where Γ_0 is the half width of the T^*T curve. It has often been assumed that this corresponds to a zero-resistance frequency, $f_R = (2\pi\tau)^{-1}$, which would be near 400 GHz for the present device. While the finite lifetime will definitely slow down the tunneling process, its effect of $f_{\max}$ is not clear. Intuitively we expect that the lifetime in the well should cause the ac conduction current to lag behind the ac voltage. This is clearly an inductive effect. A double-barrier diode equivalent circuit containing an intrinsic inductance has been proposed by Gering *et al.*[19]

All of the oscillations measured to date above 30 GHz have had output power less than 1 mW, and it is unlikely that this level will ever be greatly exceeded in a single diode. To do so would require a much larger device than those considered here. Such a device would be practically impossible to stabilize at low frequencies because its $G_{\max}$ would be at least -100 mS. A more promising way to increase the power would be to use the double-barrier structure as an injector for a transit-time oscillator.[20] In this case both the material parameters of the structure and the doping level on the anode side are tailored to achieve a negative terminal resistance according to Eq. (11). This can be achieved with the device biased in the positive resistance region if the depletion length yields a transit angle θ between π and 2π in the frequency range of interest. A significant increase in the device area will then enhance the output power without causing low-frequency instabilities. Another approach to increasing the power is to combine the output of several diodes that operate in the NDC region but are independently biased and stabilized. For example, one could design a monolithic circuit in which each of the diodes had its own resonator, bias network, and a planar antenna to couple out the radiation. The analysis of such a circuit has been given recently by Mink.[21]

VII. SUMMARY

We have demonstrated the first fundamental oscillations in a resonant tunneling diode above 100 GHz, with our highest frequency occurring at 201 GHz. This has led to a new estimate of 293 GHz for the upper limit of $f_{\max}$ in the present 4-μm-diam device. It should be compared with the value $f_{\max} = 187$ GHz obtained previously from empirical estimates of $G_{\max}$. The negative conductance is now obtained with a phenomenological theory containing two fitting parameters. This upper limit is reduced by skin effects and transit-time delay to 244 GHz, if we assume the drift velocity equals $4\times10^7\,\mathrm{cm\,s}^{-1}$ across the depletion layer. We propose that a simple change in the doping profile of the present device which reduces the series resistance should increase the transit-time-limited $f_{\max}$ to about 430, 570, and 640 GHz for a 4-, 2-, and 1-μm-diam device, respectively. If the current density could also be increased without significantly diminishing the peak-to-valley ratio, these $f_{\max}$ values would increase further by about 10%.

ACKNOWLEDGMENTS

The authors wish to thank A. L. McWhorter, R. A. Murphy, and P. E. Tannenwald for carefully editing this manuscript. We also acknowledge C. D. Parker for packaging devices and assisting in the measurements, N. Usiak for providing whiskers and chip bonds, M. A. Hollis for valuable conversations, and C. L. Chen, L. J. Mahoney, and G. D. Johnson for performing the fabrication procedures. This work was carried out with the support of the U.S. Army Research Office.

[1] T. C. L. G. Sollner, P. E. Tannenwald, D. D. Peck, and W. D. Goodhue, Appl. Phys. Lett. **45**, 1319 (1984).

[2] T. J. Shewchuk, P. C. Chapin, P. D. Coleman, W. Kopp, R. Fischer, and H. Morkoç, Appl. Phys. Lett. **46**, 508 (1985).

[3] E. R. Brown, T. C. L. G. Sollner, W. D. Goodhue, and C. D. Parker, Appl. Phys. Lett. **50**, 83 (1987).

[4] W. D. Goodhue, T. C. L. G. Sollner, H. Q. Le, E. R. Brown, and B. A. Vojak, Appl. Phys. Lett. **49**, 1086 (1986).

[5] T. C. L. G. Sollner, E. R. Brown, W. D. Goodhue, and H. Q. Le, Appl. Phys. Lett. **50**, 332 (1987).

[6] N. Iwata, Y. Matsumoto, and T. Baba, Jpn. J. Appl. Phys. **24**, L17 (1985).

[7] W. D. Goodhue, G. D. Johnson, and T. H. Windhorn, in *Proceedings of the 13th International Conference on GaAs and Related Compounds*, edited by W. T. Lindley (Inst. Phys. Conf. Ser. **83**, 349, 1986).

[8] H. K. Henisch, *Rectifying Semiconductor Contacts* (Oxford University Press, London, 1957).

[9] B. C. DeLoach, IEEE Trans. Microwave Theory Tech. **MTT-15**, 457 (1972).

[10] C. B. Duke, *Tunneling in Solids* (Academic, New York, 1969), Secs. 5 and 7 (a).

[11] R. Tsu and L. Esaki, Appl. Phys. Lett. **22**, 562 (1973).

[12] D. D. Coon and H. C. Liu, Appl. Phys. Lett. **49**, 94 (1986).

[13] D. D. Coon and H. C. Liu, Appl. Phys. Lett. **47**, 172 (1985).

[14] A. D. Stone and P. A. Lee, Phys. Rev. Lett. **54**, 1196 (1985).

[15] T. Weil and B. Vinter, Appl. Phys. Lett. **50**, 1281 (1987).

[16] S. M. Sze, *Physics of Semiconductor Devices* (Wiley, New York, 1981), Sec. 10.7.2.

[17] C. W. Tu, R. H. Hendel, and R. Dingle, *Gallium Arsenide Technology*, edited by D. K. Ferry (Sams, Indianapolis, 1985), p. 107.

[18] F. Capasso, K. Mohammed, and A. Y. Cho, IEEE J. Quantum Electron. **QE-22**, 1853 (1986).

[19] J. M. Gering, D. A. Crim, D. G. Morgan, P. D. Coleman, W. Kopp, and H. Morkoc, J. Appl. Phys. **61**, 271 (1987).

[20] V. P. Kesan, D. P. Neikirk, B. G. Streetman, and P. A. Blakey, IEEE Electron. Device Lett. **EDL-8**, 129 (1987).

[21] J. W. Mink, IEEE Trans. Microwave Theory Tech. **MTT-34**, 273 (1986).

Harmonic multiplication using resonant tunneling

T. C. L. G. Sollner, E. R. Brown, W. D. Goodhue, and C. A. Correa
Lincoln Laboratory, Massachusetts Institute of Technology, Lexington, Massachusetts 02173

(Received 4 March 1988; accepted for publication 1 July 1988)

We propose and demonstrate an odd-harmonic resistive multiplier that exploits the unique current-voltage (*I-V*) relation of resonant-tunneling diodes. It is shown that efficient odd-harmonic conversion is possible and that even harmonics do not appear because of the antisymmetry of the *I-V* curve. In addition, with the proper choice of resonant-tunneling structure and pump amplitude, most of the harmonic output power can be confined to a single, odd-harmonic frequency. Fifth-harmonic multiplication has been demonstrated with output at 21.75 GHz and a power conversion efficiency of 0.5% in a coaxial circuit. Circuit simulation using an improved *I-V* curve yields a fifth-harmonic efficiency of 2.7%, suggesting that useful harmonic output in the millimeter and submillimeter spectrum should be achievable.

Harmonic multipliers are often used for the generation of electromagnetic waves at frequencies above those conveniently available from fundamental oscillators. For example, radio astronomy receivers at frequencies above 50 GHz often use power from a multiplier as the local oscillator,[1] and multipliers are a primary source of power for molecular spectroscopy in the submillimeter spectrum.[2]

Harmonic multipliers have traditionally used either the voltage-dependent resistance (a varistor) or capacitance (a varactor) associated with either metal-semiconductor (Schottky diodes) or *p-n* junctions. Capacitive nonlinearities have been favored because of the higher available conversion efficiency between the power delivered by the pump and that available at the desired harmonic. It was shown by Page[3] that a resistive nonlinearity containing no negative differential resistances can produce a conversion efficiency of at most $1/n^2$, where n is the harmonic number. On the other hand, varactors are limited by the Manley–Rowe relations,[4] which in this case allow a maximum conversion efficiency of unity.

In this communication, we propose and demonstrate the use of resonant-tunneling diodes as varistors for harmonic generation. (Some of the basic ideas and preliminary results were first published by Sollner, Brown, and Goodhue[5] in 1987.) One advantage of these devices over Schottky diodes is the presence of negative differential resistance regions in the current-voltage (*I-V*) curve, so it is possible, as discussed by Andreyev,[6] to surpass the limits found by Page for resistive mixers. Another advantage is that, under the proper conditions, it is possible to confine most of the harmonic output power to a single harmonic frequency. For Schottky-diode multipliers, larger voltages are always generated at lower harmonics, which must be properly reactively terminated. Avoiding these additional "idler" circuits will greatly simplify circuit design and should therefore increase efficiency, especially in the millimeter and submillimeter wavelength range where it is difficult to avoid significant resistive loss. Also, no dc bias is required, further simplifying the circuit. For resonant-tunneling diodes available today, output frequencies of several hundred gigahertz are expected to be feasible, and perhaps even higher frequencies will be available with optimized diodes. This part of the frequency spectrum now suffers from a lack of available solid-state sources, so resonant-tunneling multipliers could fill this need, at least for low-power sources.

Resonant tunneling occurs when two or more semitransparent barriers are placed closely enough together that charge carriers interact coherently with them. The resonant states formed between the barriers greatly increase the tunneling probability of carriers with energy equal to that of the states, resulting in peaks and valleys in the current as the voltage across the structure is increased. Typically, the barriers are made from an epitaxially grown material of larger band gap, such as AlAs grown on GaAs. A typical *I-V* curve for a double-barrier resonant-tunneling diode is shown in Fig. 1. More details on the fabrication of resonant-tunneling diodes have been published by Goodhue *et al.*[7]

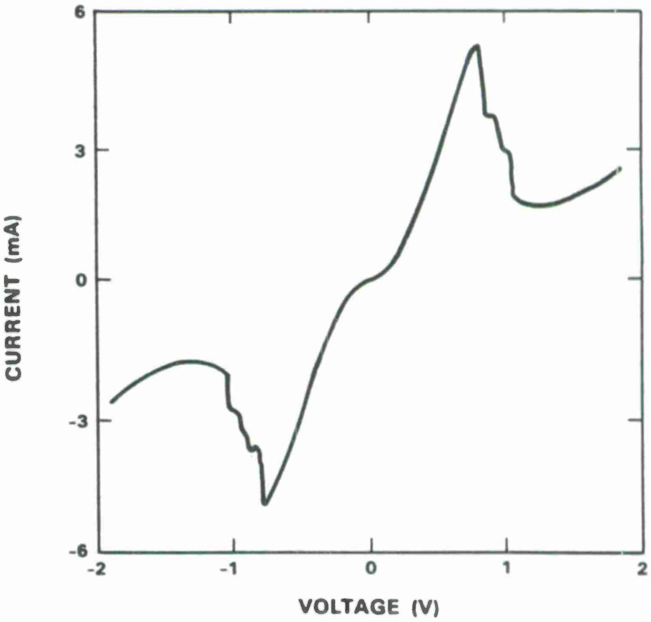

FIG. 1. Current-voltage (*I-V*) curve of the resonant-tunneling diode that was used as a resistive harmonic multiplier. Oscillations were occurring in the negative differential resistance regions, causing the departures from a smooth curve. These oscillations, at about 10 GHz, apparently did not begin when the device was pumped at frequencies above 1 GHz.

0021-8979/88/204248-03$02.40

The presence of a peak and valley in the *I-V* curve, combined with the overall antisymmetry of the *I-V* curve about the origin [i.e., $I(V) = -I(-V)$], offer the potential for efficient odd-harmonic generation with an unbiased resonant-tunneling diode. If the diode is pumped with an ac signal, so that the peak amplitude of the voltage across the diode occurs above the resonant current peak, at least three local maxima occur in the diode current waveform over one cycle, corresponding to third or higher odd-harmonic generation.

It is interesting to note that the velocity-field relation of *n*-type GaAs is similar to the current-voltage relation shown in Fig. 1. This velocity-field relation arises from the scattering of hot electrons between the Γ and *L* valleys, and a number of workers have used this effect for frequency multiplication.[8,9] The main disadvantage is that electrons require time of the order of a picosecond to return to the Γ valley, limiting the useful frequencies to below 100 GHz. The frequency limits for resonant tunneling will be discussed below.

A resonant-tunneling diode with the *I-V* curve shown in Fig. 1 was mounted in a coaxial, whisker-contacted package and placed in the circuit shown in Fig. 2. All components were connected together with 50-Ω coaxial line, and the circuit was relatively free of resonances to 22 GHz. The oscillator power at 4.25 GHz was adjusted to give optimum conversion efficiency at the fifth harmonic, resulting in the spectrum shown in Fig. 3. The power available at the fundamental (4.25 GHz) was measured by replacing the resonant-tunneling diode with a short. The best fifth-harmonic conversion efficiency was 0.5%. As expected, the power converted to even harmonics is more than 40 dB below the odd-harmonic output.

To estimate the conversion efficiency expected from a resonant-tunneling diode, the *I-V* curve of Fig. 1 was fitted to a piecewise continuous curve, and the circuit of Fig. 2 was simulated using lumped circuit elements. We have assumed that the only power source occurs at the fundamental frequency of the oscillator; however, the solution to the full nonlinear problem requires sources that account self-consistently for the harmonics generated by the nonlinearities of the diode.[10] The neglect of these terms greatly simplifies the calculation, but causes some quantitative discrepancy. The calculated fifth-harmonic conversion efficiency is 0.3% rather than the observed value of 0.5%, and the calculated third-harmonic output power is below that observed by a similar amount. It is possible that the differences may arise from our neglect of the harmonic sources mentioned above, or perhaps from ignoring the voltage dependence of the capacitance that occurs in the resonant-tunneling diode. Still, the agreement with the measured spectrum of Fig. 3 is sufficient to give us confidence that the numerical model is a good approximation to the experimental measurement.

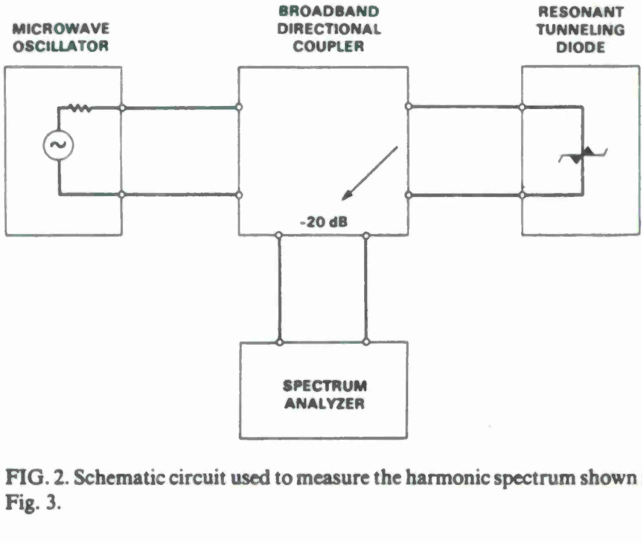

FIG. 2. Schematic circuit used to measure the harmonic spectrum shown in Fig. 3.

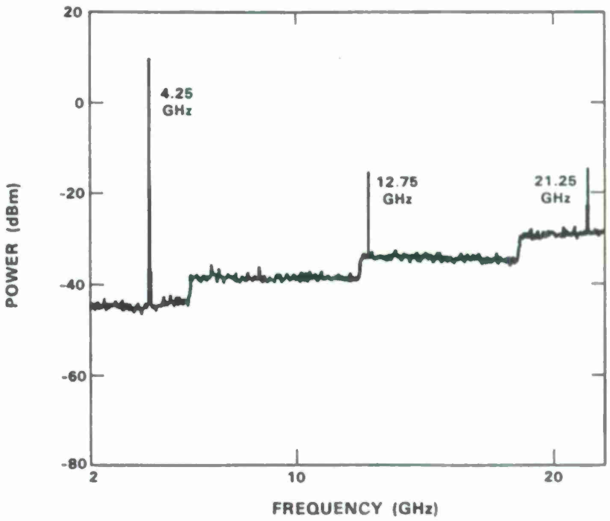

FIG. 3. Power spectrum generated by a resonant-tunneling diode in the circuit of Fig. 2. The amplitude of the pump at 4.25 GHz has been adjusted to optimize the fifth-harmonic output power at 21.25 GHz. The absence of even harmonics is an indication of the high degree of antisymmetry of the *I-V* curve.

The model described above can be used to predict the performance of a multiplier when the *I-V* curve of the resonant-tunneling device has been arranged to increase harmonic generation. The characteristics that are desirable are a large peak-to-valley ratio and a shape that provides more equal spacing in time between the maxima in the current waveform. The simulated *I-V* curve shown in Fig. 4 has not been optimized for these characteristics, but it is a considerable improvement over the curve of Fig. 1. Figure 5 shows the power spectrum at the terminals of the diode when the voltage amplitude and source resistance have been optimized for fifth-harmonic conversion. This simulation yields a fifth-harmonic conversion efficiency of 2.7%, and additional optimization is still possible. The calculated efficiency is near the limit of $1/n^2$ derived by Page[3] for positive-conductance nonlinearities, and perhaps further improvements could surpass it. For example, the filters could be arranged so that the fundamental and harmonics could be terminated with different impedances.

The efficiency of multipliers using *I-V* curves similar to that of Fig. 1 drops quickly for harmonics above the fifth because there is only one peak and valley in each quadrant of the curve; however, it is possible to have several peaks in a resonant-tunneling *I-V* curve. Two peaks would make possible the efficient generation of up to the ninth harmonic, three peaks allow the thirteenth harmonic, and so on. (Recently,

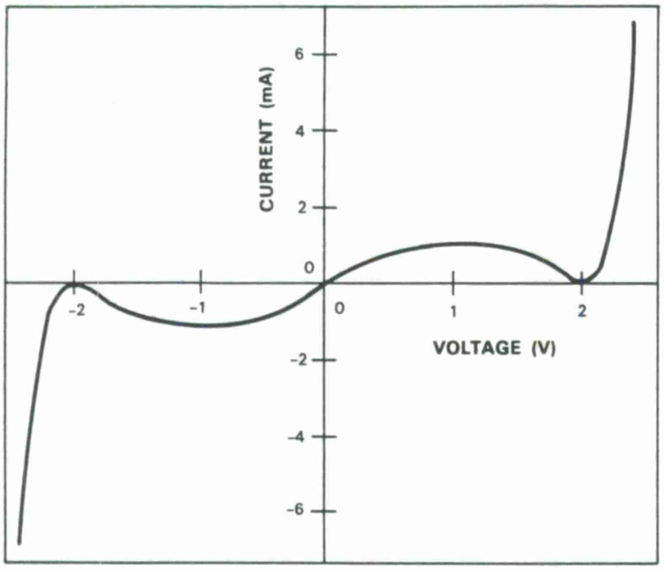

FIG. 4. Hypothetical *I-V* curve that gives better harmonic generation efficiency than the experimental curve of Fig. 1.

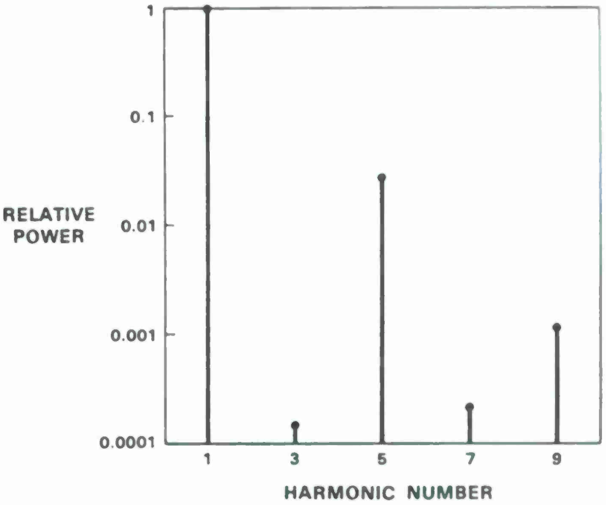

FIG. 5. Power spectrum calculated using the *I-V* curve of Fig. 4. The conversion efficiency to the fifth harmonic is nearly an order of magnitude larger than that calculated using the experimental *I-V* curve of Fig. 1.

Sen *et al.*[11] have suggested that two resonant-tunneling diodes in series can produce a large fifth-harmonic output in a somewhat different application.) It should also be feasible to adjust the pump amplitude to produce most of the harmonic power in a single harmonic if the current in the higher-voltage valleys can be kept sufficiently small. Thus, a single harmonic multiplier could convert power below 100 GHz to the terahertz range.

The upper frequency limit for a given resonant-tunneling diode oscillator has been studied in some detail,[12] but the multiplier has not been carefully analyzed to date. An estimate can be reached through reasoning leading to the maximum oscillation frequency $f_{\max}$. This is the frequency above which there is no negative resistance observable from the device terminals, so the peaks in the current waveform, so essential to the concepts presented here, would not be present. This frequency is given by

$$f_{\max} = (1/2\pi C)\,[\,(-G_{\max}/R_s) - G_{\max}^2\,]^{1/2}.$$

Here C is the device capacitance parallel with the maximum (negative) conductance $G_{\max}$, and R_s is the resistance in series with this parallel combination. Currently available resonant-tunneling diodes have $f_{\max}$ values approaching 300 GHz.[13] One of these diodes has recently been used as a tripler by Batelaan and Frerking[14] to produce 250 μW at 191 GHz with 0.61% efficiency.

In summary, a promising new approach for resistive harmonic multipliers has been demonstrated with resonant-tunneling diodes. Several advantages for high-harmonic multipliers are available, and it is expected that these ideas can be extended to obtain usable power in the terahertz region.

It is a pleasure to acknowledge technical assistance from G. D. Johnson, C. L. Chen, K. M. Molvar, D. J. Landers, N. Usiak, R. F. Murphy, G. L. Durant, and B. J. Felton. Helpful discussions were contributed by J. W. Bales, R. H. Mathews, K. A. McIntosh, C. D. Parker, and P. E. Tannenwald. This work was sponsored by the U.S. Army Research Office, the U.S. Air Force, and NASA.

[1] E. R. Brown and P. E. Tannenwald, in *Far-Infrared Science and Technology*, Vol. 666 (SPIE, Bellingham, WA, 1986), p. 38.

[2] G. W. Chantry, Ed., *Modern Aspects of Microwave Spectroscopy* (Academic, London, 1979).

[3] C. H. Page, Proc. IRE **46**, 1738 (1958).

[4] J. M. Manley and H. E. Rowe, Proc. IRE **44**, 404 (1956).

[5] T. C. L. G. Sollner, E. R. Brown, and W. D. Goodhue, in *Picosecond Electronics and Optoelectronics II*, Vol. 24 in *Springer Series in Electronics and Photonics* (Springer, Berlin, 1987), p. 102.

[6] V. S. Andreyev, Radio Eng. Electron. Phys. **20**, 136 (1975).

[7] W. D. Goodhue, T. C. L. G. Sollner, H. Q. Le, E. R. Brown, and B. A. Vojak, Appl. Phys. Lett. **49**, 1086 (1986).

[8] S. Kaneda and H. Horima, Electron. Lett. **8**, 141 (1972).

[9] V. S. Andreyev, V. V. Kukushkin, V. I. Popov, N. Ye. Skvortsova, and B. B. Elenkrig, Radio Eng. Electron. Phys. **19**, 79 (1974).

[10] A. R. Kerr, IEEE Trans. Microwave Theory Tech. **MTT-23**, 828 (1975).

[11] S. Sen, F. Capasso, A. Y. Cho, and D. Sivco, IEEE Trans. Electron Devices **ED-34**, 2185 (1987).

[12] T. C. L. G. Sollner, E. R. Brown, W. D. Goodhue, and H. Q. Le, Appl. Phys. Lett. **50**, 332 (1987).

[13] E. R. Brown, W. D. Goodhue, and T. C. L. G. Sollner, J. Appl. Phys. **64**, 1519 (1988).

[14] P. D. Batelaan and M. A. Frerking, in *Conference Digest, Twelfth International Conference Infrared and Millimeter Waves*, edited by R. J. Temkin (IEEE, New York, 1987), p. 14.

APPENDIX E

Observation of millimeter-wave oscillations from resonant tunneling diodes and some theoretical considerations of ultimate frequency limits

T. C. L. G. Sollner, E. R. Brown, W. D. Goodhue, and H. Q. Le
Lincoln Laboratory, Massachusetts Institute of Technology, Lexington, Massachusetts 02173

(Received 30 October 1986; accepted for publication 8 December 1986)

Recent observations of oscillation frequencies up to 56 GHz in resonant tunneling structures are discussed in relation to calculations by several authors of the ultimate frequency limits of these devices. We find that calculations relying on the Wentzel–Kramers–Brillouin (WKB) approximation give limits well below the observed oscillation frequencies. Two other techniques for calculating the upper frequency limit were found to give more reasonable results. In one method we use the solution of the time-dependent Schrödinger equation obtained by Kundrotas and Dargys [Phys. Status Solidi B **134**, 267 (1986)], while in the other we use the energy width of the transmission function for electrons through the double-barrier structure. This last technique is believed to be the most accurate since it is based on general results for the lifetime of any resonant state. It gives frequency limits on the order of 1 THz for two recently fabricated structures. It appears that the primary limitation of the oscillation frequency for double-barrier resonant tunneling diodes will be imposed by intrinsic device circuit parameters and by the transit time of the depletion layer rather than by time delays encountered in the double-barrier region.

There has been considerable debate on the subject of the speed of devices based on resonant tunneling. By comparing high-frequency current response measurements with the observed dc characteristics, we have previously established[1] that the response time is as short as 100 fs. Luryi[2] subsequently pointed out that the oscillation frequency of a double-barrier diode (DBD) employing resonant tunneling should be limited by the well charging and discharging time. He calculated this time to be 40 ps for the structure measured in Ref. 1, corresponding to a frequency limit of approximately $f = 1/(2\pi\tau) = 4$ GHz. We have recently observed oscillations with τ as short as 2.8 ps (corresponding to 56 GHz). This frequency is more than an order of magnitude greater than predicted by Luryi's calculation. We will present evidence that this discrepancy lies in the Wentzel–Kramers–Brillouin (WKB) approximation used by Luryi.

The complete problem of electron kinetics through a DBD is complex, involving self-consistent solution to the Poisson equation and the time-dependent Schrödinger equation, including elastic and inelastic scattering. Although several groups are currently attempting solutions, no results are yet available. Since guidelines are needed to help direct experimental programs, we will here attempt to set a bound on the maximum frequency of response by calculating parts of the problem separately and finding a characteristic time for each part.

The structure of a DBD and the resulting current-voltage (*I-V*) curve are shown in Fig. 1. Oscillations are obtained by biasing the device into the negative differential resistance region of the *I-V* curve while it is embedded in a suitable high-frequency circuit. Figure 2 shows a sketch of the waveguide circuit used and its equivalent circuit with the DBD. The details of this circuit and the material parameters of the DBD have been reported elsewhere.[3]

Table I summarizes the material and electrical parameters for three waveguide oscillators. The capacitance is calculated including the size of the depletion region when the device is biased in the negative differential resistance region. The series resistance is also calculated, but it has been measured in one sample and found to agree with the calculation. The actual oscillation frequency $f_{\rm osc}$ is determined primarily by the waveguide circuit. The maximum oscillation frequency consistent with the equivalent circuit shown in Fig. 2 occurs when the conductance in parallel with the DBD from the external circuit is made arbitrarily small. This maximum frequency determined by the intrinsic circuit elements of the DBD is

$$f_{\rm circ} = (1/2\pi C)(-G_{\max}/R_s - G^2_{\max})^{1/2},$$

where $G_{\max}$ is the maximum negative conductance.

The transit time across the depletion region is closely related to the capacitance in the equivalent circuit. A wider depletion region reduces the capacitance of the device, but also introduces a phase shift in the current relative to the applied voltage just as would storage in the well. While this phase shift could be used to achieve a negative conductance as in a barrier injection and transit time diode,[4] we will assume here that the phase shift must be kept small to utilize the intrinsic negative conductance of the DBD. This time delay $\tau_{\rm depl}$ yields a frequency limit that we arbitrarily define as $f_{\rm depl} = (1/2\pi\tau_{\rm depl})$. This limit is calculated in Table I assuming the saturated carrier velocity of 10^7 cm/s. Since the scattering mean free path is comparable to the depletion region thickness, the actual velocity of carriers in the depletion region will probably be higher than this value, so this estimate of $f_{\rm depl}$ is conservative.

Another effect that could limit the maximum oscillation frequency is charge storage delay in the quantum well. In other words, if each carrier must spend a certain period of time in a quantum state in the well, then this state lifetime introduces a phase difference between the current and voltage and would limit the intrinsic response of the DBD. At first glance this state lifetime would appear to be rather long. Bohm[5] has solved this problem in the WKB approximation

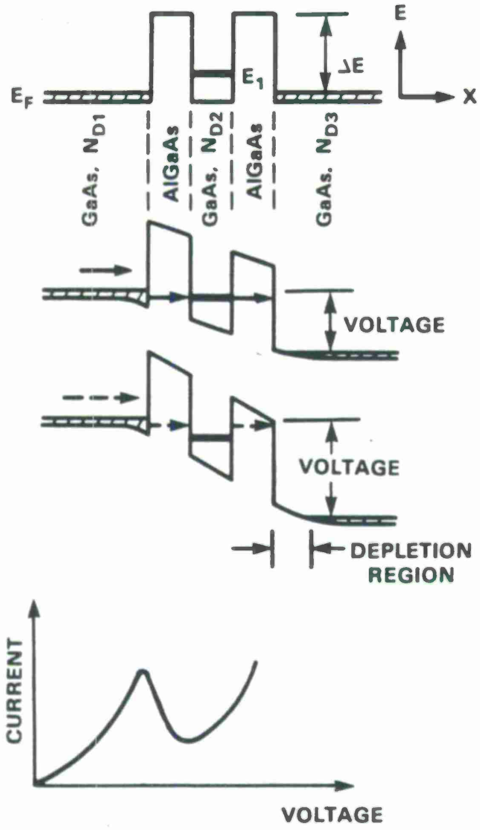

FIG. 1. Energy-band diagrams showing the origins of negative resistance in a double-barrier diode. The barriers are caused by the higher band gap of the AlGaAs alloy. These barriers create resonant states in the well at energies E_i, and the current has local maxima when these resonances are at the same energy as most of the electrons incident from the emitter on the left. The lifetime of an electron in one of these resonant states and the transit time through the depletion region are possible limits on the speed of the negative resistance.

and found the time to be given by the classical period of a carrier in the well divided by the transmission probability of the barrier, i.e.,

$$\Delta t = (\theta^2 + 1/16\theta^2)\tau$$
$$\cong \theta^2 \tau ,$$

where τ is the classical period,

$$\tau = 2 \frac{\partial}{\partial E} \int_{\rm well} \sqrt{2m(E-V)}\, dx ,$$

and the barrier transmission probability is θ^{-2}, where

$$\theta = \exp \int_{\rm barrier} \frac{\sqrt{2m(V-E)}}{\hbar}\, dx .$$

Here E is the energy of the carrier, V is the potential of the well or barrier, and m is the carrier effective mass. In Table I, the frequencies corresponding to Δt are given as $f_{\rm WKB} = 1/(2\pi\Delta t)$ for the several DBD's fabricated. These frequencies are well below the observed oscillation frequencies, so it is clear that there must be something wrong with this simple approach. Of course, the WKB approximation does not strictly apply since the potential in the DBD changes rapidly on the scale of the carrier wavelength. But probably the more severe limitation stems from the fact that the carrier is contained between two barriers separated by less than the carrier wavelength. Thus it is no longer reasonable to think of a carrier as being reflected between two barriers since it is located partially outside both barriers at any time. This greatly increases the escape probability, as we shall see.

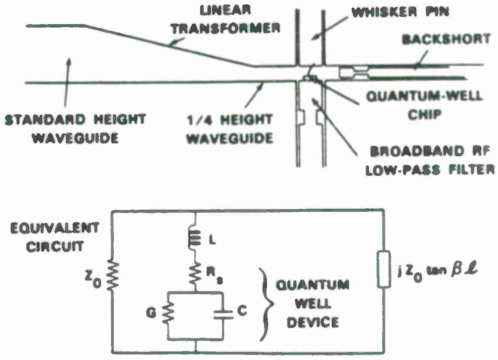

FIG. 2. Waveguide structure used to make oscillators from double-barrier diodes (DBD's) and the associated equivalent circuit. The circuit intrinsic to the DBD also limits the maximum oscillation frequency.

So far we have considered only the motion of electrons in the well. However, Luryi[2] calculates the current through a single barrier in the WKB approximation to find a resistance associated with the barrier, and from the capacitance across the barrier a time constant results,

$$RC = (\epsilon\alpha^{-1}\lambda/c)e^{4\pi d/\lambda} \quad \text{(cgs units)} ,$$

where $\lambda = h/\sqrt{2m\phi}$, ϕ is the average barrier height, m is the electron effective mass, ϵ is the barrier dielectric constant, $\alpha^{-1} = \hbar c/e^2 \cong 137$, d is the barrier thickness, and c is the speed of light. Luryi asserts that this RC time constant represents the lifetime of carriers in the well and hence the limit to oscillation frequencies. This limit is labeled f_L in Table I. This limit is also considerably less than the observed oscillation frequencies.

The lifetime of carriers in the well can also be estimated from a recent exact (numerical) solution to the time-dependent Schrödinger equation for a thin quantum well by Kundrotas and Dargys.[6] The authors solved for the probability of escape from a delta-function quantum well after the instantaneous application of an electric field. Their barriers were infinitely thick, so the escape time will be much larger than that from our thin barriers; hence this calculation provides an upper bound on the DBD escape time. They found the time required for the escape probability to reach near-unity values was significantly shorter than that predicted by standard approximations. Their results yield a cut-off frequency labeled $f_{\rm KD}$ in Table I. Note that $f_{\rm KD}$ is much higher than $f_{\rm WKB}$ even though the WKB calculation was for barriers of finite thickness.

Perhaps the most accurate method for estimating the lifetime of an electron in the well is to calculate the energy width of the transmission resonance through the double-barrier structure. Then the lifetime of this resonance is given by an uncertainty relation, $\tau = \hbar/\Delta E$, as recently pointed out by Ricco and Azbel[7] and by Coon and Liu.[8] This very general result, originally derived for atomic and nuclear transitions, applies to any resonant state.[9] We have calculated the

TABLE I. Measured and calculated parameters for three different wafers of double-barrier diodes.

	Sample		
	1	2	3
Material parameters			
Barrier material	AlAs	$Ga_{0.7}Al_{0.3}As$	AlAs
Barrier thickness (nm)	2.5	3.0	1.5
Well thickness (nm)	4.5	4.5	4.5
Doping outside barriers (cm^{-3})	1×10^{18}	2×10^{17}	2×10^{17}
Electrical parameters			
Peak-to-valley ratio, 300 K	1.7/1	1.3/1	3.5/1
Peak current density ($\times10^4$ A cm^{-3})	0.8	1.2	4.0
Depletion layer at bias (nm)	15	30	70
Capacitance (fF)[a]	100	50	20
Max. negative conductance (mS)[a]	5.0	8.0	13.0
Series resistance (Ω)[a]	10	15	15
Oscillation characteristics			
dc bias I_B,V_B (mA,V)	0.7,0.40	2.7,0.32	3.0,0.95
f_{osc} (GHz)[b]	20.7	43.7	56.4
THEORETICAL			
Max. oscillation frequency			
f_{circ} (GHz)[c]	35	70	200
f_{depl} (GHz)[d]	1000	500	230
f_{WKB} (GHz)[e]	0.01	220	6.0
f_L (GHz)[f]	0.01	60	6.0
f_{KD} (GHz)[g]	130	300	100
$f_{\Delta E}$ (GHz)[h]	80	2100	800

[a] Typical values for a circular mesa of 4 μm diameter.

[b] Maximum observed fundamental oscillation frequency.

[c] $f_{circ} = (2\pi C)^{-1}(-G_{max}/R_s - G_{max}^2)^{1/2}$.

[d] From depletion layer drift time.

[e] WKB estimate of charge storage time in well.

[f] From Ref. 2 for charge storage time in well.

[g] From Ref. 6, for electron lifetime in well with infinitely thick barriers.

[h] From calculation of energy width of transmission through double-barrier structure.

transmission as a function of incident electron energy for the structures of Table I using essentially the method outlined by Tsu and Esaki.[10] A frequency corresponding to the lifetime is listed in Table I as $f_{\Delta E}$. This frequency is generally higher than f_{KD} because of the finite barriers. (It seems to be slightly lower for sample 1.)

An important conclusion from this work is that the WKB method appears to consistently overestimate the escape time of an electron in a narrow quantum well with an electric field applied. The most satisfactory estimate of the well storage time comes from considering the width of the transmission resonance (leading to $f_{\Delta E}$) since this derivation is firmly grounded in the theory of scattering from resonant states. Transit time effects such as f_{depl} must also be considered, as must those limitations arising purely from the device equivalent circuit, f_{circ}. At this point in the development of DBD oscillators, these intrinsic circuit elements present the first hurdle to higher frequencies and must be optimized with the depletion layer drift time in mind. In view of the results discussed here, there appear to be no fundamental or practical impediments to DBD oscillators up to several hundred gigahertz.

We would like to take this opportunity to express our thanks to G. D. Johnson for assistance in fabrication and to P. E. Tannenwald for technical discussions. This work was supported by the U. S. Army Research Office and by NASA.

[1] T. C. L. G. Sollner, W. D. Goodhue, P. E. Tannenwald, C. D. Parker, and D. D. Peck, Appl. Phys. Lett. 43, 588 (1983).
[2] S. Luryi, Appl. Phys. Lett. 47, 490 (1985).
[3] E. R. Brown, T. C. L. G. Sollner, W. D. Goodhue, and C. D. Parker, Appl. Phys. Lett. 50, 83 (1987).
[4] D. J. Coleman, Jr. and S. M. Sze, IEEE Device Research Conference, Ann Arbor, MI, June 28, 1971; Bell Syst. Tech. J. 50, 1695 (1971).
[5] D. Bohm, *Quantum Theory* (Prentice-Hall, Englewood Cliffs, NJ, 1951).
[6] J. Kundrotas and A. Dargys, Phys. Status Solidi B 134, 267 (1986).
[7] B. Ricco and M. Ya. Azbel, Phys. Rev. B 29, 1970 (1984).
[8] D. D. Coon and H. C. Liu, Appl. Phys. 49, 94 (1986).
[9] J. Blatt and V. F. Weisskopf, *Theoretical Nuclear Physics* (Springer, Berlin, 1979).
[10] R. Tsu and L. Esaki, Appl. Phys. Lett. 22, 562 (1973).

APPENDIX F

Persistent photoconductivity in quantum well resonators

T. C. L. G. Sollner, H. Q. Le, C. A. Correa, and W. D. Goodhue
Lincoln Laboratory, Massachusetts Institute of Technology, Lexington, Massachusetts 02173

(Received 8 February 1985; accepted for publication 8 April 1985)

We have made the first observation of persistent photoconductivity in resonant tunneling structures. The spectral dependence suggests that it arises from Si *DX* centers in the AlGaAs barriers, and calculations based on a simple model using this assumption agree well with the observations. This effect has been useful in investigating the charge distribution and electric fields near the heterojunction interface and in determining the barrier parameters. The model should help in the design and fabrication of optimized resonant tunneling devices.

Resonant tunneling structures (quantum well resonators) have recently been shown to possess some intriguing characteristics, including high-speed charge transport ($\tau < 10^{-13}$ s) and broad regions of the negative resistance that can be used to produce oscillations at microwave, and perhaps higher, frequencies.[1,2] These heterostructure devices contain GaAs-AlGaAs interfaces that are capable of macroscopic segregation of carriers because of the difference in band gaps. Carriers in the AlGaAs diffuse to the GaAs with lower band gap, leaving behind an ionized impurity, and establish a dipole layer across the interface. In addition to hydrogenic impurities, it is well known[3] that in AlGaAs, electron traps called *DX* centers exist which, once optically ionized, remain so for long times at low temperatures, giving rise to a persistent photoconductivity. This effect has been used in quantum wells to study charge transport along the interface,[4] and we will show here that it can be helpful in clarifying resonant tunneling as well.

In this letter we report the first observation of persistent photoconductivity in resonant tunneling structures. We have observed a large effect upon the current-voltage (I-V) curve, and the spectral dependence of the effect confirms that it is due to Si *DX* centers in the AlGaAs barrier regions. A simple model agrees well with the observations and provides further insight into the physics of heterojunctions. It is possible for the first time from I-V curves alone to determine the conduction-band discontinuity and the barrier thickness uniquely.

A resonant tunneling structure consists of thin barrier regions of $Al_xGa_{1-x}As$ separated by thin regions of GaAs. As Fig. 1 shows, the barriers to electron flow occur because of the higher energy of the conduction band of the $Al_xGa_{1-x}As$. These barriers act as partially transparent mirrors to electrons, the charge transport taking place by tunneling through the thin barriers. Two of these barriers, placed sufficiently closely together that electron wave functions are coherent across them, form a sort of electron Fabry–Perot resonator with peaks in the electron transmission (current) as a function of incident electron energy (voltage). Current peaks occur when the voltage across the double-barrier region is roughly equal to $2E_i/e$, where E_i is one of the allowed energies, measured from the Fermi level, of electron motion normal to the barriers for carriers confined to the well. The lifetime of a carrier in the well is shortened by the possibility of tunneling out, so this level is broadened, as shown in Fig. 1. In our structures, only one level occurs, which is marked E_1 in the figure.

DX centers in AlGaAs are believed to be electron traps that are neutral until the electron is ionized. With the electron removed, a configurational change occurs so that recombination is unlikely without the assistance of a phonon of large momentum; thus, at low temperatures, relaxation times are extremely long. (Some repopulation may occur from long wavelength photons, as discussed by Nathan *et al.*[5] and by Kastalski and Hwang;[6] however, we have not observed repopulation with either 1.06- or 1.9-μm pulses.) The effect of the presence of positively charged centers in the barriers on the electron energy is shown by the solid lines in Fig. 1, whereas the dashed line shows the energy in the absence of ionized centers. If the conduction band in the well is below the Fermi level, a significant number of electrons accumulate in the well at zero bias. But at bias levels above a few tens of millivolts, they quickly tunnel out, so we have ignored this accumulation in our calculations and in Fig. 1. The net effect is that the well is lowered relative to the Fermi level and the effective barriers are lowered. The consequences of this potential shift will be discussed in more detail below.

The resonant tunneling structures were grown by molecular beam epitaxy on an n^+ wafer of GaAs. The barriers and the well widths are about 40 Å. The regions outside the barriers were doped with Si to 1×10^{18} cm^{-3}, whereas the barriers and well were nominally undoped (total impurity content $< 10^{15}$ cm^{-3}). The Al mole fraction in the barriers was $20 \pm 5\%$. Although no Si was grown in the barriers, appreciable diffusion of Si (but not Al) does take place during overgrowth of the top 5000-Å layer of GaAs. Using the diffusion constants of Tatsuta *et al.*,[7] we estimate an average Si concentration in the barriers of 2–5×10^{17} cm^{-3}. We note, however, that the Si diffusion in GaAs is about half as fast as in the $Al_{0.3}Ga_{0.7}As$ measured by Tatsuta *et al.*, so there

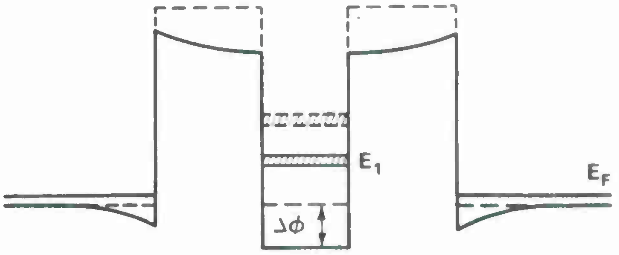

FIG. 1. Electron energy as a function of position in a quantum well structure with positive charge in the barriers and the electrons outside the barrier well region. The dashed lines show the conduction band in the absence of ionized centers.

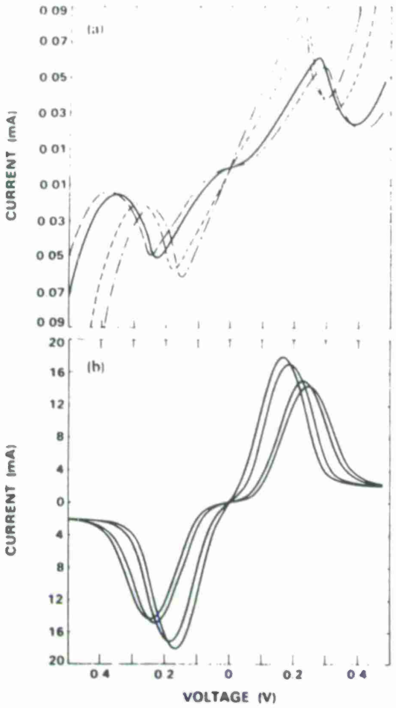

FIG. 2. (a) Observed and (b) calculated *I-V* curves for the structure shown in Fig. 1 for several exposures to 0.85-μm light. The long-dashed curve is unexposed, the solid curve has had an arbitrary exposure, Q, the short-dashed curve has exposure 10 Q, and the broken top curve has exposure 100 Q.

should be significantly less Si in the well. The heterojunction interface may also inhibit diffusion. Ohmic contacts are provided on the top and bottom of the wafer, and isolation is accomplished by the wet etching of 3-μm-diam mesas. Whisker contact is made to the small mesas.

Illumination was provided by a quartz-halogen lamp and a grating monochromator with the resolution set to 25 nm. A low-pass filter was used to eliminate higher order dispersion, and an electronic shutter controlled the exposure. The sample was mounted in a mechanical refrigerator with the mesa at 45° to the optical axis. The sample was cooled to 20 K in the dark. *I-V* curves were recorded after every exposure to produce a sequence of curves, some of which are shown in Fig. 2(a). Aside from the curve taken before exposure, each curve shown has an exposure ten times greater than the curve below it. The top curve has had nearly all the *DX* centers ionized. After the persistent photoconductive effect had saturated, the sample was warmed to room temperature and recooled for another experiment at a different wavelength.

The effects observed in Fig. 2(a) can be explained by the model shown in Fig. 1 and a calculation of the *I-V* curves at finite temperature in a way similar to that suggested by Tsu and Esaki,[8] except that accumulation and depletion regions are included. Figure 2(b) shows *I-V* curves calculated using this model for the same relative exposures as the experimental curves of Fig. 2(a) and the *DX* center density as determined below. The parameters used in the model were consistent with the growth constants of the structure, as described above, except that the temperature used in the model was 60 K rather than the physical temperature of the device of 20 K. The fact that little change in the observed *I-V* curves is seen below about 100 K supports this evidence that some electron heating is occurring, although the heating mechanism is unknown. The agreement with the observed curves is good, considering the simplicity of the model. The higher predicted current density is believed to arise from the omission of scattering in the theory. The current increase at higher voltages is not completely understood, but if it is due to impurity-assisted tunneling, then the observed increase with increasing *DX* center density would seem reasonable. More details of this model will be published in the future.

It remains to relate the observed shift of peak current at resonant bias voltage to the incident photon number. *I-V* curve calculations similar to those of Fig. 2(b) show that the shift in current and voltage of the resonant peak is a linear function of the shift in the well potential, $\Delta\phi$, for $\Delta\phi < E_1$ (see Fig. 1). The voltage shift can be understood from the resonant energy of the structure, E_1, which follows linearly the level of the well bottom. The peak current is also calculated to vary linearly with $\Delta\phi$, although it is not so obvious why this should occur.

It is easy to show from Poisson's equation that the shift in the well potential because of positive charges in the barriers is linearly related to the volume density, n, of ionized centers in the barriers by

$$\Delta\phi = \frac{ned}{2\epsilon}(d + 2l_{\mathrm{TF}}), \tag{1}$$

where d is the barrier thickness, e is the electron charge, ϵ is the dielectric constant of the barrier region, and l_{TF} is the Thomas–Fermi screening length in the GaAs surrounding regions. Thus, the change in resonant current, I_{pp}, and voltage, ΔV_{pp}, are expected to vary linearly with the ionized *DX* center density n. (We measure I_{pp} and V_{pp} as the total current and voltage, respectively, between the positive and negative resonance peaks.) We will assume for simplicity that the charge density in the two barriers is the same, although the slight asymmetry about zero in the *I-V* curve suggests some difference. This effect is minimized by measuring the sum of the changes in the *I-V* curve for both positive and negative directions.

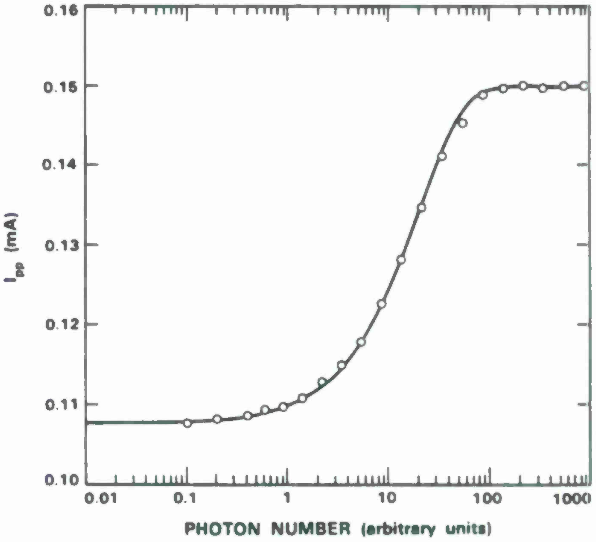

FIG. 3. Difference in current between positive and negative resonant peaks in the *I-V* curve as a function of exposure (in arbitrary units) to 0.85-μm photons. The solid curve fit to the data points is given by Eq. (3).

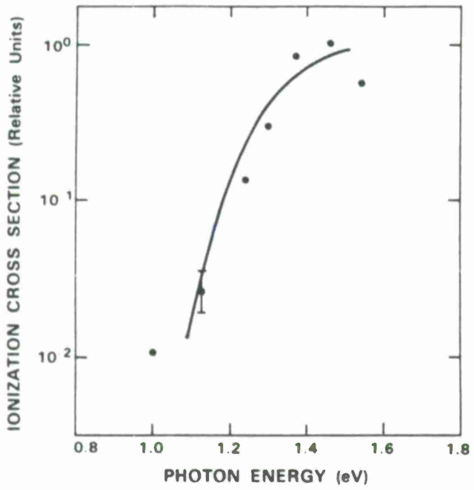

FIG. 4. Points show the observed photon energy dependence of the relative ionization cross section for the persistent photoconductive effect described in this letter. A typical error bar is shown on one data point. The solid line is from Ref. 9 for Si *DX* centers in $Al_{0.4}Ga_{0.6}As$. The agreement confirms that the effect observed here is caused by Si *DX* centers in the barrier regions of Fig. 1.

The density of ionized centers can be related to the number of incident photons, Q, by the usual exponential approach to saturation,

$$n = \frac{N_0\sigma_f(h\nu)\{1-\exp[-(\sigma_f+\sigma_t)Q/A]\}}{\sigma_f(h\nu)+\sigma_t(h\nu)}, \qquad (2)$$

where N_0 is the total volume density of *DX* centers, A is the illuminated area, and $\sigma_f(h\nu)$ and $\sigma_t(h\nu)$ are the photon-induced ionization and trapping cross sections, respectively. The latter can be expected to be negligible, except perhaps at longer wavelengths where some quenching may occur.[5,6] From Eq. (2) and the linearity discussed above, we arrive at an expression for the change in peak current.

$$\Delta I_p \approx \Delta I_{pp}^{\text{sat}}[1-\exp(-\sigma_f Q/A)]. \qquad (3)$$

A fit to the observed ΔI_{pp} as a function of Q yields $\Delta I_{pp}^{\text{sat}}$ and the relative ionization cross section $\sigma_f(h\nu)$. Figure 3 shows the fit of Eq. (3) to the observations at a wavelength of 0.85 μm. A similar expression holds for ΔV_{pp}, and the fit to experimental data is good, if not quite so close as that shown in Fig. 3. It is clear from these data that the model describes the observed effects very well.

The sequence of *I-V* curves for different exposures, as shown in Fig. 2, permits a determination of the material parameters that is not possible with a single *I-V* curve. Changing parameters in the *I-V* curve calculations shows that V_{pp} is determined primarily by the well width, but I_{pp} is sensitive to both barrier height and barrier width, so that the latter two quantities cannot be determined uniquely from the dark curve alone. With the added variable of charge in the barrier, however, the additional information from ΔI_{pp} and ΔV_{pp} resolves this ambiguity, allowing barrier height and width to be determined independently.

The total *DX* center density in the barriers ($N_0 = 3.8\times10^{17}$ cm^{-3}) is given by $\Delta V_{pp}^{\text{sat}}$, using Eq. (1) and the computed *I-V* curves. The well width (38 ± 3 Å), barrier height (160 ± 20 meV), and barrier width (40 ± 5 Å) are the parameters that give best agreement between the observed and calculated curves of Fig. 2. These structural parameters agree with estimates from growth conditions, whereas N_0 compares well with our estimate of total Si concentration in the barriers. This N_0 measurement indicates that a large fraction of the Si in AlGaAs occurs as *DX* centers, in agreement with most other studies. The value of barrier height gives an aluminum fraction of 0.18 ± 0.02, in good agreement with the target value of 0.2 ± 0.05, assuming the presently accepted value of 60% of the band-gap difference in the conduction band.

Repeating the experiment at different wavelengths yields the frequency dependence of the ionization cross section. Figure 4 shows the relative ionization cross section in the measured range. The solid line is that found for Si *DX* centers in AlGaAs by Lang and Logan.[9] There seems to be little doubt that the persistent photoconductive effect we observe arises from Si *DX* centers in the AlGaAs barriers.

We have shown that a simple model can explain persistent photoconductivity in resonant tunneling structures. This gives us some faith that the characteristics crucial to the design of optimum device structures can now be obtained from straightforward measurements, aiding in the design and fabrication of useful devices. The persistent photoconductivity demonstrated here is just one of several possibly useful phenomena (e.g., for image storage or memory elements). We have also observed fast photoconductivity in quantum well resonators, which will be reported in the future.

Help in fabrication of these devices was graciously provided by J. J. Lambert, I. H. Mroczkowski, and N. Usiak. We are also indebted to S. J. Allen of Bell Communications Research and to A. R. Calawa, B. A. Vojak, and D. D. Peck for advice and assistance. We would particularly like to thank P. E. Tannenwald for useful discussions. This work was supported by the U.S. Army Research Office.

[1] T. C. L. G. Sollner, W. D. Goodhue, P. E. Tannenwald, C. D. Parker, and D. D. Peck, Appl. Phys. Lett. **43**, 588 (1983).
[2] T. C. L. G. Sollner, P. E. Tannenwald, D. D. Peck, and W. D. Goodhue, Appl. Phys. Lett. **45**, 1319 (1984).
[3] R. J. Nelson, Appl. Phys. Lett. **31**, 351 (1977); or see D. V. Lang, R. A. Logan, and M. Jaros, Phys. Rev. B **19**, 1015 (1979).
[4] H. L. Stormer, A. C. Gossard, W. Wiegmann, and K. Baldwin, Appl. Phys. Lett. **39**, 912 (1981).
[5] M. I. Nathan, T. N. Jackson, P. D. Kirchner, E. E. Mendez, G. D. Pettit, and J. M. Woodall, J. Electron. Mater. **12**, 719 (1983).
[6] A. Kastalski and J. C. M. Hwang, Solid State Commun. **51**, 317 (1984).
[7] S. Tatsuta, T. Inata, S. Okamura, S. Muto, S. Hiyamizu, and I. Umebu, Paper D1.5, Fall Meeting of the Materials Research Society, Nov. 26–30, 1984, Boston, MA.
[8] R. Tsu and L. Esaki, Appl. Phys. Lett. **22**, 562 (1973).
[9] D. V. Lang and R. A. Logan, Inst. Phys. Conf. Ser. **43**, 433 (1979).

Proceedings 1985 IEEE/Cornell Conference on Advanced
Concepts in High Speed Semiconductor Devices and Circuits

Persistent Photoconductivity in Resonant Tunneling Structures: Toward a Resonant Tunneling Transistor*

T. C. L. G. Sollner, H. Q. Le, C. A. Correa, and W. D. Goodhue
Lincoln Laboratory, Massachusetts Institute of Technology
Lexington, Massachusetts 02173

Resonant tunneling structures have been shown to be capable of high speed charge transport as well as microwave oscillations.[1,2] More recently[3] persistent photoconductivity has been observed and has been used to improve model calculations of the electrostatic potential and hence of the current-voltage (I-V) curves. We will show here that the model can be used with the persistent photoconductivity measurements to derive the transconductance of a transistor based on the double-barrier resonant tunneling structure.

Figure 1 shows the conduction band of a typical double-barrier resonant tunneling structure. AlGaAs is used to provide thin (~50 Å) tunneling barriers in GaAs. Between these barriers is a thin (~50 Å) layer of GaAs. Electrons in this layer are confined by the barriers and hence are resonant levels. When a voltage is applied, a peak in the transmitted current occurs when the incident energy of an electron in the outer electrode region coincides with one of these resonant levels. This process is very similar to the action of a Fabry-Perot etalon, in which the AlGaAs tunnel barriers serve as partially transmitting mirrors, and the energy of the electrons plays the role of the photon energy.

It is intriguing to speculate on the possibility of attaching an electrical connection to the central GaAs well, so that a three-terminal device, a resonant tunneling transistor, is formed. Figure 2 shows one conceivable geometry for such a device. We will assume that the emitter is on the top surface, that the well acts as the base by controlling current flow between the emitter and collector, and that the collector is the bottom electrode. To reduce base resistance, the spacing between the base pads should be minimized. The n^- regions are essentially intrinsic, thus reducing base-to-emitter and base-to-collector capacitances. If these regions are kept thin, the current density will remain unchanged and the carrier transit time can be kept short compared to other time constants of the device. The conduction band at zero bias is shown on the left of the figure. We note that contact to the very thin base region will probably be a major technological challenge, but may be worth the effort in view of results presented later in this paper. We will estimate the operating characteristics of this type of transistor from the two-terminal results using the effects of persistent photoconductivity to simulate the third terminal.

---

*This work was supported by the U.S. Army Research Office.

The persistent effect of light on the quantum well I-V curves is shown in Figure 3. At temperatures below 20 K many hours are required for the current of an illuminated device to decay to that of an unexposed device. The solid I-V curve is unexposed, the long-dashed curve has had an arbitrary exposure, Q, the short-dashed curve has exposure 10 Q, and the broken top curve has exposure 100 Q which nearly saturates the effect. After exposure it is necessary to warm the sample to nearly room temperature and then recool to restore the unexposed state. The model which best explains these results is sketched in Fig. 4. It is well known that complexes called DX centers exist in n-type AlGaAs which exhibit a persistent ionization upon illumination. These ionized DX centers produce positive space charge in the barriers and the electrons which have been freed in the process find themselves in the electrode regions because their energy is lower there than either in the barriers or well. The dipoles thus formed have the effect of lowering the barriers and potential of the resonant energy level in the well with respect to the electrons in the electrodes, which is similar to the result of applying a potential directly to the well (base). This shifts the peak current to lower applied voltages and increases the transparency of the barriers.

Figure 5 shows a comparison between the observed and calculated I-V curves. The shift of the peaks to lower voltages is evident, and the increase in peak current and zero-voltage conductance are a result of the lower effective barriers. Notice that the observed current has a component which continues to increase at higher voltages. A further complication is that this component increases with increasing concentration of ionized centers. This leakage current probably arises from impurity assisted tunneling through the barriers. It will be a source of uncertainty in the calculation of transconductance which follows. It should also be noted that the calculated current density is much higher than that observed. Higher current densities can be expected if the actual fabrication more closely approaches the ideal structure on which our model is based.

The transconductance of a three-terminal device can be calculated from our measured I-V curves. The central idea involves the fact that the potential of the well (base) is lowered relative to the electrodes (emitter and collector) upon exposure to light as shown in Fig. 5. The shift in this potential, $\Delta\phi$, is easily calculated from the voltage shift, ΔV_p, in the current peak and is given by

$$\Delta V_p = 2\Delta\phi \qquad (1)$$

The factor of 2 arises from the fact that the base-to-emitter applied voltage is half of that applied between the base and collector. The change in collector current density, ΔJ_c, due to this change in base-to-emitter voltage, $\Delta\phi$, is given by the difference in current between the two curves. The transconductance, G_m, is therefore given by

$$G_m = A\ \Delta J_c/\Delta\phi = 2A\ \Delta J_c/\Delta V_p \qquad (2)$$

where A is the base area. There is one complication, however. Since the leakage current discussed above also changes with $\Delta\phi$, it is difficult to determine and account for this contribution. Nevertheless, it seems reasonable to assume that at voltages below the resonance the output impedance is large and positive. We have therefore extrapolated the excess current at high voltage smoothly back toward zero keeping the output impedance positive. These extrapolations are shown in Fig. 6. Using the I-V curves of Fig. 6 we obtain an intrinsic transconductance of 2000 mS/mm for an emitter width of 1 μm. Specific contact resistances on the order of 10^{-7} ohm cm^2 are necessary to realize an extrinsic transconductance of this order.

It is interesting to calculate the transit time through the active region. Suppose we use intrinsic regions near the emitter and collector of 400 Å each to minimize capacitance. Then at a saturation velocity of 10^7 cm/s an electron will cross the device in about 1 ps. In fact, the velocity would probably be much higher since transport across such short distances will be nearly ballistic.

Another parameter of interest is the small signal delay time

$$t = G_m/C$$

where C is the total input capacitance. Using the geometry and parameters described above, we find a gate delay time of about 3 ps, or a cutoff frequency of about 55 GHz.

Finally, we will examine the base resistance. Since the base is very thin and lightly doped, it might be expected that the base resistance would be quite high. However, there are some fortunate aspects to the quantum well geometry which reduce its resistance considerably. It is well known that electron mobilities in modulation-doped quantum wells are very high at temperatures of 100 K and below. Although this structure is not a modulation-doped well in the usual sense, the base layer acquires charge from the transiting carriers without any direct doping. Just as in a Fabry-Perot resonator, near the resonant transmission peak carriers build up between the barriers to a level much higher than the average transiting carrier density. For present samples we estimate an average well charge density of approximately 10^{17} cm^{-3}. Using the best reported[5] mobility at 50 K of 5×10^5 cm^2/V-s, a base carrier density of 2×10^{17} cm^{-3}, an emitter width of 1 μm and length of 20 μm, and a 40-Å well, we find a base resistance of less than 10 ohms. This gives an RC product for base resistance and collector capacitance of about 0.5 ps, so base resistance does not seem to be a serious limitation on performance.

The charge in the base layer will build up or decay by electrons tunneling in or out of the well. The characteristic time for this process is not easily calculated because the well size is comparable to the electron de Broglie wavelength. However, an exact calculation by Dargys and Kundrotas[6] for an electron in a delta-function potential with an applied electric field gives a value of this characteristic time of order 10^{-13} s for a GaAs well in AlGaAs and electric fields comparable to those in our structures near the resonance peak. The actual time required for our structure may even be less since our barriers have finite thickness.

In view of the promising estimations which have been made possible by the observation of persistent photoconductive effects, it seems reasonable to pursue the idea of a resonant tunneling transistor further. Contact to the thin base region appears to be the most difficult task at the moment, but if this could be overcome, the structure suggested here, as well as other similar designs, could be fruitfully investigated experimentally.

REFERENCES

1. T. C. L. G. Sollner, W. D. Goodhue, P. E. Tannenwald, C. D. Parker, and D. D. Peck, Appl. Phys. Lett. 43, 588 (1983).

2. T. C. L. G. Sollner, P. E. Tannenwald, D. D. Peck, and W. D. Goodhue, Appl. Phys. Lett. 45, 1319 (1984).

3. T. C. L. G. Sollner, H. Q. Le, C. A. Correa, and W. D. Goodhue, Appl. Phys. Lett. 47, 36 (1985).

4. D. V. Lang and R. A. Logan, Inst. Phys. Conf. Ser. 43, 433 (1979).

5. A. C. Gossard, Inst. Phys. Conf. Ser. No. 69, 1 (1984).

6. A. Dargys and J. Kundrotas, J. Phys. C: Solid State Phys. 18, L493-L495 (1985).

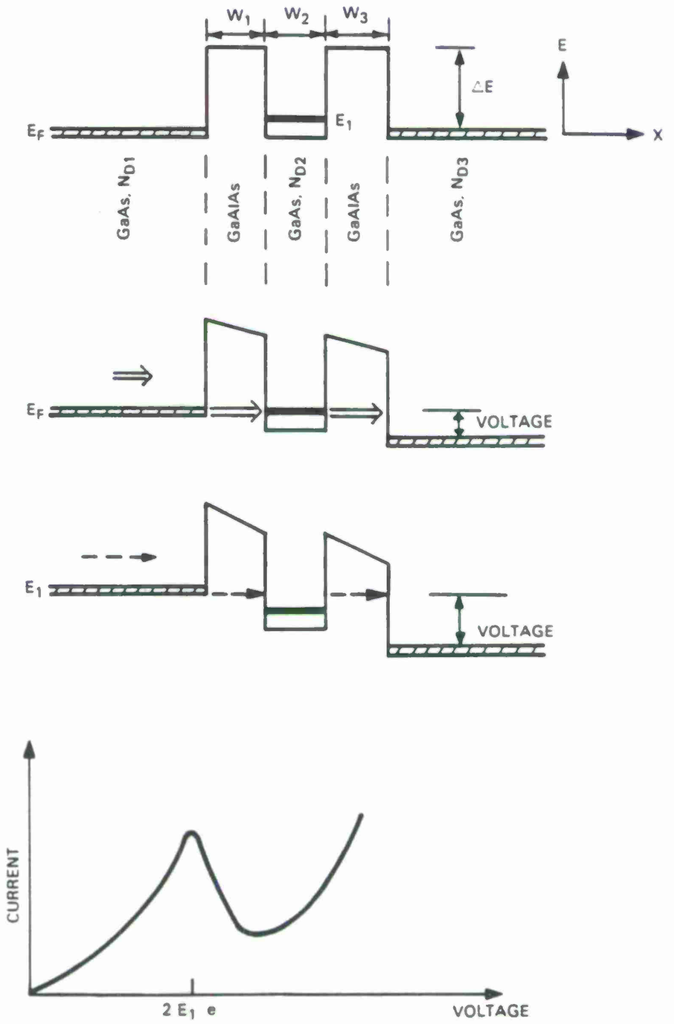

Figure 1. Electron energy as a function of position in the quantum well resonator. The energy level E_1 occurs above the bottom of the conduction band because of confinement in the x direction.

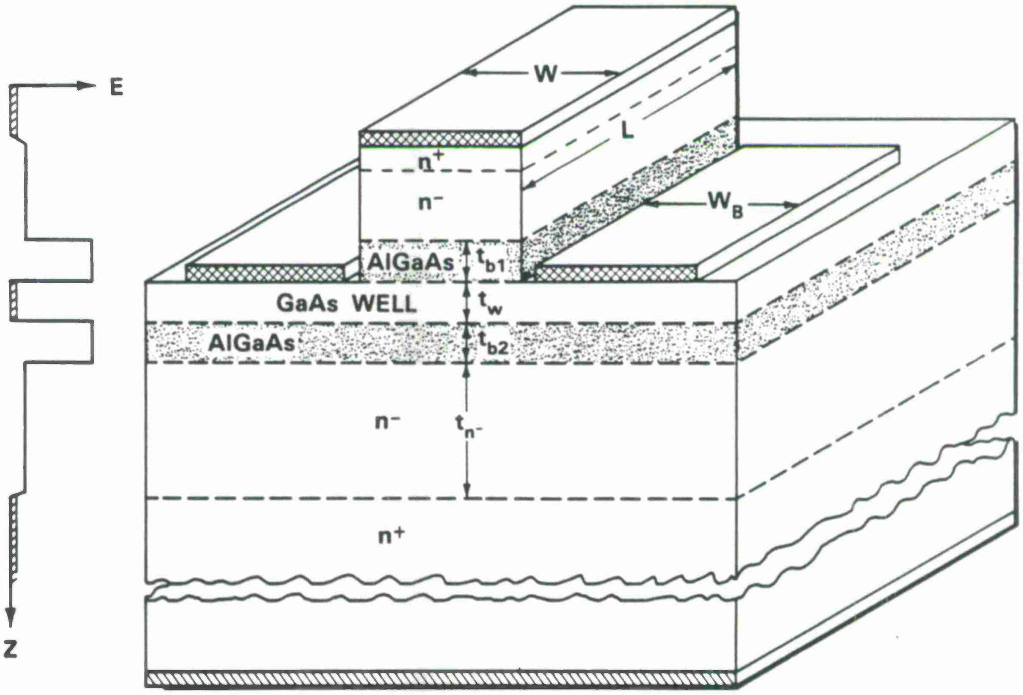

Figure 2. Proposed geometry for a resonant tunneling transistor. The spatial dependence of the conduction band energy is also shown.

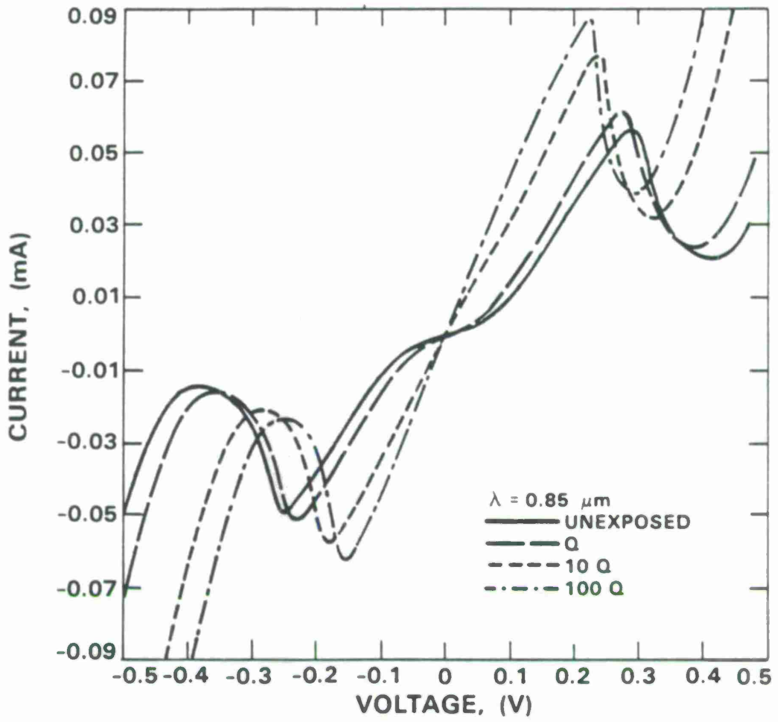

Figure 3. Current-voltage curves of a quantum well resonator after exposure to light, but after the light has been turned off. Four different exposures are shown.

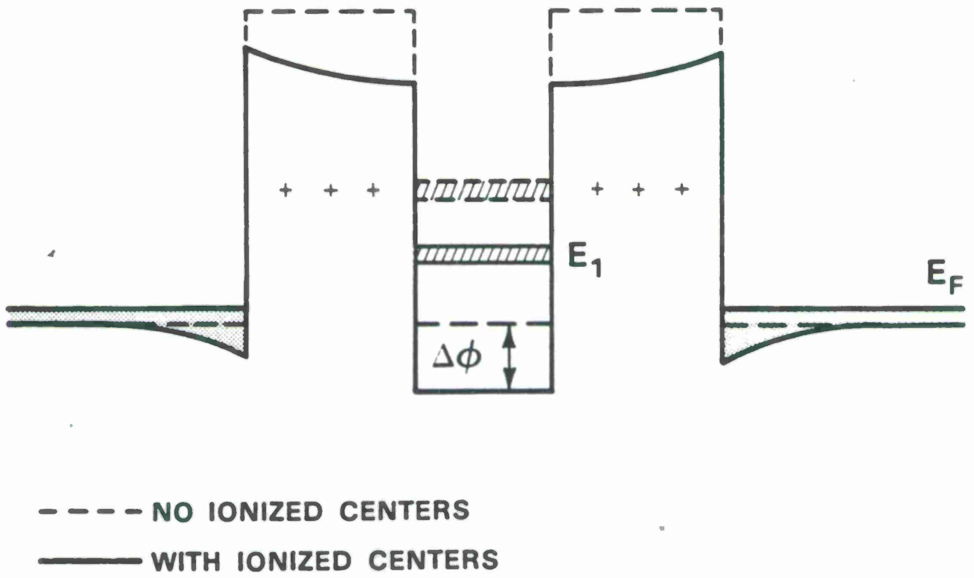

Figure 4. Electron energy as a function of position in a quantum well resonator showing the effect of positive charge in the barriers. The dashed lines show the conduction band in the absence of ionized centers.

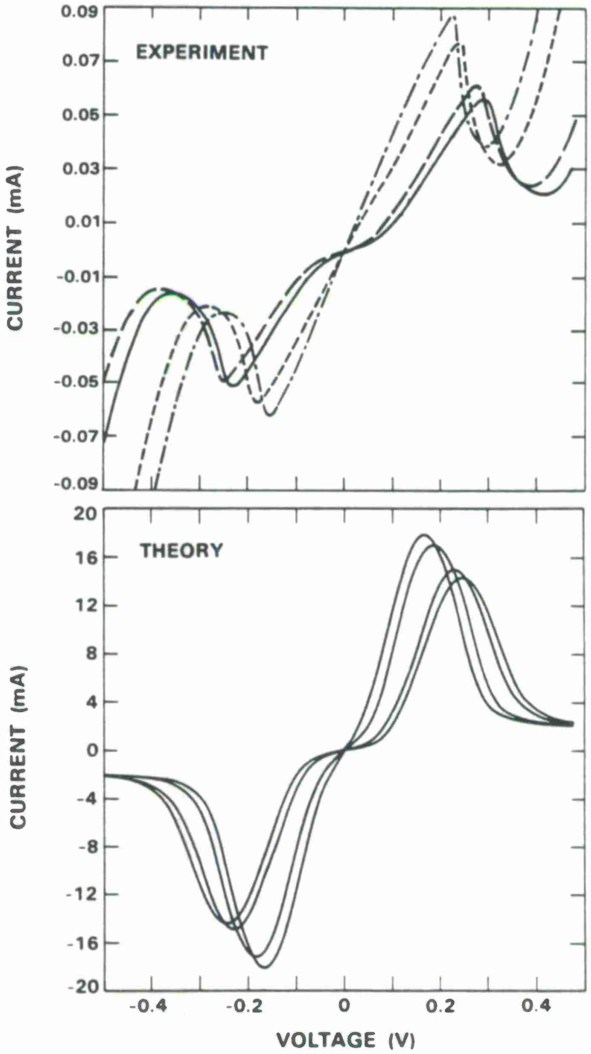

Figure 5. Observed and calculated I-V curves for the structure shown in Figure 4. The exposures are the same as in Figure 4.

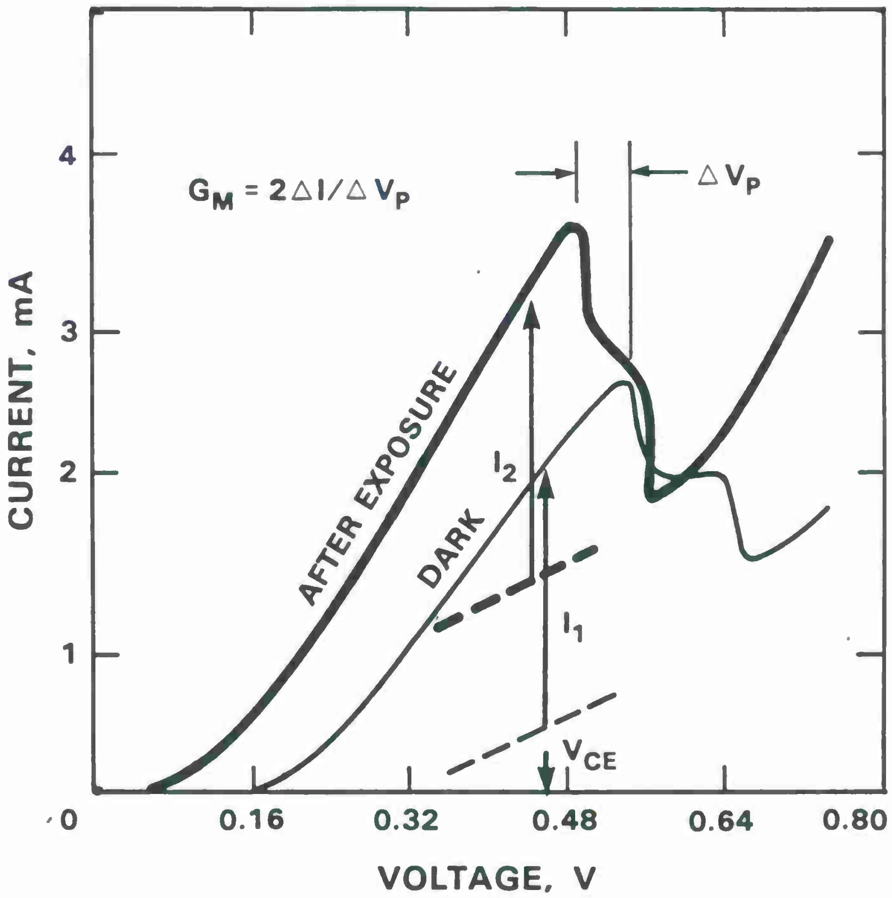

Figure 6. Method of calculating the transconductance of the proposed transistor from two terminal I-V measurements (see text).

APPENDIX H

Picosecond switching time measurement of a resonant tunneling diode

J. F. Whitaker and G. A. Mourou
Laboratory for Laser Energetics and Department of Electrical Engineering, University of Rochester, 250 East River Road, Rochester, New York 14623-1299

T. C. L. G. Sollner and W. D. Goodhue
Lincoln Laboratory, Massachusetts Institute of Technology, Lexington, Massachusetts 02173

(Received 7 March 1988; accepted for publication 1 June 1988)

Picosecond bistable operation has been experimentally observed for the first time in a double-barrier resonant tunneling diode. A rise time of 2 ps was measured using the electro-optic sampling technique; this is the fastest switching event yet observed for an electronic device. This time domain measurement adds necessary information to the understanding of the transport mechanisms in the resonant tunneling diode and is consistent with switching time limitations computed for the device. It also demonstrates that appropriately designed double-barrier quantum well diodes have a response time comparable to that of the fastest all-optical logic elements, and that they may be very useful in high-speed logic applications.

Since its inception by Tsu and Esaki,[1] the notion of quantum mechanical tunneling through double-barrier heterostructures has raised considerable interest. The negative differential resistance (NDR) exhibited by this device makes it suitable for a wide variety of applications; among them are oscillators,[2] mixers,[3] and transistors.[4,5] Especially noteworthy is the experimental[6] and theoretical[7] evidence suggesting that these devices could operate in the terahertz frequency regime. We report here, for the first time, the measurement of a double-barrier resonant tunneling diode (RTD) in its bistable or switching mode with sufficient temporal resolution to resolve the switching time. We have measured this switching time to be less than 2 ps. This time compares favorably with the theoretical considerations of Liu and Coon[8] for the switching time of a heterojunction double-barrier diode circuit. Practical electronic devices that respond on such a short time scale would rival the speed of the fastest optical switching elements, leading to their utility in electronic logic circuits of the future. These time domain measurements may also provide some insight concerning the mechanisms of electron transport through double-barrier heterostructures, processes that are far from being completely understood.

The RTD used in these measurements was grown by molecular beam epitaxy to have two barriers of 1.5-nm-thick AlAs separated by a GaAs well 4.5 nm thick. The outer regions of GaAs contained Si doping to an electron density 2×10^{17} cm^{-3}. This resulted in a peak current density of about 4×10^{4} A/cm^{2}. For the 4-μm-diam RTD tested here, the capacitance when biased near the current peak was calculated to be 20 fF, and the series resistance was 15 Ω. More details of the material growth and fabrication can be found in Ref. 9.

The device was tested using an instrument with the subpicosecond resolution necessary to measure such brief events, the electro-optic sampling system.[10] A schematic diagram of the circuit used to test the time response of the RTD is shown in Fig. 1. Coplanar electrodes of gold acting as a transmission line were deposited on both a GaAs switch and a lithium tantalate ($LiTaO_3$) sampling crystal, and the chip containing the array of resonant tunneling diodes was mounted so that the device faced the switching element as shown. An ohmic contact on one of the 4-μm-diam diodes was connected to an electrode using a gold-coated phosphor-bronze wire that had been etched to a 1 μm diameter at its tip. Another ohmic contact on the back of the RTD was fixed to one coplanar electrode on the $LiTaO_3$ crystal with silver epoxy, and the contact was completed with the pointed wire (whisker) such that the device was in series with the transmission line. Synchronized optical pulses from a dye laser of about 80 fs duration were used to activate a photoconductive switch at the input to the device and to measure the electric fields across the transmission line by probing the change in index of refraction in the $LiTaO_3$ induced by the output of the device. All the measurements reported were made at room temperature.

The equivalent circuit of the RTD can be represented as a capacitor in parallel with a variable resistor (which can be negative), and these in series with a small positive resistor, as shown in Fig. 2. The RTD was connected in series with a load resistance, a whisker inductance, and a time-varying photoconductive switch resistance $R(t)$, as shown. The dc

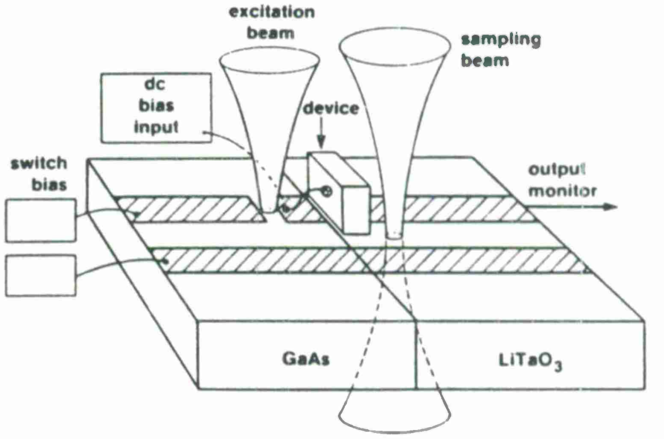

FIG. 1. Experimental configuration for electro-optic sampling of resonant-tunneling diode. A 12-μm-diam wire with a 1 μm tip contacts a mesa on the resonant-tunneling diode chip.

0003-6951/88/310385-03$01.00

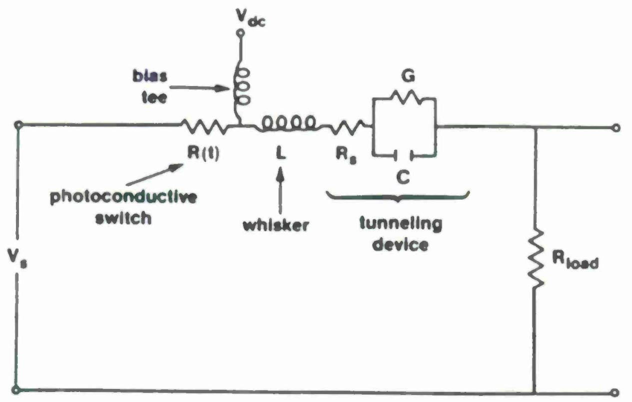

FIG. 2. Equivalent circuit for resonant-tunneling diode and test circuit.

bias to the RTD was applied through a large inductor, and the bias from the photoconductive switch was considered as the input to the network. Any other parasitic circuit elements have been ignored. When an additional current ΔI was presented to the RTD as the switch was illuminated and closed, a potential difference developed across the diode and its operating point was changed. As shown in the second and third frames of Fig. 3(a), the load line was thus shifted upwards on the current-voltage (I-V) characteristic from point A. When the load line exceeded the current peak of the I-V curve, the stable operating point became point C [see Fig. 3(a)], and switching was initiated. The switching time depended on how rapidly the device capacitance could be charged, resulting in a change of voltage from that of point A to point C.

The method used to determine the switching time of the device will now be presented. The region between the two load lines labeled "1" in each frame of Fig. 3(a) represents the shift in load line resulting from closing the switch with the optical pulse, when starting from different dc bias conditions. The region labeled "2," shown in the top frame only, indicates the shift in load line along a relatively linear portion of the I-V curve. The resulting waveform from region 2 at the output of the diode was used as a reference so that a comparison could be made to each of the other waveforms from region 1 and the switching response more easily resolved. This waveform 2 is depicted in each of the frames of Fig. 3(b). Displayed as a dashed line is the waveform from each region 1 in Fig. 3(a) and, below the waveforms, the temporal variation of the difference of the two waveforms. The waveforms in Fig. 3(b) are exaggerated to schematically show the effects of switching. The experimental result of subtracting the two waveforms from regions 1 and 2 is presented in Fig. 3(c). In the first frame, the cancellation is nearly complete. The discrepancies observed are due to noise and to small deviations in the regions of the I-V curve traversed. The switching process can be observed in the second and third frames of Figs. 3(b) and 3(c). In the second frame, curve 1, the dashed line, follows curve 2 only from points A to B, where it coincides with the rising portion of the I-V curve. When the load line exceeds the current peak of the I-V curve, the diode switches to point C and a rapid drop in current is observed. In the second frame, as the input decreases, the optical switch current also decreases so that the load line drops below point E, and the operating point returns to F and relaxes to A, where waveforms 1 and 2 are again nearly identical. This is indicated in the difference waveform $(1-2)$ of Fig. 3(b) and can also be seen in the experimental difference waveform in Fig. 3(c).

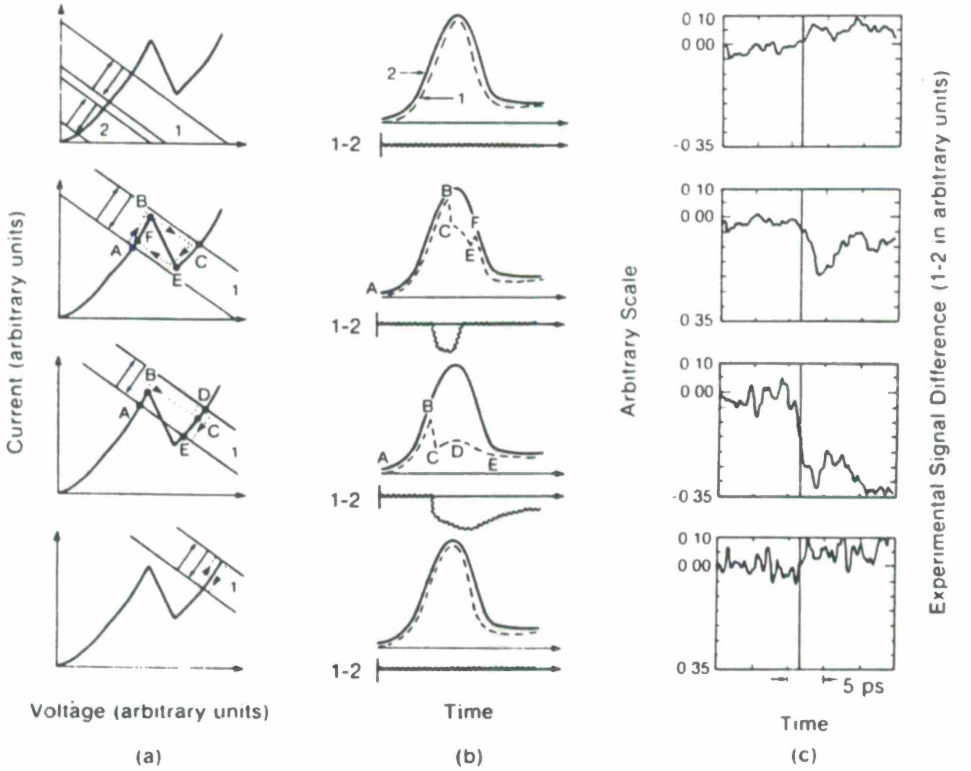

FIG. 3. Resonant-tunneling diode switching as a function of bias: (a) I-V curve with load lines, (b) analytic representation of waveforms resulting from movement of load lines in (a) and the difference of these waveforms, and (c) experimental signal difference.

The third frame of Fig. 3 displays the same switching action, but with the device attaining a latched state. The operation from points C to D to E is along a path of the I-V curve that would approximately cancel with that from region 2, leading to a long plateau on the difference waveform and a device that has been switched into the lower current state. This was distinctly observed in frame 3 of Fig. 3(c). Since the peak of the I-V curve was reached by the load line earlier than in the frame above, the switching took place at an earlier time, as evidenced by the position of the waveforms relative to the thin vertical line of Fig. 3(c) that represents a constant time reference. In frame 2, the onset of the switching began at the marker, while in frame 3 the switching event was already about halfway completed. The rise time of the switching event, as measured from the third frame of Fig. 3(c), was discovered to be 1.9 ps in duration between the 10% and 90% points. During the relatively long time between optical pulses, the bias point returns to point A. This is possible because the impedance determining the low-frequency load line is much smaller than the high-frequency impedance. In frame 4 of this figure, the dc bias point is extended above the area of negative differential resistance, where region 1 traverses virtually the same slope as region 2, and cancellation is again expected and found.

As mentioned earlier, the switching time should depend on the time to charge the device capacitance between the voltages corresponding to points A and C in Fig. 3(a)[7,8]:

$$t_s \approx C(V_C - V_B)/(I_p - I_v)\,, \qquad (1)$$

where I_p and I_v are the peak and valley currents in the negative differential resistance region. As measured experimentally, $V_C - V_B = 0.44$ V and $I_p - I_v = 3$ mA. Charge storage occurs predominantly outside the double-barrier region, and so to compute the capacitance, we must know the distance between the conductive regions on each side of the quantum well. The GaAs well width was 4.5 nm, while the AlAs barriers were 1.5 nm thick, and the depletion width into the doped collector region was approximately 70 nm. Using a relative permittivity for GaAs of 13.1, the capacitance was found to be about 20 fF, and the rise time for switching was calculated to be 2.9 ps. Bearing in mind that Eq. (1) is only approximately valid and that the instrumental contribution was not measured, this is in reasonable agreement with the measured value of 1.9 ps.

The tunneling current in a RTD can be a result of a resonant, coherent tunneling current, as in the optical analog of a Fabry–Perot resonator, and/or a sequential, incoherent tunneling process stemming from elastic and inelastic collisions. Originally, the idea of electrons scattering and sequentially tunneling was used by Luryi[11] to explain the discrepancy between the measured and expected current of the device. It was pointed out by Weil and Vinter[12] and Jonson and Grincwajg[13] that, in most cases, the tunneling current is proportional only to the resonant level linewidth Γ_r and insensitive to the scattering energy width Γ_i. The device response time, however, is inversely proportional to the total energy width of the system, $\Gamma_t = \Gamma_r + \Gamma_i$. The measured switching time can be looked at as an upper limit of the response time of the structure, since the measurement circuit could only increase the time of response. In our experiments, the device tested had a geometry such that Γ_r was about 2 meV. The resulting device response from resonant tunneling alone ($\tau \approx 2\hbar/\Gamma_r$) could therefore be of the order of a single picosecond. Thus we can make no statement about the importance of sequential tunneling from this measurement. However, if a RTD with a much smaller Γ_r were to show a switching time of a picosecond or so, then we could conclude that sequential tunneling was the dominant transport mechanism, since this process would give us the very fast response commensurate with the collisionally broadened Γ_i.

In conclusion, we have used the electro-optic sampling technique to measure the fastest switching event yet for an electronic device. The switching speed of the RTD is also comparable to the one observed in the fastest optical bistable devices. The similarity in the observed performance of the electronic and optical bistable devices is not surprising considering the fact that the switching time is limited by the round-trip time in the Fabry–Perot resonant cavity. That is, the nanometer dimensions and slow electron velocity of a RTD provide comparable round-trip times to those obtainable with the submicron dimensions but higher photon velocities of multiple quantum well optical devices. This illustrates just how similar electrical and optical resonators are, and how the response of electronic devices is catching up to the supposedly faster optical devices.

This work was supported by the Laser Fusion Feasibility Project at the Laboratory for Laser Energetics which has the following sponsors: Empire State Electric Energy Research Corporation, New York State Energy Research and Development Authority, Ontario Hydro, and the University of Rochester. Additional support was provided by the United States Air Force Office of Scientific Research under contract F49620-87-C-0016 to the Ultrafast Optical Electronics Center at the Laboratory for Laser Energetics of the University of Rochester. The work at Lincoln Laboratory was supported by the U.S. Army Research Office, NASA, and the U.S. Air Force. We would especially like to thank M. A. Frerking, S. Rowe, and P. D. Batelaan of the Jet Propulsion Laboratory for training us in the techniques of microstrip whisker contacts.

[1] R. Tsu and L. Esaki, Appl. Phys. Lett. 22, 562 (1973).
[2] T. C. L. G. Sollner, E. R. Brown, W. D. Goodhue, and H. Q. Le, Appl. Phys. Lett. 50, 332 (1987).
[3] T. C. L. G. Sollner, E. R. Brown, and W. D. Goodhue, in *Picosecond Electronics and Optoelectronics II*, edited by F. J. Leonberger, C. H. Lee, F. Capasso, and H. Morkoç (Springer, Berlin, 1987), p. 102.
[4] F. Capasso and R. A. Kiehl, J. Appl. Phys. 58, 1366 (1985).
[5] T. K. Woodward, T. C. McGill, and R. D. Burnham, Appl. Phys. Lett. 50, 451 (1987).
[6] T. C. L. G. Sollner, W. D. Goodhue, P. E. Tannenwald, C. D. Parker, and D. D. Peck, IEEE Trans. Electron Devices ED-30, 1577 (1983).
[7] D. D. Coon and H. C. Liu, Appl. Phys. Lett. 49, 94 (1986).
[8] H. C. Liu and D. D. Coon, Appl. Phys. Lett. 50, 1246 (1987).
[9] W. D. Goodhue, T. C. L. G. Sollner, H. Q. Le, E. R. Brown, and B. A. Vojak, Appl. Phys. Lett. 49, 1086 (1986).
[10] J. A. Valdmanis, G. A. Mourou, and C. W. Gabel, IEEE J. Quantum Electron. QE-19, 664 (1983).
[11] S. Luryi, Appl. Phys. Lett. 47, 490 (1985).
[12] T. Weil and B. Vinter, Appl. Phys. Lett. 50, 1281 (1987).
[13] M. Jonson and A. Grincwajg, Appl. Phys. Lett. 51, 1729 (1987).

APPENDIX I

Planar Dipole-Fed Mixer Arrays for Imaging at Millimeter and Submillimeter Wavelengths

John A. Taylor[†], **T.C.L. Gerhard Sollner, and Christopher D. Parker**
Lincoln Laboratory, Massachusetts Institute of Technology
Lexington, MA 02173

Joseph A. Calviello
AIL Division, Eaton Corporation
Walt Whitman Road
Melville, NY 11747

(1985 Intl. Conf. IR and MM Waves, Orlando, FL)

Abstract

The excellent sensitivity of single planar mixers at 140 GHz (T_R = 4900K DSB) has led us to investigate arrays of mixers, each fed by planar dipole antennas. Model measurements of impedances and mutual coupling, as well as fabrication and tests at millimeter and submillimeter wavelengths, are described.

Introduction

We have been investigating planar mixers for focal plane imaging at millimeter and submillimeter wavelengths [1,2]. We report here the progress in that effort, with new results at 140 GHz and at 1760 GHz, as well as new scale model results at 3 GHz.

Our design approach, described in References 1 and 2, has been the use of two microstrip dipole antennas on top of a grounded crystal quartz substrate, which feed a nonlinear mixing element. Crystal quartz was selected because of its availability in thin wafers (≤150 μm) and its relatively low dielectric constant. Recently we have been using high performance GaAs beam-lead Schottky diodes from AIL [3,4].

The basic circuit is shown in Figure 1. The antennas are two full-wavelength dipoles spaced by approximately $\lambda/2$ with the diode bonded midway between the antennas. The antenna pair acts as a 2 element array which radiates primarily in the direction perpendicular to the substrate. A low-pass filter, designed to reduce fundamental and second harmonic leakage, is partially shown at the right edge of Figure 1. Not shown is the 50 Ω coupled-microstrip transmission line from the filter to the edge of the substrate which carries the DC bias and IF signal. Both the filter and transmission line have been redesigned based on an improved theoretical model.

Scale Model Measurements

In order to continue to improve the performance of this circuit, scale models were constructed and tested at S-band (2-4 GHz). Measurements were first made of the impedance seen at the diode position of the double-dipole circuit. This measurement was made through a $\lambda/4$ balun with no diode in the circuit. A value of 38 + j23 Ω was obtained at 3.2 GHz, the scaled center frequency of the 140 GHz circuit. The measured impedance can be understood as the high, real impedance of a parallel pair of full wavelength dipoles transformed by a length of 100 Ω coupled microstrip transmission line. According to theory, at 3.2 GHz the phase shift between the diode port and each dipole is 112°. The extra phase shift beyond 90° is responsible for 40% of the inductive reactance observed. The additional inductance may be due to the balun or to operation at a frequency slightly off resonance.

A measurement of the impedance seen at the diode port is important for improving the match between the feed and the diode. For optimum coupling to this diode at millimeter wavelengths, the resistance presented by the feed should be approximately 150 Ω. This assumes that the diode resistance will be 100 to 200 Ω when it is biased for minimum conversion loss and noise [5,6]. The optimum value of feed inductance depends on the diode capacitance and the frequency of operation. Minor changes in the circuit dimensions such as an increase in the dipole feed gap or a decrease in the coupled microstrip line length could provide a significantly better impedance match.

Measurements were also made of the coupling between pairs of closely spaced double-dipole antennas to evaluate the suitability of the structure for diffraction-limited imaging. Any coupling between pairs of antennas in an array lessens the contrast available when imaging. Two configurations were tested for coupling between pairs: the H-plane orientation (*i.e.*, parallel pairs of dipoles) and the E-plane orientation (*i.e.*, collinear pairs of dipoles). In both cases the center-to-center separation was λ_0, the free-space wavelength. We measured $|S_{12}|$ = -26 dB and -35 dB in the E- and H-planes, respectively. The results are consistent with the value predicted by Pozar [7] for pairs of single resonant antennas in the E-plane configuration ($|S_{12}|$ = -30 dB).

Measurements at 140 GHz

We have fabricated the improved circuit on 150 μm quartz and tested its bandwidth, radiation pattern and heterodyne sensitivity near 140 GHz. Figure 2 shows the radiation pattern at 132 GHz plotted on a linear scale. The lack of nulls or significant ripples in the main beam leads us to believe that the coupling into the antennas from surface waves on the substrate is weak. The similar widths of the E- and H-plane patterns are important for coupling to circular lenses and reflectors.

In order to estimate the spectral bandwidth of the antenna, video responsivity measurements were made at several different frequencies. A peak responsivity of 170 V/W was measured at 132 GHz and at least 85 V/W was measured over a 12% bandwidth. The theory of Pozar [7] predicts that greater bandwidth could be achieved if a thicker substrate were used; however, a thicker substrate would increase the surface wave coupling.

[†] Also with the Department of Electrical and Computer Engineering, University of Massachusetts, Amherst, MA 01003.

The circuit has been tested as a planar mixer with the LO and blackbody RF signal combined externally in a quasi-optical diplexer. Both beams were focused onto the substrate by an offset ellipsoidal mirror. A receiver temperature of 4900K (DSB) and a total conversion loss of 8.5 dB were measured at an IF frequency of 1.1 GHz. The mixer required 4 mW of LO power from the carcinotron and 1.5 mA bias for optimum sensitivity. This LO power level suggests that high power sources are needed as local oscillators if large arrays of this type are to be driven to optimum sensitivity.

Submillimeter Measurements

The circuit has been fabricated on 70 and 33 μm quartz for testing at 300 and 560 GHz, respectively, which is in progress. The diodes used typically have $R_s = 3.5\ \Omega$ and $C_j(0) = 9$ fF, yielding a cutoff frequency of 5000 GHz. In order to examine the upper frequency limit of the 560 GHz circuit, we have tested it at 1760 GHz (171 μm) using a methanol laser pumped by a CO_2 laser. We measured a video responsivity of 5 mV/W. At 171 μm we believe that the diode is acting as its own antenna, since the diode is on the order of 2λ in length. A different design approach, such as monolithic fabrication on a thinner substrate, is more appropriate at this wavelength and could yield improved sensitivity.

Conclusions

We have developed a planar millimeter wave mixer fed by microstrip dipole antennas which has excellent sensitivity and radiation patterns at 140 GHz. The improvement over our previous results is thought to be due to better low-pass filter and transmission line designs, and to the use of a smaller, lower resistance diode. Scale modeling at 3.2 GHz has been used to estimate the circuit impedance at the diode position and to determine the coupling between circuits closely spaced in an array. Measurements at 171 μm suggest that a different construction approach is needed at this short wavelength.

Acknowledgments

We wish to thank Dr. A. Gopinath of Lincoln Laboratory and Dr. K.S. Yngvesson of the University of Massachusetts for valuable discussions concerning this work. This work was supported in part by the U.S. Army Research Office and the Department of the Air Force.

References

1. P.T. Parrish, T.C.L.G. Sollner, R.H. Mathews, H.R. Fetterman, C.D. Parker, P.E. Tannenwald, A.G. Cardiasmenos, "Printed Dipole - Schottky Diode Millimeter Wave Antenna Array," *Proc. SPIE*, 337, pp. 49-52, 1982.

2. H.R. Fetterman, T.C.L.G. Sollner, P.T. Parrish, C.D. Parker, R.H. Mathews, and P.E. Tannenwald, "Printed Dipole Millimeter Wave Antenna for Imaging Array Applications," *Electromagnetics*, 3, pp. 209-215, 1983.

3. S. Nussbaum, J.A. Calviello, E. Sard and N. Arnoldo, "Widely Tunable Millimeter-Wave Mixers Using Beam-Lead Diodes," *IEEE MTT-S Intl. Microwave Symp. Digest*, pp. 209-211, 1982.

4. J.A. Calviello, J.L. Wallace and P.R. Bie, "High-Performance GaAs Beam-Lead Mixer Diodes for Millimetre and Submillimetre Applications," *Electron. Lett.*, 15, pp. 509-510, 1979.

5. A.V. Räisänen, "Experimental Studies on Cooled Millimeter Wave Mixers," *Acta Polytechnica Scandinavica*, EE Series 46, pp. 31-36, 1980.

6. D.E. Held and A.R. Kerr, "Conversion Loss and Noise of Microwave and Millimeter - Wave Mixers: Part 2 - Experiment," *IEEE Trans. Microwave Theory Tech.*, 26, pp. 55-61, 1978.

7. D.M. Pozar, "Considerations for Millimeter Wave Printed Antennas," *IEEE Trans. Antennas Propagat.*, 31, pp. 740-747, 1983.

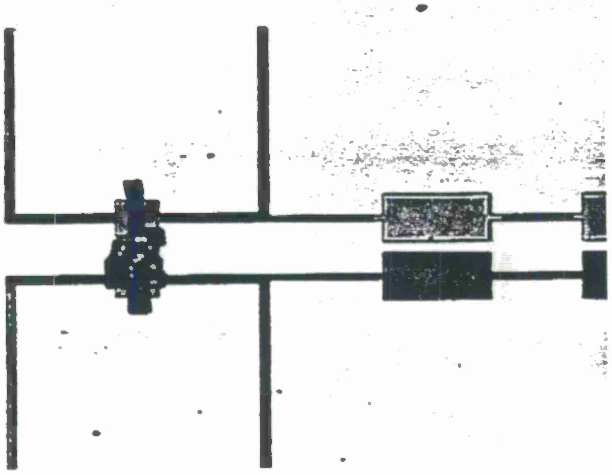

Figure 1. The double-dipole circuit with AIL beam-lead Schottky diode bonded midway between the two full-wavelength dipoles. The microstrip circuit shown here is Au on 150 μm crystal quartz for operation at 140 GHz.

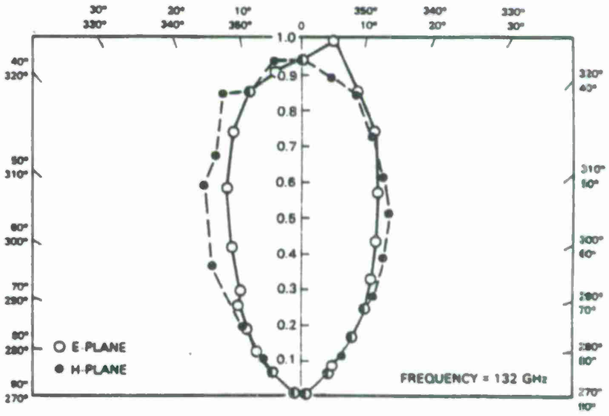

Figure 2. The radiation pattern at 132 GHz of the antenna pair shown in Figure 1.

APPENDIX J

International Journal of Infrared and Millimeter Waves, Vol. 6, No. 8, 1985

SUBMILLIMETER-WAVE HETERODYNE SPECTROSCOPY WITH A COMPACT SOLID STATE RADIOMETER

John A. Taylor† and Peter E. Tannenwald

Lincoln Laboratory, Massachusetts Institute of Technology
Lexington, Massachusetts 02173

Neal R. Erickson

Five College Radio Astronomy Observatory
University of Massachusetts
Amherst, Massachusetts 01003

Gerald F. Dionne and James F. Fitzgerald

Lincoln Laboratory, Masachusetts Institute of Technology
Lexington, Massachusetts 02173

Received May 23 1985

---

†Also with the Department of Electrical and Computer Engineering, University of Massachusetts, Amherst, MA 01003.

0195-9271/85/0800-0687$04.50/0

Abstract

A compact, solid state submillimeter-wave heterodyne radiometer has been developed and was used to measure spectral characteristics of a water vapor jet in a space simulation chamber. Features of the 557 GHz water vapor line profile were observed in significantly greater detail than in previous experiments through an increased sensitivity and improved frequency resolution (600 kHz). The local oscillator of the radiometer consisted of a frequency multiplication chain which was driven by an InP Gunn oscillator at 92.6 GHz, and which contained a frequency tripler and harmonic mixer in cascade. The front end of the receiver had a noise temperature of 4500 K (DSB) at 555 GHz, consumed 3 W and weighed 3 kg. This advance in technology is particularly relevant to submillimeter-wave radiometry from a space-based platform.

Key words: water vapor spectroscopy, submillimeter-wave radiometry, heterodyne radiometer, submillimeter-wave oscillator, frequency multiplier.

Introduction

In the last few years at Lincoln Laboratory we have conducted a series of experiments on the submillimeter radiative properties of a jet of H_2O molecules ejected from a sonic nozzle and expanded adiabatically into a high-vacuum chamber (1)-(3). The intensities and line shapes of the 752 and 557 GHz rotational transitions of the cooled H_2O molecules were measured radiometrically against a warm background using heterodyne receivers developed here and at the University of Massachusetts. Although the radiometers were operated in a laboratory environment, the experiments were designed to simulate heterodyne spectroscopic measurements that could be carried out from a space-based platform. Space operation would allow observations in areas such as astronomy and aeronomy that would not be masked by atmospheric water vapor absorption.

The 752 GHz experiment used a far-IR laser pumped by a CO_2 laser as the local oscillator (LO) (1), while the 557 GHz measurements were made with a harmonic mixer and a

282 GHz carcinotron as the LO (3). In both experiments difficulty in achieving sufficient LO power with frequency stability limited the quality of the spectral data. Moreover, because of their large size, weight and power requirements, neither LO is readily adaptable for use in space.

These problems have prompted us to develop a local oscillator chain for the submillimeter band which uses only solid state components. With this new oscillator we have demonstrated the operation of a solid state submillimeter radiometer near 557 GHz with best DSB noise temperature of 4500 K, front end (LO, mixer and IF amplifier) weight of 3 kg and power consumption of about 3 W. The radiometer was used to repeat the water jet spectroscopy experiment in the space simulation chamber, yielding results substantially superior to the two previous experiments.

The Radiometer

A block diagram of the present radiometer and spectroscopy experiment is shown in Figure 1. The local oscillator of the radiometer began with a 50 mW InP Gunn oscillator (4) at 92.58 GHz. This signal was fed by waveguide to a frequency tripler containing a GaAs Schottky varactor diode (5),(6). The varactor diode was whisker-contacted and mounted in a crossed-guide structure with each waveguide terminated by a movable backshort. The tripler produced approximately 3 mW of power at 278 GHz, which was fed by waveguide to a harmonic mixer (5). A diagram of the harmonic mixer, which contained a whisker-contacted Schottky mixer diode, is given in reference 3. The harmonic mixer has also been operated as a frequency doubler, which has permitted the chain to operate as a sextupler. When driven by an IMPATT oscillator, this chain has produced 50 μW at 556 GHz (7). The two multipliers will be described more fully at a later date (8).

Although the receiver was operated at 557 GHz in the spectroscopy experiment, its DSB noise temperature improved from 7800 K to 4500 K when the signal frequency was lowered to 555 GHz. This difference was due to the fact that the mixer's performance was dependent on the LO power supplied to it, which in turn varied sharply with the frequency-dependent impedance match between the tripler and mixer.

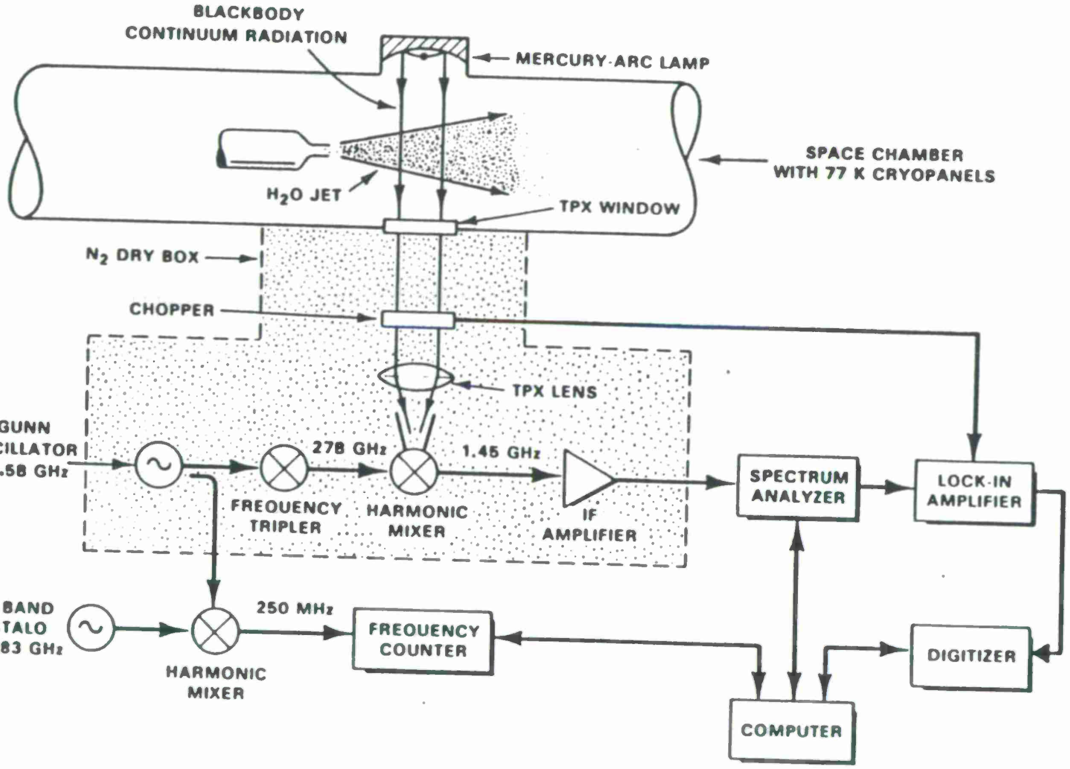

Figure 2. Block diagram of 557 GHz heterodyne radiometer. The receiver was housed in a N_2 dry box to prevent ambient H_2O from absorbing the signal.

In the spectroscopy experiment the harmonic mixer combined the tripled Gunn signal with the chopped RF signal containing the spectral information to yield an intermediate frequency (IF) at 1.45 GHz. This IF signal was amplified by a GaAs MESFET with a noise temperature of 50 K, then passed through a digitally-controlled bandpass filter in the spectrum analyzer. The filter's bandwidth was 300 kHz and its center frequency was stepped through the spectral line in nominal 250 kHz increments. The actual step size included a correction for the frequency drift of the Gunn oscillator with respect to the tenth harmonic of an X-band cavity-stabilized klystron (stalo), as measured by the frequency counter. Although this tracking filter did not compensate for rapid changes in the Gunn's frequency (jitter), it did correct for the Gunn's frequency drift due to thermal effects. The 100 kHz wide jitter in the Gunn resulted in an overall frequency resolution of 600 kHz. This could be improved significantly by further frequency stabilization. After filtering, the signal was synchronously detected, integrated for 3 sec, digitized and recorded by computer.

Spectroscopy Results

As in the previous experiments (1)-(3), a laboratory-scale water vapor jet from a 1 cm diameter nozzle was directed along the axis of a large high-vacuum chamber with liquid nitrogen cryopanelled walls. Figure 2 shows the highly resolved 557 GHz H_2O absorption line measured against a Hg arc continuum at a point 50 cm downstream from the jet nozzle for a nominal flow rate of 0.5 g/sec. To illustrate the substantial improvement in sensitivity and resolution, the line profile measured previously under similar conditions, but with the radiometer using a carcinotron LO (3), is sketched for comparison. At line center, the signal temperature represents the adiabatically cooled rotational temperature of the optically thick line. The minimum temperature of -75 K agrees with the value reported earlier (3). The linewidth reflects the Doppler broadening caused by the range of flow velocities in the diverging molecular beam, and its nearly flat bottom is due to saturated absorption of the continuum radiation by most Doppler components. The steep rise and fall of the line now indicate that the divergence angle of the vapor jet is well defined.

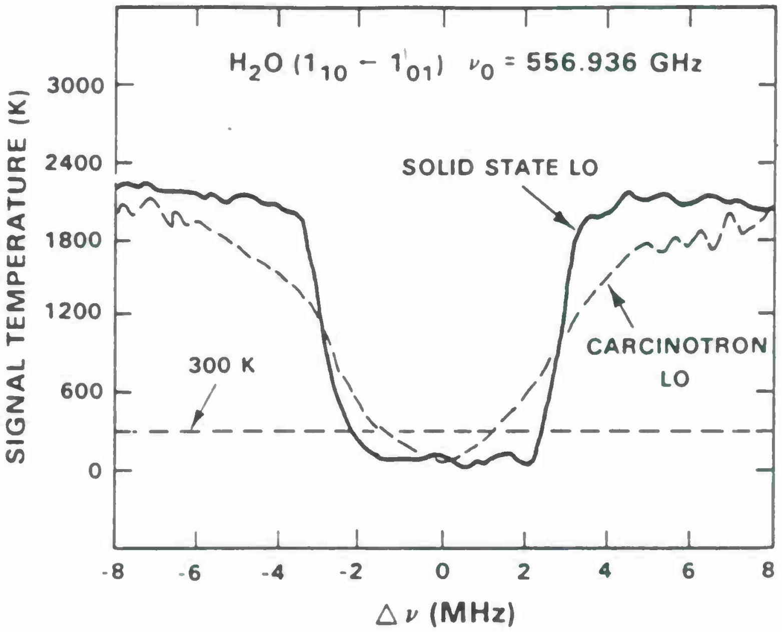

Figure 2. Optically-thick H_2O absorption line profiles measured at 50 cm from nozzle against Hg arc lamp background. Comparison is made with data from earlier experiment using a carcinotron LO.

Figure 3 shows the unsaturated H_2O absorption line under the same conditions but at a point 200 cm from the nozzle. The improved resolution has contributed at least partly to the observation of a self-reversal effect more prominent than that reported originally (2), where it was attributed to Doppler-shifted regions of varying optical depths and temperatures in the expanding jet. The shape and magnitude of the self reversal were again sensitive to the particular H_2O flow rate and the distance downstream from the nozzle. Without additional data, it is not possible to separate the relative contributions of jet temperature and

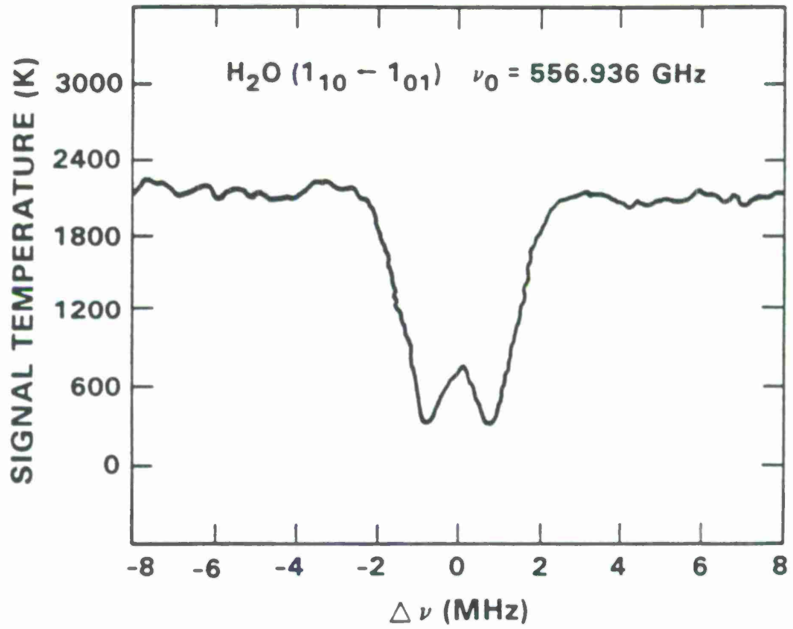

Figure 3. Absorption line of H_2O jet illuminated by Hg arc lamp under conditions which caused a self reversal around the center of the line. Both Figures 2 and 3 contain corrections for the constant power in the image sideband and for 2 dB loss in the TPX chamber window (see, e.g., Ref. 3).

opacity to the self reversal. This reflects a general problem in radiometry, which occurs when the quantity observed is the product of the local temperature and absorption, integrated along the line of sight. In our case the detected signal is the sum of the radiometric temperature of the arc lamp attenuated by the cold water vapor and the emission from the vapor. Additional measurements, other than radiometric, must be made to more fully understand the dynamics of a vapor jet expanding adiabatically into a vacuum. However, the present radiometer is well suited for obtaining the necessary spectroscopic information.

Conclusion

The development of a solid state submillimeter-wave oscillator has expanded the range of possible experiments in submillimeter radiometry and spectroscopy. Earlier we described the oscillator's operation as a "stand-alone" source which could be useful for direct-detection spectroscopy (7), and here we have discussed its application as the LO of a compact heterodyne radiometer for high-resolution spectroscopy. The sensitivity and stability of this radiometer are close to state-of-the-art (9), and the combination of these factors with the receiver's compactness and efficiency make this a promising system for use in space. Space operation may require minor modifications in the receiver design, although both multipliers used in this experiment have proved to be rugged and reliable, having survived three years of laboratory tests without a failure.

Acknowledgments

We wish to thank Dr. T. C. L. G. Sollner of Lincoln Laboratory for valuable suggestions concerning this work and Dr. J. L. Ryan, also of Lincoln Laboratory, for making the space chamber available to us. We wish to thank Dr. Lothar Wandinger, U. S. Army Electronics R & D Command, and Dr. James Crowley of Varian Associates for providing us with the InP Gunn oscillators. This work was supported by the U.S. Army Research Office and the Department of the Air Force.

References

1. G. F. Dionne, J. F. Fitzgerald, T-S. Chang, M. M. Litvak, and H. R. Fetterman, "Radiometric Observations of the 752.033-GHz Rotational Absorption Line of H_2O from a Laboratory Jet," Intl. J. Infrared and Millimeter Waves, vol. 1, pp. 581-595, 1980.

2. G. F. Dionne, J. A. Weiss, J. F. Fitzgerald, H. R. Fetterman, and M. M. Litvak, "High-Resolution Submillimeter-Wave Radiometry of Supersonic Flow," Appl. Phys. Lett., vol. 42, pp. 862-864, 1983.

3. G. F. Dionne, H. R. Fetterman, N. R. Erickson, C. D. Parker, and J. F. Fitzgerald, "Heterodyne Radiometry Measurements of the 557 GHz H_2O Rotational Line," IEEE J. Quant. Electron., vol. QE-20, pp. 188-190, 1984.

4. B. Fank, J. Crowley and C. Hang, "InP Gunn Diode Sources," SPIE Conf. Millimeter-Wave Technology III, Arlington, VA, paper 544-03, 1985.

5. N. R. Erickson, "High Efficiency Millimeter and Submillimeter Frequency Multipliers," in Eighth Intl. Conf. Infrared and Millimeter Waves Digest, Miami, FL, paper M3.2, 1983.

6. N. R. Erickson, "A High-Efficiency Frequency Tripler for 230 GHz," in Twelfth European Microwave Conf. Proc., Helsinki, Finland, pp. 288-292, 1982.

7. J. A. Taylor, N. R. Erickson, P. E. Tannenwald, "Solid-State Submillimeter-Wave Source," Solid State Research Report, Lincoln Laboratory, M.I.T., vol. 2, pp. 61-62, 1984.

8. N. R. Erickson, to be published.

9. W. J. Wilson, "Submillimeter-Wave Receivers - A Status Report," IEEE Trans. Microwave Theory Tech., vol. MTT-31, pp. 873-878, 1983.

REPORT DOCUMENTATION PAGE

1a. REPORT SECURITY CLASSIFICATION Unclassified		1b. RESTRICTIVE MARKINGS			
2a. SECURITY CLASSIFICATION AUTHORITY 2b. DECLASSIFICATION/DOWNGRADING SCHEDULE		3. DISTRIBUTION/AVAILABILITY OF REPORT Approved for public release; distribution is unlimited.			
4. PERFORMING ORGANIZATION REPORT NUMBER(S) Final		5. MONITORING ORGANIZATION REPORT NUMBER(S) ESD-TR-89-142			
6a. NAME OF PERFORMING ORGANIZATION Lincoln Laboratory, MIT	6b. OFFICE SYMBOL *(If applicable)*	7a. NAME OF MONITORING ORGANIZATION Electronic Systems Division			
6c. ADDRESS *(City, State, and Zip Code)* P.O. Box 73 Lexington, MA 02173-0073		7b. ADDRESS *(City, State, and Zip Code)* Hanscom AFB, MA 01731			
8a. NAME OF FUNDING/SPONSORING ORGANIZATION U.S. Army Research Office	8b. OFFICE SYMBOL *(If applicable)* ARO 22746-PH	9. PROCUREMENT INSTRUMENT IDENTIFICATION NUMBER F19628-85-C-0002 Program 88			
8c. ADDRESS *(City, State, and Zip Code)* P.O. Box 12211 Research Triangle Park, NC 27709-2211		10. SOURCE OF FUNDING NUMBERS			
		PROGRAM ELEMENT NO. 81102A	PROJECT NO.	TASK NO.	WORK UNIT ACCESSION NO.

11. TITLE *(Include Security Classification)*
Submillimeter Quantum Electronics

12. PERSONAL AUTHOR(S)
T.C.L. Gerhard Sollner

13a. TYPE OF REPORT Final Report	13b. TIME COVERED FROM 4/1/85 TO 11/1/88	14. DATE OF REPORT *(Year, Month, Day)* 1989, June, 14	15. PAGE COUNT 84

16. SUPPLEMENTARY NOTATION
The view, opinions and/or findings contained in this report are those of the author(s) and should not be construed as an official Department of the Army position, policy, or decision, unless so designated by other documentation.

17. COSATI CODES

FIELD	GROUP	SUB-GROUP

18. SUBJECT TERMS *(Continue on reverse if necessary and identify by block number)*
resonant tunneling
oscillators
multipliers
radiometer
DX centers

19. ABSTRACT *(Continue on reverse if necessary and identify by block number)*

The phenomenon of resonant tunneling has been explored in GaAs/AlGaAs heterostructures that were grown by molecular-beam epitaxy. The physics and fundamental speed limitations were studied, and devices such as oscillators, multipliers, and mixers have been demonstrated. Useful output has been obtained at room temperature for frequencies up to 425 GHz. The feasibility of resonant-tunneling transistors has been examined, suggesting cutoff frequencies above 100 GHz. Planar antenna arrays have been developed and tested up to 1.7 THz. In the area of compact solid-state instrumentation, a 555 GHz receiver was developed that had a noise temperature of 45000 K and weighed 3 kg.

20. DISTRIBUTION/AVAILABILITY OF ABSTRACT ☐ UNCLASSIFIED/UNLIMITED ☒ SAME AS RPT. ☐ DTIC USERS	21. ABSTRACT SECURITY CLASSIFICATION Unclassified	
22a. NAME OF RESPONSIBLE INDIVIDUAL Lt. Col. Hugh L. Southall, USAF	22b. TELEPHONE *(Include Area Code)* (617) 981-2330	22c. OFFICE SYMBOL ESD/TML